

DTIC FILE COPY

AD-A230 466

(1)



DTIC
SELECTED
JAN 07 1991

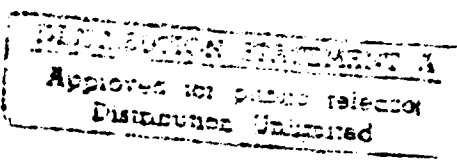
D D

A METHOD OF MOMENTS SOLUTION FOR THE
ELECTRIC CURRENTS ON AN APERTURE-FED,
STACKED PATCH MICROSTRIP ANTENNA

THESIS

William L. Irvin, Captain, USAF

AFIT/GE/ENG/90D-27



DEPARTMENT OF THE AIR FORCE
AIR UNIVERSITY
AIR FORCE INSTITUTE OF TECHNOLOGY

Wright-Patterson Air Force Base, Ohio

91 1 3 173

AFIT/GE/ENG/90D-27

6

DTIC
ELECTED
JAN 07 1991
S D D

A METHOD OF MOMENTS SOLUTION FOR THE
ELECTRIC CURRENTS ON AN APERTURE-FED,
STACKED PATCH MICROSTRIP ANTENNA

THESIS

William L. Irvin, Captain, USAF

AFIT/GE/ENG/90D-27

Approved for public release; distribution unlimited

A METHOD OF MOMENTS SOLUTION FOR THE ELECTRIC CURRENTS ON AN
APERTURE-FED, STACKED PATCH MICROSTRIP ANTENNA

THESIS

Presented to the Faculty of the School of Engineering
of the Air Force Institute of Technology
Air University
In Partial Fulfillment of the
Requirements for the Degree of
Master of Science in Electrical Engineering

William L. Irvin
Captain, USAF

December 1990

Accepted:	
Major Advisor	Minor Advisor
Dr. J. C. Vardoulakis	Dr. J. R. Gaskins
University Advisor	University Advisor
J. R. Gaskins	J. R. Gaskins
By	
William L. Irvin	
Availability Codes	
Dist	Avail. Under Special
A-1	

Approved for public release; distribution unlimited

Preface

The purpose of the effort was to provide the Air Force Institute of Technology with the foundation of an analysis and design capability for aperture-fed, stacked patch antennas. While the Method of Moments software written during this study is not optimal in many aspects, my major goal of providing software flexibility and documentation has been met to the best of my ability.

While the words for this thesis are the products of my own hand, their existence are the results of enormous contributions from numerous people. First, I must express my appreciation to my advisor Major Harry Barksdale for his guidance and support over the last year. I also wish to thank my thesis committee members, Captains Phil Joseph and Byron Welsh, for their much needed assistance. I also gratefully acknowledge the assistance and hard work of fellow student Captain Ron Erwert for providing preliminary data on the polynomial models of the antenna Green's functions. I also wish to thank classmate Captain Bill Wood for teaching me the "ins and outs" of the computer network at AFIT.

I must also thank my family for their support over the last 18 months and during my entire Air Force career. Thanks to my mother and father for teaching me the importance of hard work and patience. Thanks to my mother- and father-in-law for the support they've provided to me and my family during my AFIT tour. Also, I must thank my son, Chandler, and daughter, Kendall, for providing a means of escape during what was at times a seemingly unending endeavor.

Finally, and above all others, I thank my dear wife Pam; without her strength, faith, and love the last 18 months would have been far too much for me. We finally made it.

Leon Irvin
December, 1990

TABLE OF CONTENTS

Preface	iii
Abstract	viii
I. Introduction	1-1
1.1 Background on Microstrip Antennas	1-1
1.2 Advantages and Disadvantages of Microstrip Antennas	1-3
1.3 The Aperture-Fed, Stacked Patch Microstrip Antenna	1-4
1.4 Research Description	1-6
1.4.1 Problem Statement.	1-6
1.4.2 Research Objectives and Scope.	1-6
1.4.3 Research Assumptions.	1-7
1.5 Summary of Current Knowledge	1-8
1.6 Materials and Equipment Needed	1-9
1.7 Thesis Organization	1-9
II. Current Efforts - Microstrip Antennas	2-1
2.1 Aperture Fed Microstrip Antennas	2-1
2.2 Stacked Patch Microstrip Antennas	2-4
2.3 Aperture Fed, Stacked Patch Antennas	2-6
2.4 Microstrip Antenna Solutions Using the Method of Mo- ments	2-8
2.5 Summary of Current Knowledge	2-11
III. Theory	3-1
3.1 The Antenna Model	3-2
3.2 Tangential Electric Field Equations	3-4
3.3 Details of the Method of Moments Solution.	3-11
3.3.1 Basis and Test Functions.	3-13
3.3.2 Converting Integral Equations to Matrix Equa- tions.	3-18
3.3.3 Properties of the MoM Solution Matrix.	3-25
3.4 Challenges of the MoM Solution	3-26
3.4.1 Evaluating the Antenna's Green's Functions.	3-27
3.4.2 Modeling the Microstrip Feedline.	3-30
3.5 The 3-Plane Model - A Solution Independent of the Excitation Source	3-31
3.5.1 Approximations for the Aperture Fields.	3-31
3.5.2 Modified Matrix Equation.	3-33
3.6 Solving the MoM Matrix Equation	3-34
3.6.1 Solving the Matrix Equation via Iteration.	3-35
3.6.2 Basic Iterative Method.	3-35
3.6.3 An Iterative Approach Suited to the MoM Solu- tion.	3-36
3.7 Calculating the Fields of the Antenna	3-39
3.7.1 Calculating the fields on the Antenna Inter- faces.	3-39
3.7.2 Calculating the Antenna Far-Field Patterns.	3-40

IV. Method of Moments Software Description	4-1
4.1 Numerical Integration Equations	4-1
4.1.1 Impedance Sub-Matrix Gaussian Quadrature Equations.	4-4
4.1.2 Inner-Product Gaussian Quadrature Equations.	4-9
4.2 Software Overview	4-11
4.3 Antenna Data Subroutines	4-14
4.3.1 Subroutine INPUT.	4-14
4.3.1 Subroutine SEGMENT.	4-19
4.3.2 Subroutine ASYGF5.	4-26
4.4 Method of Moments Matrix Equation Subroutines	4-27
4.4.1 Subroutine EVALSUB.	4-28
4.4.2 Subroutine SURFINT.	4-31
4.4.3 Subroutine RHOFIND.	4-33
4.4.4 Subroutine EVALGRN.	4-39
4.4.4 Subroutine EVALRHS.	4-39
4.5 Matrix Equation Solution Subroutines	4-41
4.5.1 Subroutine SOLVNVR5.	4-41
4.5.2 Subroutine INVERT.	4-41
4.6 Data Output Subroutines	4-44
4.6.1 Subroutine OUTPUT.	4-44
4.6.2 Subroutine JDISTR.	4-45
V. Results	5-1
5.1 Physical Description of the Sample Antennas	5-1
5.1.1 Antenna #1.	5-1
5.1.2 Antenna #2.	5-2
5.2 Surface Current Data	5-2
5.2.1 Surface Currents on Antenna #1.	5-3
5.2.2 Surface Currents on Antenna #2.	5-13
5.3 Surface Current Expansion Coefficients	5-16
5.4 MoM Impedance Matrix Properties	5-19
VI. Recommendations	6-1
6.1 Conclusions	6-1
6.2 Expanding the MoM Software	6-2
6.1.1 Incorporating a Feed System Model	6-3
6.1.2 Calculations for Bandwidth Characteristics	6-3
6.1.3 Modifications for Field Pattern Calculations	6-4
6.3 Improving Computation Efficiency	6-5
Appendix A. Green's Functions Sommerfeld Integrals and Polynomial Approximations	A-1
Appendix B. Evaluation of the Analytic Asymptotic Green's Function Term	B-1
Bibliography	BIB-1

LIST OF FIGURES

Figure 1-1	Microstrip Antenna with (a) Microstrip Feed and (b) Coaxial Feed	1-2
Figure 2-2	Geometry of the Aperture-Fed, Stacked Patch Microstrip Antenna	1-5
Figure 2-1	Side View (a) and Top View (b) of Pozar's Aperture-Fed Microstrip Antenna	2-2
Figure 2-2	Coaxially-Fed, Stacked Patch Microstrip Antenna	2-5
Figure 3-1	Equivalent Antenna Model With Incident and Induced Currents.	3-2
Figure 3-2	Geometry of the Antenna Charge and Current Cells	3-11
Figure 3-3	Surface Current Rooftop Basis Functions and Surface Charge Pulse Doublet Basis Functions for x- and y-directed Current Cells	3-14
Figure 3-4	Aperture Model for Calculating Far-Field Radiation Patterns	3-42
Figure 4-1	Array Representation of Current Cells on the Antenna Patches.	4-21
Figure 5-1	Plots of x-directed Surface Currents for the First Three Rows of x-cells on the Patch of Interface 2b, Antenna #1 (data from four node quadrature)	5-4
Figure 5-2	Plots of y-directed Surface Currents for the First Three Rows of y-cells on the Patch of Interface 2b, Antenna #1; (data from four node quadrature)	5-5
Figure 5-3	Plots of y-directed Surface Currents for Rows Four, Five, and Six of y-cells on the Patch of Interface 2b, Antenna #1 (data from four node quadrature)	5-6
Figure 5-4	Plots of x-directed Surface Currents for the First Three Rows of x-cells on the Patch of Interface 3b, Antenna #1 (data from four node quadrature)	5-8
Figure 5-5	Plots of y-directed Surface Currents for the First Three Rows of y-cells on the Patch of Interface 3b, Antenna #1 (data from four node quadrature)	5-9
Figure 5-6	Plots of y-directed Surface Currents for the First Three Rows of y-cells on the Patch of Interface 3b, Antenna #1 (data from four node quadrature)	5-10
Figure 5-7	Plots of x-directed Surface Currents for the First Three Rows of x-cells on the Patch of Interface 2b, Antenna #1 (data from six node quadrature)	5-11
Figure 5-8	Plots of x-directed Surface Currents for the First Three Rows of x-cells on the Patch of Interface 3b, Antenna #1 (data from six node quadrature)	5-12
Figure 5-9	Plots of x-directed Surface Currents for the First Three Rows of x-cells on the Patch of Interface 3b, Antenna #2 (data from four node quadrature)	5-14
Figure 5-10	Plots of the y-directed Surface Currents for Rows Five and Six of y-cells on the patch of Interface 3b, Antenna #2 (data from four node quadrature)	5-15

LIST OF TABLES

Table 3-1	Antenna Tangential Field Boundary Conditions [23] . . .	3-4
Table 3-2	An Example Antenna with its Associated MoM Segment- ation	3-35
Table 5-1	Surface Current Coefficients for the Patch of Interface 2b	5-17
Table 5-2	Surface Current Coefficients for the Patch of Interface 3b	5-18
Table A-1	Coefficients for I^r_{b21} Polynomial Model	A-5
Table A-2	Coefficients for I^s_{b21} Polynomial Model	A-5
Table A-3	Coefficients for I^t_{b21} Polynomial Model	A-6
Table A-4	Coefficients for I^r_{b31} Polynomial Model	A-8
Table A-5	Coefficients for I^s_{b31} Polynomial Model	A-8
Table A-6	Coefficients for I^t_{b31} Polynomial Model	A-9
Table A-7	Coefficients for G^b_{A22} Polynomial Model	A-12
Table A-8	Coefficients for G^b_{q22} Polynomial Model	A-12
Table A-9	Coefficients for G^b_{A32} Polynomial Model	A-14
Table A-10	Coefficients for G^b_{q32} Polynomial Model	A-14
Table A-11	Coefficients for G^b_{A33} Polynomial Model	A-18
Table A-12	Coefficients for G^b_{q33} Polynomial Model	A-18

Abstract

This study presents a method of moments solution for the surface currents and charge distributions on an aperture-fed, stacked patch antenna. To make the solution independent of the antenna excitation technique, an aperture magnetic current distribution is assumed, and the spatial Green's functions of the antenna are used to calculate the tangential fields on the antenna patches and coefficients for a finite series expression of the surface currents and charge densities. The Green's functions of the antenna are modeled with polynomials that are a function of the radial distance separating observer and source locations. The method of moments solution is implemented using FORTRAN 77 and requires no external software support. The numerical techniques, algorithms, and complete software functional descriptions are also included.

A METHOD OF MOMENTS SOLUTION FOR THE ELECTRIC
CURRENTS ON AN APERTURE-FED, STACKED PATCH MICROSTRIP ANTENNA

I. *Introduction*

This chapter presents a brief overview of microstrip antennas and the motivation for the analysis of the aperture-fed, stacked patch microstrip antenna. The exact goals of this thesis, along with the assumptions made during the research, are discussed. A brief review of current aperture-fed, stacked patch microstrip antenna analysis efforts, and an introduction to the method of moments is also included. In conclusion, an overview of the remaining chapters of the thesis is given.

1.1 *Background on Microstrip Antennas*

In its simplest form, a microstrip antenna consists of two parallel, conducting layers separated by a dielectric substrate. Typically, the upper layer is the radiating element and the lower serves as a

ground plane. Input to the antenna can be supplied in a number of ways.

Two of the most versatile feed techniques are the microstrip feedline and the coaxial feed (see Figure 1-1). Radiation from the antenna is

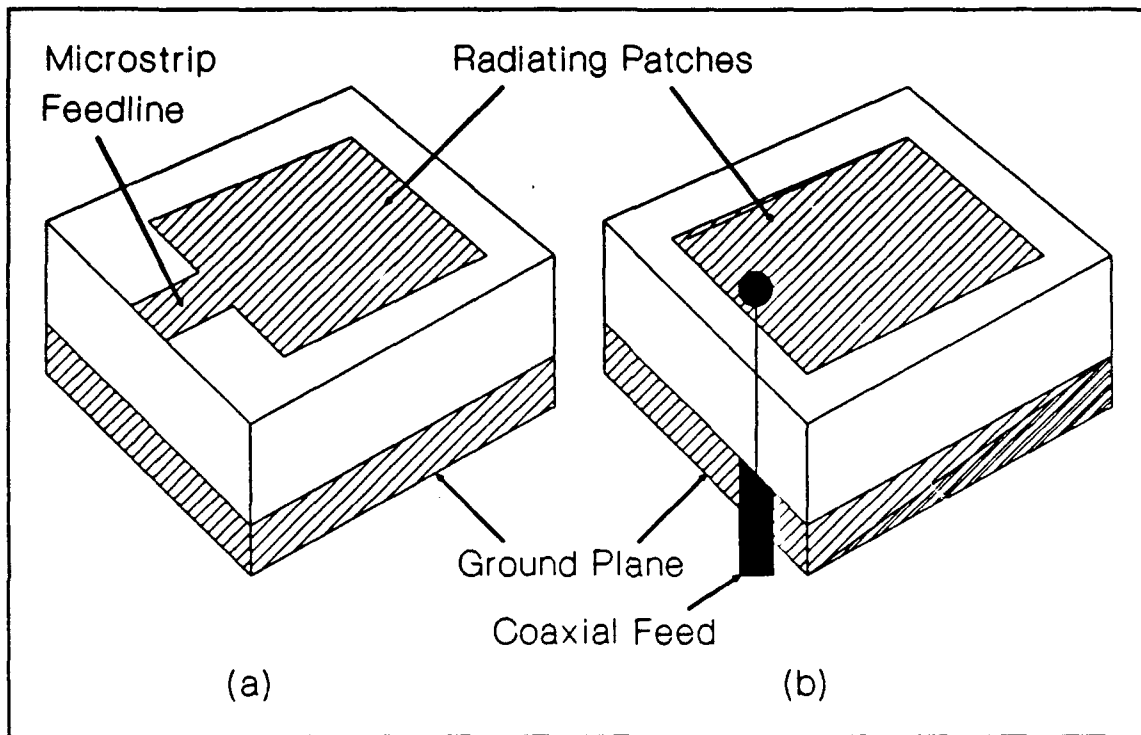


Figure 1-1 Microstrip Antenna with (a) Microstrip Feed and (b) Coaxial Feed

produced by fringing of the electric field along the open-circuited edges of the patch. The radiating patch of the antenna is typically $\lambda/2$ long, thus the normal components of the antenna's radiation tend to cancel in the far-field, while the components parallel to the antenna ground plane are in phase. Therefore, the radiated fields are at a maximum in the direction normal to the antenna's surface [1:5]. The radiating patch may be any shape, but rectangular or circular elements

are commonly used because of the relative simplicity of analyzing their radiation characteristics [2:488].

G. A. Deschamps first proposed the concept of a microstrip antenna in 1953. However, 20 years passed before photo-etching techniques and material properties were developed to the point where practical microstrip antennas could be built [1:1]. A series of successful, independent experiments in the early 1970's demonstrated the feasibility of microstrip antennas. By 1978, the microstrip antenna was widely known and used in a variety of communications systems [6:2]. Since the 1970's, extensive research and development exploiting the numerous advantages of the microstrip antenna, both as a single radiation source and as an array element, have established it as a separate entity within the broad field of microwave antennas [1:1].

1.2 Advantages and Disadvantages of Microstrip Antennas

Microstrip antennas are well suited to the current emphasis on miniaturization and increased reliability. The antennas have been successfully adapted for use in systems ranging from biomedical diagnosis to satellite and aircraft communications [20:424].

The widespread use of microstrip antennas can be attributed to the numerous advantages they offer when compared to more traditional antenna types. Some of these advantages include low volume, weight, and fabrication cost, mechanical ruggedness, and compatibility with modular

designs, since solid state devices can be manufactured simultaneously and on the same circuit board as the antenna [23:2].

Some of the disadvantages associated with microstrip antennas include narrow bandwidth, antenna gains much less than unity, poor isolation between feed and radiating elements, and low power handling capability [1:2].

Narrow bandwidth is the most restrictive of these shortcomings. The bandwidth of a simple microstrip antenna is typically less than five percent of the resonant frequency [21:145]. The bandwidth of a microstrip antenna can be improved by reducing the permittivity or increasing the thickness of the antenna substrate [1:62]. However, using a low permittivity substrate degrades the performance of other solid state components etched on the same substrate as the antenna. Increasing substrate thickness detracts from the microstrip antenna's low profile, and causes difficulties in matching the antenna input impedance with that of the feed network [23:3].

1.3 *The Aperture-Fed, Stacked Patch Microstrip Antenna*

Several practical ways to overcome bandwidth limitations without compromising the advantages of the microstrip antenna have been tried and proven. The aperture-fed, stacked patch antenna (see Figure 1-1) is an effort to improve bandwidth by employing two of these techniques, the aperture-fed and stacked patch configurations, in a single design.

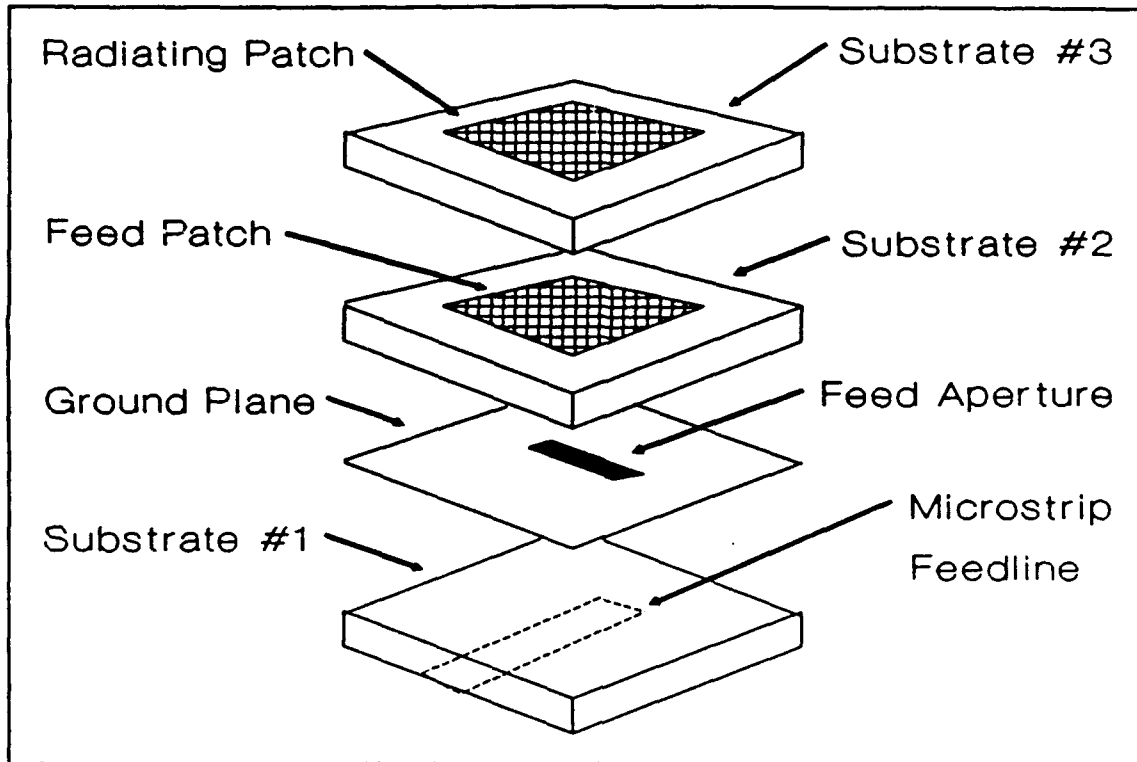


Figure 2-2 Geometry of the Aperture-Fed, Stacked Patch Microstrip Antenna

By placing the antenna patches on a substrate separated from other active circuit components, the aperture-fed configuration allows selection of substrate permittivity and thickness for maximum antenna performance without affecting the operation of other circuit elements. Additionally, placing the ground plane between the feed network and the radiating elements of the antenna overcomes the problem of poor isolation between spurious feed network and antenna radiation [31:936]. Because there is no physical connection between the feed network and the antenna, the aperture-fed configuration is simple to manufacture and consequently, very appealing for use in antenna arrays, especially those containing a large number of elements.

The use of the stacked patch configuration provides further bandwidth enhancement [23:3]. Proper selection of the additional dielectric layer's permittivity and thickness, as well as the shapes, sizes, and relative locations of the feed and radiating patches, can provide the additional benefits of enhanced gain or dual frequency operation [5:609].

1.4 Research Description

The aperture-fed, stacked patch microstrip antenna presents a complex analysis problem. One analysis has been completed by Nazar [23] using the mixed potential integral equation (MPIE) approach. Nazar's work provides the integral equations that can be used to calculate the currents and potentials on an aperture-fed, stacked patch microstrip antenna. However, the integral equations cannot be solved analytically; thus, a numerical solution is required.

1.4.1 Problem Statement. Develop the FORTRAN software necessary to calculate the electric surface currents and charge densities on the elements of an aperture-fed, stacked patch microstrip antenna.

1.4.2 Research Objectives and Scope. This effort uses Nazar's analysis as a basis for developing a Method of Moments (MoM) solution for the surface currents and charge densities on an aperture-fed, stacked patch microstrip antenna. With this solution, the radiated

fields and impedances characteristics of the antenna design can be calculated.

The product of this research is a software package that completes the MoM solution for a user specified aperture-fed, stacked patch microstrip antenna. The package is written in FORTRAN 77 and requires no external software to complete the solution. Results obtained with the package have been verified as much as possible using data available in current literature [18]. Descriptions explaining the use of the software and the design, coding, and logic of the solution are also provided.

1.4.3 Research Assumptions. Nazar's analysis uses Green's functions to characterize the interactions and radiation mechanisms of the aperture-fed, stacked patch antenna. By definition, the Green's functions are expressions for the potentials created by a unit electric or Hertz dipole located within one of the antenna's surfaces or ground plane. By expressing any arbitrary signal applied to the antenna as a spectrum of unit sources, the Green's functions can be used to calculate the resulting fields in the antenna [19:165]. With the fields known, it is then possible to calculate the radiated fields.

Nazar expresses the Green's functions as integral equations that are derived under the restrictions of each dielectric layer having finite thickness while being homogeneous, isotropic, and lossless. Additionally, the patch conductors and ground plane are infinitely thin, perfect conductors.

The software developed for this thesis does not explicitly evaluate the integral expressions for the aperture-fed, stacked patch microstrip antenna's Green's functions. Instead, the Green's functions are represented by appropriately chosen polynomials in accordance with the work of Erwert [8].

1.5 Summary of Current Knowledge

As previously discussed, Nazar has derived the Green's Functions necessary to model the aperture-fed, stacked patch microstrip antenna. His work combines the aperture-feed analysis of Sullivan and Schaubert [29] with the MPIE approach of Mosig and Gardiol [20] to derive the spatial Green's functions for the antenna. The MPIE approach is attractive because it fully characterizes the near-fields of the antenna including surface waves [23:ii]. The Green's functions for the antenna are expressed in the form of Sommerfeld integrals that can only be evaluated numerically. However, the numerical stability of the Green's functions allow the use of approximations for their values without unacceptable loss of accuracy [19:429;21:224-226]

The method of moments is a numerical technique that has been successfully used to solve a wide variety of electromagnetic radiation and scattering problems. The MoM approach provides a well understood means for converting a series of complex, integral equations into matrix equations that are easily solved on a digital computer. Furthermore,

the MoM technique has been used in microstrip antenna radiation solutions by numerous authors [16;22;24]. Sullivan and Schaubert [29] have successfully applied the method of moments in the analysis of an aperture-fed antenna, and Barlatey *et al.* [5] have employed the technique to obtain the MPIE solution of the stacked patch configuration.

1.6 Materials and Equipment Needed

Theoretically, the MoM software package can be executed on any computer system equipped with a FORTRAN 77 compiler. However, due to the large number of numerical integrations required by the MoM solution, a high speed computer is best suited for the task. In this study, the calculations were accomplished on the Air Force Institute of Technology, School of Engineering Digital Equipment Corporation VAX 8550 computer.

1.7 Thesis Organization

The remainder of this document is organized as follows. Chapter II presents a survey of literature focusing on current research efforts involving MPIE analysis of aperture-fed microstrip antennas, stacked patch microstrip antennas, or aperture-fed, stacked patch microstrip antennas and the use of the method of moments in obtaining solutions to microstrip antennas. Chapter III presents the equations needed to model

the antenna and the specifics of the MoM solution. Chapter IV discusses the numerical techniques needed to complete the MoM solution and a detailed description of the logic, algorithms, and FORTRAN code. Chapter V discusses the predictions made with the software and their accuracy as compared to data reported in the literature. Finally, the conclusions drawn from this research and recommendations for further work are presented in Chapter VI.

II. Current Efforts - Microstrip Antennas

This chapter presents a review of current microstrip analysis efforts relevant to the research of this thesis. To begin, a detailed discussion of aperture-fed and stacked patch microstrip antennas is presented with emphasis on the benefits of the configurations. Next, research on aperture-fed, stacked patch antennas is reviewed, and finally, applying the method of moments to solutions for microstrip antennas is discussed.

2.1 Aperture Fed Microstrip Antennas

The bandwidth performance of a microstrip antenna can be improved by either increasing the thickness or decreasing the relative permittivity of the dielectric substrate separating the conductors of the antenna [1:62]. However, these changes result in loss, radiation, and input impedance mismatch problems which would typically offset any bandwidth gains [23:3]. One way to take advantage of increased sub-

strate thickness while avoiding these problems is the aperture-fed microstrip antenna which was first proposed by D. M. Pozar [26].

Pozar's configuration places a ground plane between a microstrip feedline and a microstrip antenna patch (see Figure 2-1). The signal

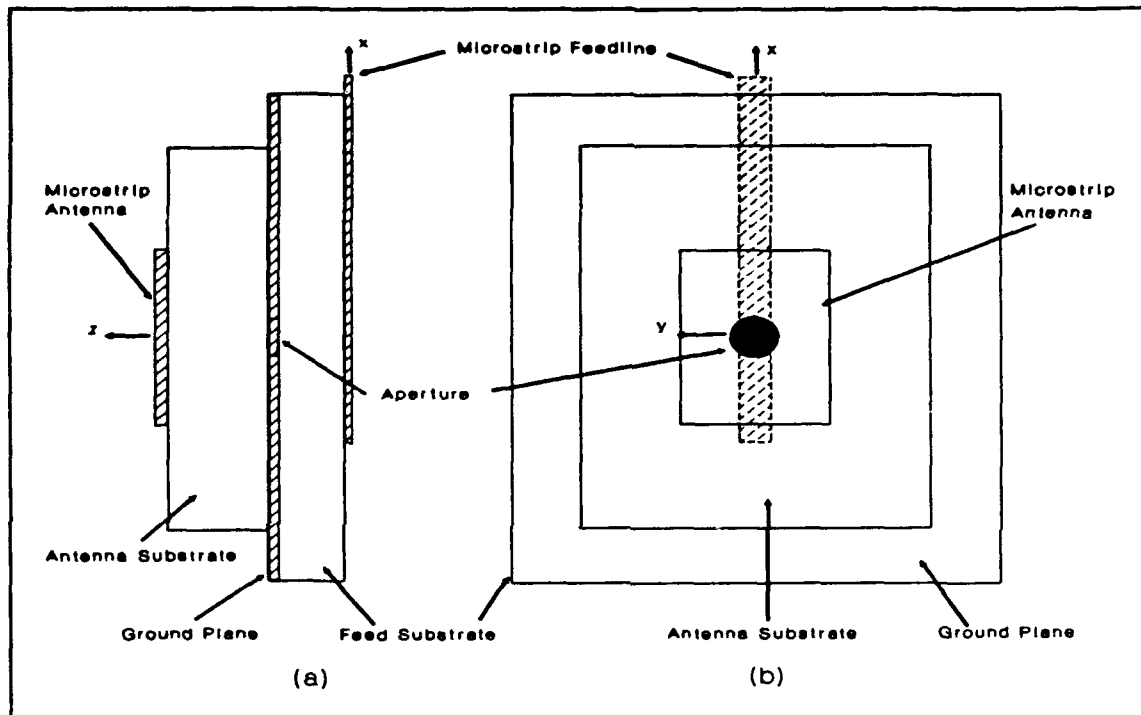


Figure 2-1 Side View (a) and Top View (b) of Pozar's Aperture-Fed Microstrip Antenna

applied to the microstrip feedline is electromagnetically coupled to the radiating patch, thus the aperture-fed configuration does not require a direct connection between the feedline and antenna. Pozar notes three advantages to this configuration:

- (i) The configuration is well suited for monolithic phased arrays, where active devices can be integrated on, for example, a gallium arsenide substrate with the feed network and the radiating elements can be located on an adjacent (low dielectric constant) substrate, and coupled to the feed

network through apertures in the ground plane separating the two substrates. The use of two substrates thus avoids the deleterious effect of a high-dielectric-constant on the bandwidth and scan performance of a printed antenna array.

(ii) No radiation from the feed network can interfere with the main radiation pattern, since a ground plane separates the two mechanisms.

(iii) No direct connection is made to the antenna elements, so problems such as large probe self-reactances or wide microstrip line (relative to patch size), which are critical at millimeter-wave frequencies, are avoided. [26:49]

Pozar uses the cavity model of a patch antenna and small hole coupling theory to analyze the aperture coupling and quantify the relationship between aperture placement and the coupling of energy to the radiating patch. Pozar found an aperture with a long y-dimension (see Figure 2-1) and a narrow x-dimension provides the strongest coupling between the feedline and radiating patch [25:50]. Also, varying the length of the feedline extending beyond the aperture and the aperture size provides two means of tuning the antenna [25:50]. Pozar suggests the use of as small an aperture as possible, while adjusting the feedline length to match the antenna input impedance with that of the feed circuit. While no bandwidth performance is reported, Pozar does note the design appears to be quite robust in terms of flexibility and ease of fabrication [25:49]. Measurements of a prototype antenna employing the aperture feed show the principal plane radiation patterns are basically the same as other microstrip antennas of the same geometry [25:50].

Sullivan and Schaubert [29] have completed a more detailed mathematical analysis of an aperture-fed microstrip antenna with a single

patch. Their analysis uses coupled integral equations and a Galerkin moment method to solve for the feedline electrical surface currents, the radiating patch electrical surface currents, and the equivalent magnetic surface currents on the ground plane. As part of this work, Sullivan and Schaubert used their model to investigate the effect of increased feedline thickness and relative permittivity. They report increased relative permittivity of the feedline substrate improved coupling, but left the resonant frequency of the antenna unchanged [29:982]. As feedline substrate thickness was increased, aperture coupling decreased while the resonant frequency of the antenna remained unchanged [29:982]. These results demonstrate the wide range of design flexibility offered by the aperture-fed antenna. Additionally, the analysis provides a means to predict antenna input impedance and resonant frequency based on aperture length and the thickness and dielectric constant of the feedline and antenna substrates.

2.2 Stacked Patch Microstrip Antennas

An example of a coaxially-fed, stacked patch microstrip antenna is shown in Figure 2-2. The lower patch of the antenna is referred to as the driven or feed patch. The upper patch is the radiating element and is excited by energy electromagnetically coupled from the driven patch. Because of this coupling mechanism, stacked patch antennas are also referred to as electromagnetically coupled patch (EMCP) antennas.

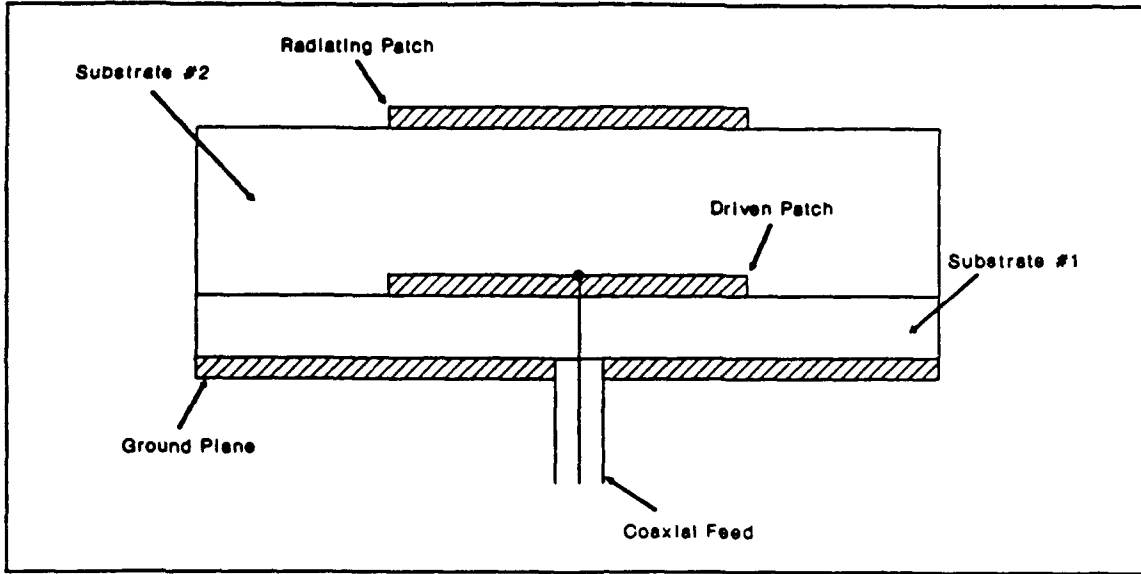


Figure 2-2 Coaxially-Fed, Stacked Patch Microstrip Antenna

Oltman and Huebner [25] first introduced the concept of electro-magnetically coupled microstrip radiators with a study of microstrip dipoles stacked near a microstrip feedline.

The study cites four advantages offered by the stacked configuration. Because of increased ground plane-radiator spacing, the stacked geometry provides greater bandwidth performance and increased radiation efficiency [25:151]. Experimental data reported in the study show bandwidth values between 2.5 and 5.5 percent for VSWR of 1.92 or higher [25:154].

A third advantage of the stacked geometry is reduced radiation from feedline bends, junctions, and other discontinuities. In the stacked geometry, the radiating element can be placed farther away from the feed circuitry, while the feed circuitry can be simultaneously located close to the ground plane. Since feedline radiation is directly

proportional to the separation between the feedline and ground plane, the feedline radiation is reduced [25:152].

The fourth advantage of the stacked geometry is the ease in matching the electromagnetically coupled radiator to its feedline. For a basic microstrip radiator, the radiator configuration that provides a perfect match is unique. Since the stacked geometry employs electric and magnetic field coupling, Oltman and Huebner describe the perfect match configuration as a near ellipsoidal surface, therefore the perfect match point is easier to achieve [25:152].

Sabban [28] expands on the stacked element concept by replacing the microstrip dipoles with patches. In Sabban's design, the lower patch is sized to resonate at center frequency, and the upper patch is slightly larger than the lower. A low permittivity material, such as air, is used to separate the patches. Several antennas were constructed and tested as single radiators and as array elements over the S to Ka frequency bands. Sabban reports adjustments to patch separation enable impedance matching between the antenna and the feed circuit over a wide frequency range [28:64]. Depending on the antenna geometry, bandwidths of 9 to 15 percent with VSWR less than 2:1 were obtained [28:64].

2.3 Aperture Fed, Stacked Patch Antennas

Tsao et al [31] combine the aperture feed and stacked patch configurations to achieve even larger antenna bandwidths. Their purpose

in using the aperture-fed antenna is two fold. First, the aperture-fed antenna is simpler to manufacture since no probe must be soldered to the antenna. Second, the ground plane separating the feed network and the antenna prevents interference between spurious feed network radiation and antenna radiation [31:936]. Proper selection of the thicknesses and permittivities of dielectric layers separating the antenna elements, employed in conjunction with appropriately selected geometries for the coupling aperture and microstrip patches, provides a means to meet various antenna bandwidths requirements [31:936]. Depending on desired polarization characteristics, bandwidths of 19.2 and 23 percent were obtained for VSWR less than 2 [31:936].

In [23], Nazar combines the MPIE and stratified media techniques to perform a detailed analysis of the aperture-fed, stacked patch antenna. Using the vector and scalar potentials for infinitesimal sources embedded in stratified media, Nazar derives a set of Green's functions in the form of Sommerfeld integrals expressed in terms of antenna spatial variables [23:13-39]. Nazar describes the characteristics of the Green's functions' integrands, discusses integrand problem areas, and provides FORTRAN software for numerical evaluation of the integrals [23:49-84]. Also, a technique for using the Green's functions in a method of moments solution for the antenna currents is described [23:39-48].

2.4 Microstrip Antenna Solutions Using the Method of Moments

As previously mentioned, the method of moments is a numerical technique widely used to solve electromagnetic problems. The MoM provides a well understood and easily implemented means of transforming linear functional equations, i.e. integral, differential, or integro-differential equations, into a matrix equation easily solved on a computer. The equation being transformed typically describes an appropriately selected boundary condition that must be satisfied. In the case of a microstrip antenna, the boundary condition is the requirement of all tangential electric field components summing to zero. While the MoM technique is a unique process, the methods by which each step of the process is completed are diverse and bear careful consideration. This review concentrates on past efforts that provide insight into choosing the features which provide the best compromise between accuracy and computational feasibility of the MoM solution.

As employed in microstrip antenna problems, the MoM breaks the scattering or radiating body into a collection of smaller bodies, typically referred to as cells. A simple approximation for the surface currents on each cell, referred to as a basis function, is proposed. Therefore, the surface currents of the complete body is the finite sum of appropriately weighted basis functions of each cell. The challenge of the MoM solution is determining the appropriate weight, or coefficient, for each cell's basis function. The basis function coefficients are found by replacing the original boundary condition with a set of

approximate ones, and then testing each basis function for satisfaction of the approximated boundary condition using a set of weights or testing functions [21:221].

The accuracy and computational feasibility of the MoM solution is determined by selection of the appropriate number of cells, basis functions, and testing functions. Typically, the accuracy of the MoM solution increases in direct proportion to the number of the cells on the body. However, the number of cells dictates the dimensions of the matrices in the MoM matrix equation, and there is a point where the increase in accuracy is offset by a penalty paid in increased computer processing time and memory requirements. Selecting the number of cells is then a trade between acceptable accuracy and demands on computer resources.

The accuracy of the MoM solution is also affected by how well the basis functions satisfy the surface current boundary conditions. While complex basis functions tend to improve accuracy, a penalty of increased computation difficulty must be paid [18:317].

Finally, selecting the appropriate test functions can also affect the MoM solution accuracy and complexity. Since the test functions are integrated against the basis function to form an inner-product, the complexity of the test function also dictates the complexity of the computations. Secondly, careful selection of testing functions may help to avoid integration difficulties if the fields exhibit singularities, such as those of the fields near the edges of a conductor.

In [18], Mosig addresses the issue of selecting the appropriate number of cells, basis functions, and testing functions for a radiating microstrip patch. In this research, Mosig used several schemes to divide an arbitrarily shaped patch while measuring the computation requirements and accuracy of the MoM solution for different combinations of basis and testing functions. To determine the best choices, Mosig considered computation speed and the ability to predict measured values of resonant frequency, quality factors, and input impedance for a patch resonator [18:322]. In this effort, the antenna patch was divided into rectangular cells referred to as charge cells, with two adjacent charge cells forming a current cell. For charge cells, Mosig found that using cells with an x-dimension of 0.05λ , along with the appropriate basis and testing functions provides solution accuracy of within one percent [18:320]. The y-dimension of the cells does not affect solution accuracy very much, and Mosig reports any number of transverse cells greater than 3 should prove adequate for engineering calculations [18:320]. The basis functions of choice are two-dimensional, rooftop functions defined over each current cell [18:318]. The x-directed surface currents and y-directed surface currents are expanded in independent sets of rooftop basis functions. With the rooftop basis functions, the best selection for testing functions are a unit pulse defined over the line segment connecting the centers of the two charge cells comprising a single current cell [18:318]. By defining the testing functions between charge cell centers, the need to evaluate the

fields near patch edges are avoided thus the field singularities at the edges will not adversely effect the MoM solution [20:427].

2.5 *Summary of Current Knowledge*

While microstrip antennas offer numerous advantages over conventional antennas, their applications are somewhat restricted due to limited bandwidth. Pozar's aperture feed technique and Sabban's stacked patch configuration provide methods to overcome these bandwidth limitations to an acceptable degree. Tsao *et al* have demonstrated the bandwidth improvements possible by combining the aperture feed and stacked patch configurations. Nazar's analysis of the aperture fed, stacked patch antenna provides the Green's functions and numerical techniques necessary to develop the method of moments solution for the antenna currents. Mosig's research in applying the MoM to microstrip radiators provides the means to maximize the accuracy of a MoM solution while minimizing computational requirements. Combining the results from Nazar and Mosig provides a proven approach for employing the MoM to find the electric surface currents on the aperture fed, stacked patch microstrip antenna.

III. Theory

This chapter discusses the use of the MPIE Green's functions and the method of moments to solve for the surface currents of the aperture-fed, stacked patch microstrip antenna. The complete antenna model is first described, and the equations needed to find the unknown surface currents on all four interfaces of the antenna are explained. The details of the MoM solution are described and the equations for the MoM matrix elements and characteristics of the resulting matrix equation are presented.

After the complete model of the antenna is derived, some of the challenges of completing the solution for all four planes of the antenna are discussed. Next, the full model is modified so that the MoM solution can be accomplished independent of the antenna excitation technique by using an approximation for the magnetic fields of the antenna aperture. The MoM matrix equation for the resulting 3-plane solution is then derived from the results for the full antenna model. Finally, an iterative technique for solving the MoM matrix equation and the equations needed to calculate the radiated fields of the antenna are discussed.

Throughout the remainder of this thesis, vector values will be designated by a single underline and a dyadic will be designated using a double underline.

3.1 The Antenna Model

The object of the analysis is to obtain expressions for the electric surface currents on the antenna. To begin the analysis, the electric and magnetic surface currents are defined as shown in Figure 3-1. The electric surface current on the microstrip feedline produced

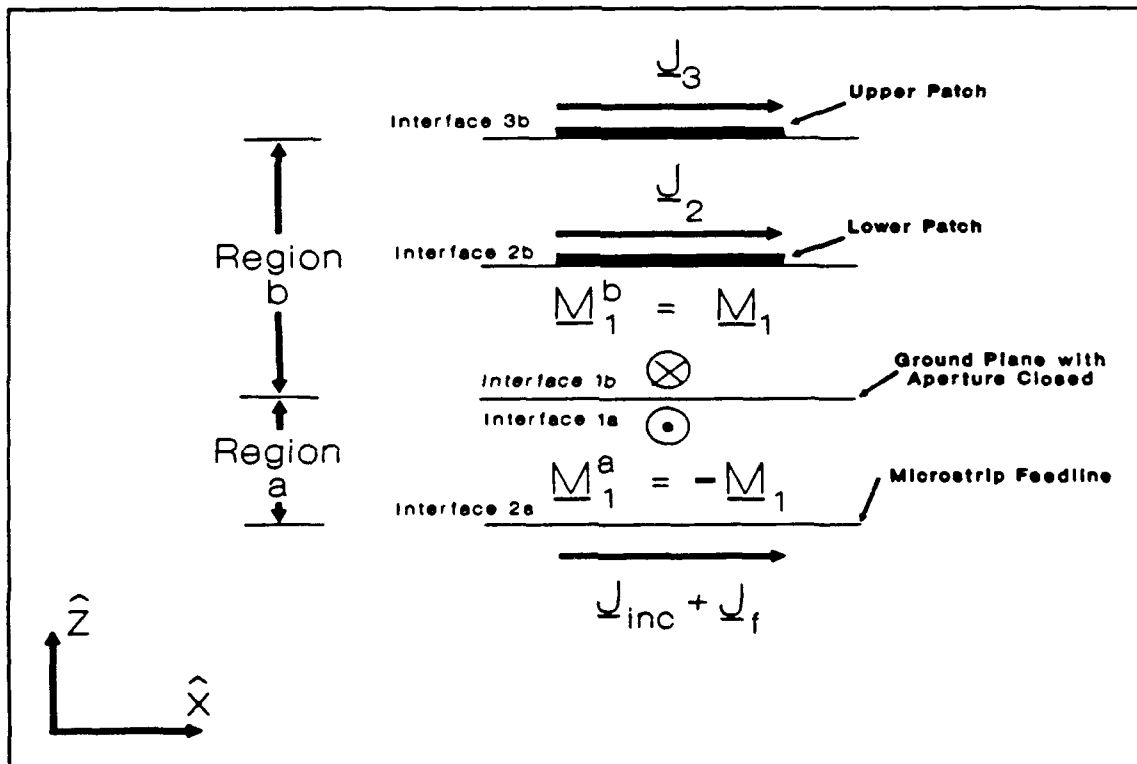


Figure 3-1 Equivalent Antenna Model With Incident and Induced Currents.

by the applied signal is defined as \underline{J}_{inc} , and the electric surface current on the feedline resulting from electric fields internally scattered by the antenna is defined as \underline{J}_f . The equivalence principle is used to replace the ground plane aperture with its equivalent magnetic surface current, \underline{M}_1 . To insure continuity of the tangential electric field through the aperture, the magnetic surface current below the ground plane, \underline{M}^a_1 , is defined as the negative of that above the ground plane, \underline{M}^b_1 [29:978]. The electric surface current vector on the patch immediately above the ground plane is defined as \underline{J}_2 and that of the uppermost patch is \underline{J}_3 . The space below the ground plane is designated region a ($z < 0$) and that above the ground plane is region b ($z > 0$). The antenna coordinate system's origin is located at the center of the aperture, with the x-axis extending parallel to the length of the microstrip feedline.

In region a, the feedline/dielectric interface is numbered 2a and the dielectric/ground plane interface is numbered 1a. In region b, the ground plane/dielectric interface is numbered 1b, the patch/dielectric interface immediately above the aperture is numbered 2b, and the uppermost patch/dielectric interface is numbered 3b. While only the x-components of the surface currents are shown in Figure 3-1, this solution considers both x- and y-directed surface currents.

The unknown surface currents \underline{J}_f , \underline{J}_2 , \underline{J}_3 , and \underline{M}_1 are found by solving the four MPIE equations that describe the boundary conditions for the tangential magnetic field of the aperture and tangential electric fields on the feedline and patches of the antenna. These

equations are written to satisfy the boundary conditions of Table 3-1 and are solved via the method of moments. The boundary conditions not shown in Table 3-1 are incorporated in the construction of the Green's functions for the antenna [23:16].

Table 3-1 Antenna Tangential Field Boundary Conditions [23]

- | | |
|----|---|
| 1) | $E^{\tan} = 0$ on the Patch of Interface 2b |
| 2) | $E^{\tan} = 0$ on the Patch of Interface 3b |
| 3) | $E^{\tan} = 0$ on the feedline |
| 4) | H^{\tan} is continuous through the aperture |

3.2 Tangential Electric Field Equations

Nazar's analysis provides the Green's function necessary to calculate the magnetic vector potential and electric scalar potential resulting from electric surface currents and electric surface charge density via a superposition integral taken over the source surface. For example, to find the magnetic vector and electric scalar potentials at interface 2b resulting from the electric surface currents and the electric charge density on interface 3b, the following integral expressions are used [23:15]

$$A_{23}^b(\rho) = \int_{S_{3b}} G_{A23}^b(R) \cdot J_3(\rho') ds' \quad (3-1)$$

$$V_{q23}^b(\rho) = \int_{S_{3b}} G_{q23}^b(R) q_3(\rho') ds'$$

where

$\underline{A}_{23}^b(\rho)$ - the magnetic vector potential produced on interface 2b by surface currents on interface 3b

$$R = |\rho - \rho'|$$

S_{3b} - the surface of the patch on interface 3b

$\underline{G}_{A23}^b(R)$ - the dyadic Green's function used to calculate the contribution to the magnetic vector potential on interface 2b created by the electric surface current on interface 3b

$V_{q23}^b(\rho)$ - the electric scalar potential on interface 2b created by the surface charge density of interface 3b

$\underline{G}_{q23}^b(R)$ - the Green's function used to calculate the contribution to the electric scalar potential at interface 2b created by the electric charge density on interface 3b

$q_3(\rho')$ - the surface charge density on the patch of interface 3b

The dot in the expression for the magnetic vector potential indicates the vector dot product of the dyadic Green's function and the electric surface current vector. The first numeral in each subscript identifies the interface where the field is observed and the second numeral identifies the interface where the source is located. The superscript *b* signifies the interfaces of interest are located in region b of Figure 3-1. The vectors ρ and ρ' are the position vectors of the observer and source points, respectively. Both vectors are a function of the cartesian coordinate pairs (x,y) and (x',y') or the cylindrical coordinate pairs (ρ,φ) and (ρ',φ') , respectively.

The general dyadic Green's function, $G_A^b(R)$ is defined

$$\underline{G}_A^b(R) = \begin{bmatrix} G_A^{bxx}(R)\hat{x}\hat{x} & G_A^{bxz}(R)\hat{x}\hat{y} \\ G_A^{byx}(R)\hat{y}\hat{x} & G_A^{byy}(R)\hat{y}\hat{y} \end{bmatrix} \quad (3-2)$$

Using the time dependence of $\exp(j\omega t)$ where $j = \sqrt{-1}$, the vector and scalar potentials are then used to calculate the tangential electric fields:

$$\underline{E} = -j\omega \underline{A} - \nabla V \quad (3-3)$$

The tangential electric fields generated by the magnetic surface currents of the aperture are found using the appropriate Green's functions as follows [23:39]:

$$\underline{E}_{21}^{\tan}(\underline{M}_1) = \int_{S_{1b}} \underline{G}_{E21}^b(R, \xi) \cdot \underline{M}_1(\rho') ds' \quad (3-4)$$

where

$\underline{G}_{E21}^b(R, \xi)$ - the dyadic Green's functions used to calculate the contribution to the electric field at interface 2b from the magnetic surface current of interface 1b

The variable ζ in equation (3-4) is the angle between the source direction and the direction to observer location, and is defined as follows:

$$\zeta = \begin{cases} \sin^{-1} \left[\frac{\rho \sin\varphi - \rho' \sin\varphi'}{R} \right]; & \text{x-directed sources} \\ \sin^{-1} \left[\frac{\rho \cos\varphi - \rho' \cos\varphi'}{R} \right]; & \text{y-directed sources} \end{cases} \quad (3-5)$$

On interface 2b, the tangential field is a sum of contributions from the electric surface currents on both patches and the magnetic surface current of the aperture. Using equations (3-1), (3-3), and (3-4), the integral equation for the tangential electric fields at interface 2b satisfying the first boundary condition of Table 3-1 is [23:40]

$$\begin{aligned} & -j\omega \int_{S_{2b}} G_{A22}^b(R) \cdot \underline{J}_2(\rho') dS' - \nabla^t \int_{S_{2b}} G_{q22}^b(R) q_2(\rho') dS' \\ & - j\omega \int_{S_{3b}} G_{A23}^b(R) \cdot \underline{J}_3(\rho') dS' - \nabla^t \int_{S_{3b}} G_{q23}(R) q_3(\rho') dS' \\ & + \int_{S_{1b}} G_{E21}^b(R, \zeta) \cdot \underline{M}_1(\rho') dS' = 0 \end{aligned} \quad (3-6)$$

where the superscript t on the del operator indicates the operation is applied only to the transverse observer coordinates, x and y in a cartesian system and ρ and φ in a cylindrical system.

Similarly, the integral equation for the tangential electric fields at interface 3b satisfying the second boundary condition of Table 3-1 is [23:40]

$$\begin{aligned}
 & -j\omega \int_{S_{2b}} G_{A32}^b(R) \cdot J_2(\rho') ds' - \nabla^t \int_{S_{2b}} G_{q32}^b(R) q_2(\rho') ds' \\
 & - j\omega \int_{S_{3b}} G_{A33}^b(R) \cdot J_3(\rho') ds' - \nabla^t \int_{S_{3b}} G_{q33}^b(R) q_3(\rho') ds' \\
 & + \int_{S_{1b}} G_{E31}^b(R, \xi) \cdot M_1(\rho') ds' = 0
 \end{aligned} \quad (3-7)$$

On the feedline of interface 2a, the tangential electric fields are the difference between the tangential fields created by the applied signal, the fields created by the reflected current, and the fields created by the magnetic currents of the aperture. The equation satisfying the third boundary condition of Table 3-1 is [23:41]

$$\begin{aligned}
 & -j\omega \int_{S_{2a}} G_{A22}^a(R) \cdot J_{inc}(\rho') ds' - \nabla^t \int_{S_{2a}} G_{q22}^a(R) q_{inc}(\rho') ds' \\
 & + j\omega \int_{S_{2a}} G_{A22}^a(R) \cdot J_f(\rho') ds' + \nabla^t \int_{S_{2a}} G_{q22}^a(R) q_f(\rho') ds' \\
 & + \int_{S_{1a}} G_{E21}^a(R, \xi) \cdot M_1(\rho') ds' = 0
 \end{aligned} \quad (3-8)$$

The final boundary condition of Table 3-1 requires a continuous tangential magnetic field through the aperture. Therefore, the tangential magnetic fields due to sources above the ground plane must equal those fields produced by sources below the ground plane. To calculate

the magnetic fields produced by the magnetic surface currents, the appropriate Green's functions are first integrated against the magnetic surface current vector and magnetic charge density to obtain the electric vector and magnetic scalar potentials [23:39]

$$\underline{E}(\rho) = \int_{S'} G_F(R) \cdot \underline{M}(\rho') ds' \quad (3-9)$$

$$V_m(\rho) = \int_{S'} G_m(R) q_m(\rho') ds'$$

where

$\underline{E}(\rho)$ - the electric vector potential

$G_F(\rho, \rho')$ - the dyadic Green's function used to calculate the contribution to the electric vector potential from the magnetic surface current

$G_m(\rho, \rho')$ - the Green's function used to calculate the contribution to the magnetic scalar potential from the magnetic charge density

$q_m(\rho')$ - the equivalent magnetic surface charge density

Using the electric vector and magnetic scalar potentials, the magnetic fields are then calculated from the relationship

$$\underline{H} = -j\omega \underline{E} - \nabla V_m \quad (3-10)$$

The contribution to the magnetic fields from the electric surface current vector are found by integrating the surface current vector against the appropriate Green's function in the same manner as equation (3-4).

In region a, the magnetic fields are created by the electric surface currents, \underline{J}_{inc} and \underline{J}_f , and the lower magnetic surface current of the aperture, \underline{M}_1^a . In region b, the magnetic fields are produced by the electric surface currents on both patches, \underline{J}_1 and \underline{J}_2 , and the aperture's upper magnetic surface current of the aperture, \underline{M}_1^b . The integral equation satisfying the fourth boundary condition of Table 3-1 is [23:41]

$$\begin{aligned}
 & \int_{S_{2a}} G_{H12}^a(R, \zeta) \cdot \underline{J}_{inc}(\rho') ds' + \int_{S_{2a}} G_{H12}^a(R, \zeta) \cdot \underline{J}_f(\rho') ds' \\
 & - j\omega \int_{S_{1a}} G_{F11}^a(R) \cdot \underline{M}_1(\rho') ds' - \nabla^t \int_{S_{1a}} G_{m11}^a(R) q_{m1}(\rho') ds' \\
 & - \int_{S_{2b}} G_{H12}^b(R, \zeta) \cdot \underline{J}_2(\rho') ds' + \int_{S_{3b}} G_{H13}^b(R, \zeta) \cdot \underline{J}_3(\rho') ds' \\
 & + j\omega \int_{S_{1b}} G_{F11}^b(R) \cdot \underline{M}_1(\rho') ds' + \nabla^t \int_{S_{1b}} G_{m11}^b(R) q_{m1}(\rho') ds'
 \end{aligned} \tag{3-11}$$

Equations (3-6), (3-7), (3-8), and (3-11) are the four equations that are solved simultaneously to obtain the unknown surface currents - \underline{J}_f , \underline{J}_1 , \underline{J}_2 , and \underline{M}_1 .

3.3 Details of the Method of Moments Solution

The first step of the MoM solution is the division of the patches, feedline, and aperture into rectangular areas referred to as charge cells. All charge cells are taken to be the same size and have dimensions $a \times b$, see Figure 3-2. Research completed by Mosig [18:320] has shown the most suitable charge cell dimensions are setting $a = 0.05\lambda$ and choosing b such that there are 3 or more charge cells across the plane in the y -direction. Having all cells the same size is not an absolute requirement, but doing so reduces the complexity and computation time for the solution [20:425].

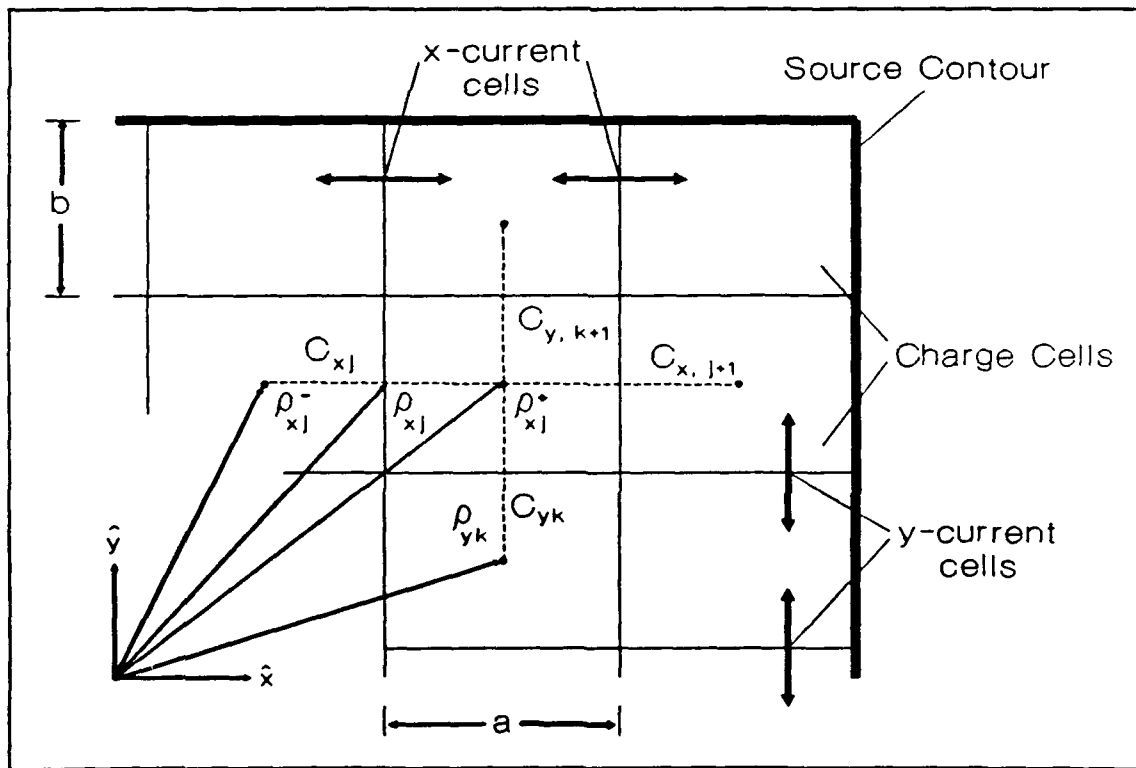


Figure 3-2 Geometry of the Antenna Charge and Current Cells

Two adjacent x-directed (y-directed) charge cells form an x-directed (y-directed) current cell. The x-directed line segment connecting the center of the j th charge cell and the adjacent charge cell to the right forms an x-directed test segment, C_{xj} . Similarly, the y-directed line segment connecting the center of the k th charge cell and the adjacent charge cell to the top forms a y-directed test segment, C_{yk} . This arrangement provides an overlap of current cells and means the number of current cells on the plane depends upon the number of charge cells. The exact relationship between the number of charge cells and current cells is not easily determined for an arbitrarily shaped source. However, for a rectangular patch with $m \times n$ charge cells, the number of x-directed current cells is given by $N_x = (m - 1)n$ and the number of y-directed cells is $N_y = m(n - 1)$ [20:426]. Any charge cell not on the perimeter of the source will support up to two x-directed current cells and two y-directed current cells.

The center of test segment C_{xj} and the j th x-directed current cell has position vector ρ_{xj} . The left and right ends of C_{xj} have position vectors ρ_{xj}^- and ρ_{xj}^+ , respectively. The position vectors for the test segment's ends are related to the center position vector through the relationships [20:426]

$$\rho'_{xj}^{\pm} = \rho'_{xj} \pm \hat{x} \left[\frac{a}{2} \right] \quad (3-12)$$

where \hat{x} is the x-directed unit vector.

Similarly, the y-directed test segment C_{yk} has position vectors ρ_{yk} , $\hat{\rho}_{yk}$, and $\hat{\rho}^+_{yk}$. The vector $\hat{\rho}_{yk}$ identifies the position of the center of the lower charge cell in the current cell and $\hat{\rho}^+_{yk}$ identifies the position of the center in the upper cell. The relationship between the position vectors of C_{yk} is given by equation (3-12) by exchanging $b \leftrightarrow a$ and $y \leftrightarrow x$.

3.3.1 Basis and Test Functions. To obtain the most general solution, no *a priori* assumptions are made concerning the distribution of currents on the conductors and aperture. This stipulation eliminates the possibility of using entire domain basis functions in the method of moments solution [20:425]. Previous comparisons of various subdomain basis functions have shown that rooftop functions, see Figure 3-3, can provide an acceptable representation for the surface currents while maintaining relative simplicity in the MoM impedance element calculations [18:320].

Each x-directed current cell supports a single rooftop function, $T_x(\rho')$, described by

$$T_x(x') = \begin{cases} 1 - \frac{|x'|}{a} ; & |x'| < a, |y'| < \frac{b}{2} \\ 0 & ; \text{Otherwise} \end{cases} \quad (3-13)$$

where

$$\begin{aligned} x' &= \hat{x} \cdot (\rho' - \rho'_{xj}) \\ y' &= \hat{y} \cdot (\rho' - \rho'_{xj}) \end{aligned} \quad (3-14)$$

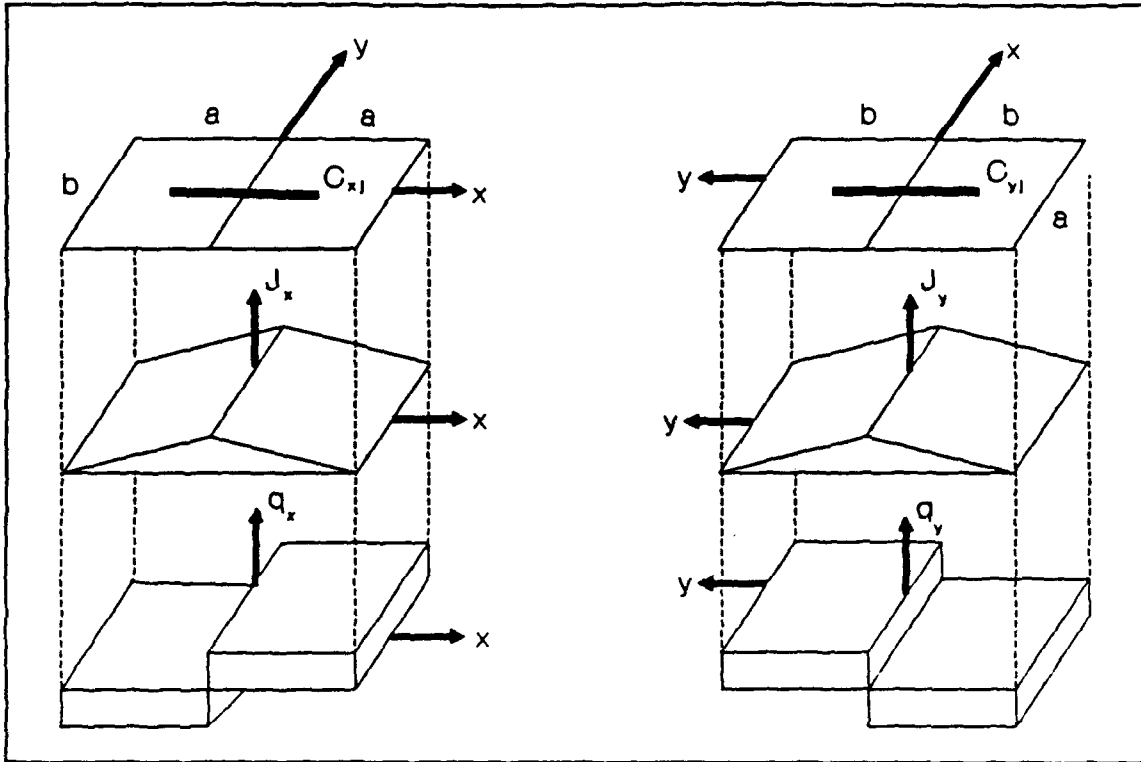


Figure 3-3 Surface Current Rooftop Basis Functions and Surface Charge Pulse Doublet Basis Functions for x- and y-directed Current Cells

Similarly, each y-directed current cell supports a rooftop basis function $T_y(y')$. The expression for $T_y(y')$ is obtained by interchanging $a \leftrightarrow b$ and $x \leftrightarrow y$ in equation (3-13).

Using the rooftop basis functions, the electric currents are expanded in the finite series

$$J(\rho') = \hat{x} \frac{1}{b} \sum_{j=1}^{N_x} \alpha_j T_x(x') + \hat{y} \frac{1}{a} \sum_{j=N_x+1}^N \alpha_j T_y(y') \quad (3-15)$$

where

α_j = the unknown surface current expansion coefficients

All four unknown surface currents are expanded in the same manner. The expansion coefficients, α_j , for surface current \underline{J}_f are identified by superscript f , the coefficients for magnetic surface current \underline{M}_1 by superscript 1 , the coefficients of \underline{J}_2 by superscript $b2$, the coefficients of \underline{J}_3 by superscript $b3$, and the coefficients of \underline{J}_{inc} by superscript inc .

As discussed by Mosig and Gardiol [20:426], the factors of $1/a$ and $1/b$ in the expressions for the surface currents give the coefficients the units of a current. In fact, the coefficients quantify the total current flowing across the adjacent boundary of the two charge cells that form each current cell [20:426].

To expand the electric surface charge density, the surface current expansion is substituted into the continuity equation

$$\nabla \cdot \underline{J} + j\omega q = 0 \quad (3-16)$$

and the surface charge density expansion is [20:426]

$$q(\rho') = \frac{1}{j\omega ab} \left[\sum_{j=1}^{N_x} \alpha_j \Pi_x(x') + \sum_{j=N_x+1}^N \alpha_j \Pi_y(y') \right] \quad (3-17)$$

The functions $\Pi_x(x') = -\nabla^t \cdot T_x(x')$ and $\Pi_y(y') = -\nabla^t \cdot T_y(y')$ are x - and y -directed pulse doublets described as follows:

$$\Pi_x(\rho') = \begin{cases} 1; & 0 \leq x' < a, |y'|' < \frac{b}{2} \\ -1; & -a < x' < 0, |y'| < \frac{b}{2} \\ 0; & \text{Otherwise} \end{cases} \quad (3-18)$$

$$\Pi_y(\rho') = \begin{cases} 1; & |x'| < \frac{a}{2}, -b < y' < 0 \\ -1; & |x'| < \frac{a}{2}, 0 \leq y' < b \\ 0; & \text{Otherwise} \end{cases}$$

where x' and y' are defined by equation (3-14).

The charge density of a single charge cell can be calculated from the expansion coefficients of all the current cells sharing the charge cell. For example, for the j th charge cell identified by the position vector ρ_{xj} , see Figure 3-2, the charge q_j is calculated using [20:426]

$$q_j = \frac{1}{j\omega ab} [\alpha_{x,j+1} - \alpha_{x,j} + \alpha_{y,k+1} - \alpha_{y,k}] \quad (3-19)$$

where the subscript of each coefficient is taken from the test segments adjoining the adjacent charge cell centers. The subscripts j and $j+1$ indicate the expansion coefficients belonging to the current cells formed by the charge cell of interest and the charge cell to the immediate left, subscript j , and the charge cell to the immediate right, subscript $j+1$. Similarly, the coefficient k identifies the coefficient for the current cell formed by the charge cell of interest and the

charge cell immediately below, and the subscript $k+1$ identifies the coefficient for the current cell formed by the charge cell of interest and the charge cell immediately above.

Figure 3-3 shows the relationship between the charge cells, current cells, rooftop functions, and pulse doublets for both x- and y-directed current cells.

Using the same rooftop function and pulse doublet functions, the expansions for the magnetic surface currents and charge densities are obtained.

With rooftop basis functions, a practical choice for test functions are unidimensional, rectangular pulses [18:318;20:426]. These pulse test functions provide a simple means to complete the required inner-products for the MoM solution without sacrificing accuracy of the results. The test functions are defined only along the paths from ρ_{xj}^- to ρ_{xj}^+ on x-directed current cells and ρ_{yk}^- to ρ_{yk}^+ on y-directed current cells. By defining the test segments along these paths, the need to compute field values near the plane's edges is eliminated, thereby avoiding field singularities that adversely effect the accuracy of the MoM solution [20:427].

Now, define an inner-product for the x-directed test function, $w_j(x)$ and any general vector function $G(r)$ such that

$$\langle w_j(x), G(r) \rangle = \int_{C_{xj}} w_j(x) \cdot G(r) dx \quad (3-20)$$

Similarly, $\langle \underline{w}_k(y), \underline{G}(\rho, \rho') \rangle$ is defined with integration along the path C_{yk} . Since the test functions selected for this solution are a unidimensional, rectangular pulse of amplitude one, the inner products reduce to integrations of the function $G(r)$ along the appropriate path.

3.3.2 Converting Integral Equations to Matrix Equations. Following the standard procedure of the method of moments, the surface current and charge density expansions, equations (3-15) and (3-17), are substituted into the integral equations (3-6), (3-7), (3-8) and (3-11). Next, an inner-product of the integral equations with test functions are taken, and these inner-products form the elements of the matrices in the MoM matrix equation.

However, before proceeding with the substitution and statement of the matrix forms of the integral equations, a simplification for the field contributions from the surface charges should be discussed. Consider the fourth term of equation (3-6) which is the expression for the tangential electric field on interface 2b created by the surface charge density on interface 2b:

$$\underline{E}_{22}^b(q_2) = -\nabla^t \int_{S_{3b}} G_{q22}^b(R) q_2(\rho') ds' \quad (3-21)$$

Note that this expression contains a gradient operation with respect to the transverse observer coordinates x and y.

Now take the inner-product, as defined by equation (3-20), along the path C_{xj} with $\underline{w}_j(x) = 1$ and $\underline{G}(r) = \underline{E}_{22}^b(q_2)$

$$\begin{aligned} \langle \underline{w}_j(x), \underline{E}_{22}^b(q_2) \rangle = & - \int_{C_{x_j}} \underline{dl} \cdot \nabla^t \int_{S_{3b}} G_{q22}^b(R) q_2(\rho') ds' \\ & - \int_{S_{3b}} \left[\int_{C_{x_i}} \nabla^t G_{q22}^b(R) \cdot \underline{dl} \right] q_2(\rho') ds' \end{aligned} \quad (3-22)$$

The fact that the gradient is taken with respect to the observer or unprimed coordinates allows an exchange in the order of operations in the inner-product. Since the contour C_{x_j} is the path from $\rho^-_{x_j}$ to $\rho^+_{x_j}$, the bracketed integral in the center of equation (3-22) can be simplified to the difference of the G_{q22}^b evaluated at the endpoints of C_{x_j} , $\rho^+_{x_j}$ and $\rho^-_{x_j}$.

With these simplifications, the inner-product of the fields created by the surface charge and the test functions are

$$\langle \underline{w}_i(x), \underline{E}_{22}^b(q_2) \rangle = - \int_{S_{3b}} [G_{q22}^b(\rho^+_{x_i}, \rho') - G_{q22}^b(\rho^-_{x_i}, \rho')] q_2(\rho') ds' \quad (3-23)$$

Using the inner products as expressed in equation (3-23) and the expansion for the surface currents and charge density given by equations (3-15) and (3-17) equation (3-6) describing the fields at interface 2b can be written

$$\begin{aligned}
& \sum_{i=1}^{N_2} \sum_{j=1}^{N_2} \left\{ \begin{array}{l} \frac{j\omega}{t_{2j}} \int_{C_{2i}} \cdot \underline{dl} \int_{S_{2j}} G_{A22}^b(R_{ij}) \cdot \underline{T}(\gamma_j) ds' \\ + \frac{1}{j\omega a_2 b_2} \int_{S_{2j}} [G_{q22}^b(R_{ij}^+) - G_{q22}^b(R_{ij}^-)] \Pi(\gamma_j) ds' \end{array} \right\} \alpha_j^{b2} \\
& - \sum_{i=1}^{N_2} \sum_{j=1}^{N_3} \left\{ \begin{array}{l} \frac{j\omega}{t_{3j}} \int_{C_{2i}} \cdot \underline{dl} \int_{S_{3j}} G_{A23}^b(R_{ij}) \cdot \underline{T}(\gamma_j) ds' \\ + \frac{1}{j\omega a_3 b_3} \int_{S_{3j}} [G_{q23}^b(R_{ij}^+) - G_{q23}^b(R_{ij}^-)] \Pi(\gamma_j) ds' \end{array} \right\} \alpha_j^{b3} \\
& - \sum_{i=1}^{N_2} \sum_{j=1}^{N_1} \left\{ \frac{j\omega}{t_{1j}} \int_{C_{2i}} \cdot \underline{dl} \int_{S_{1j}} G_{E21}^b(R_{ij}, \xi) \cdot \underline{T}(\gamma_j) ds' \right\} \alpha_j^1 = 0
\end{aligned} \tag{3-24}$$

where

$$C_{si} = C_{xi}; \quad 1 \leq i \leq N_{sx}; \quad s = 1, 2, 3$$

$$C_{si} = C_{yi}; \quad N_{sx} < i \leq N_s; \quad s = 1, 2, 3$$

N_1, N_2, N_3 = the total number of current cells on interface 1a and interface 1b, interface 2b, and interface 3b, respectively

$$t_{sj} = a_s; \quad 1 \leq j \leq N_{sx}, \quad s = 1, 2, 3$$

$$t_{sj} = b_s; \quad N_{sx} < j \leq N_s, \quad s = 1, 2, 3$$

$$\underline{dl} = \hat{x} dx; \quad 1 \leq i \leq N_{sx}, \quad s = 1, 2, 3$$

$$\underline{dl} = \hat{y} dy; \quad N_{sx} < i \leq N_s, \quad s = 1, 2, 3$$

j = index of the current cell on the source plane

i = index of the current cell on the observer plane

$$R_{ij} = |\rho_i - \rho'_j|$$

$$R_{ij}^+ = |\rho_i^+ - \rho'_j|, \quad R_{ij}^- \text{ is defined similarly}$$

ρ'_{xi} and ρ''_{xi} = the position vectors of the endpoints of test segment C_{xi} as defined in equation (3-12)

and

$$\left. \begin{aligned} \gamma_j &= \left\{ \begin{array}{l} \hat{x} \cdot (\rho' - \rho'_{xj}), 0 \leq j \leq N_{sx} \\ \hat{y} \cdot (\rho' - \rho'_{yj}), N_{sx} < j \leq N_s \end{array} \right\} \\ T(\gamma_j) &= \left\{ \begin{array}{l} \hat{x} T_x(\gamma_j); 0 \leq j \leq N_{sx} \\ \hat{y} T_y(\gamma_j); N_{sx} < j \leq N_s \end{array} \right\} \\ \Pi(\gamma_j) &= \left\{ \begin{array}{l} \Pi_x(\gamma_j); 0 \leq j \leq N_{sx} \\ \Pi_y(\gamma_j); N_{sx} < j \leq N_s \end{array} \right\} \end{aligned} \right\} s = 1, 2, 3 \quad (3-25)$$

Equation (3-24) can be written using matrices as follows:

$$[Z_{ij}^{b22}] [\alpha_j^{b2}] + [Z_{ij}^{b23}] [\alpha_j^{b3}] - [C_{ij}^{b21}] [\alpha_j^1] = 0 \quad (3-26)$$

where Z indicates impedance matrices with units of ohms per unit length, C indicates coupling matrices with units of length^{-1} [23:45], and the superscripts are assigned in accordance with previous conventions.

The same substitutions and simplifications for equation (3-6), which describes the fields on interface 3b, produces

$$\begin{aligned}
& \sum_{i=1}^{N_3} \sum_{j=1}^{N_2} \left\{ \begin{array}{l} \frac{j\omega}{t_{2j}} \int_{C_{3i}} \underline{dl} \cdot \int_{S_{2j}} G_{A32}^b(R_{ij}) \cdot \underline{I}(\gamma_j) ds' \\ + \frac{1}{j\omega a_2 b_2} \int_{S_{2j}} [G_{q32}^b(R_{ij}^+) - G_{q32}^b(R_{ij}^-)] \Pi(\gamma_j) ds' \end{array} \right\} \alpha_j^{b2} \\
& - \sum_{i=1}^{N_3} \sum_{j=1}^{N_3} \left\{ \begin{array}{l} \frac{j\omega}{t_{3j}} \int_{C_{3i}} \underline{dl} \cdot \int_{S_{3j}} G_{A33}^b(R_{ij}) \cdot \underline{I}(\gamma_j) ds' \\ + \frac{1}{j\omega a_3 b_3} \int_{S_{3j}} [G_{q33}^b(R_{ij}^+) - G_{q33}^b(R_{ij}^-)] \Pi(\gamma_j) ds' \end{array} \right\} \alpha_j^{b3} \\
& - \sum_{i=1}^{N_2} \sum_{j=1}^{N_1} \left\{ \frac{j\omega}{t_{1j}} \int_{C_{3i}} \underline{dl} \cdot \int_{S_{1j}} G_{E31}^b(R_{ij}, \xi) \cdot \underline{I}(\gamma_j) ds' \right\} \alpha_j^1 = 0
\end{aligned} \tag{3-27}$$

The equivalent matrix equivalent for equation (3-27) is

$$[Z_{ij}^{b32}] [\alpha_j^{b2}] + [Z_{ij}^{b33}] [\alpha_j^{b3}] - [C_{ij}^{b31}] [\alpha_j^1] = 0 \tag{3-28}$$

Before substituting the expansion for the surface current and charge density into the equation for the fields of interface 2a, the terms are rearranged so that the known quantity J_{inc} is on the right of the equal sign. Using the subscript f to identify variables associated with the microstrip feedline, equation (3-8) can be written

$$\begin{aligned}
& \sum_{i=1}^{N_f} \sum_{j=1}^{N_1} \left\{ \frac{j\omega}{t_{1j}} \int_{C_{f1}} \underline{dl} \cdot \int_{S_{1j}} G_{E21}^a(R_{ij}, \zeta) \cdot \underline{T}(\gamma_j) ds' \right\} \alpha_j^1 \\
& + \sum_{i=1}^{N_f} \sum_{j=1}^{N_f} \left\{ \begin{array}{l} \frac{j\omega}{t_{ij}} \int_{C_{f1}} \underline{dl} \cdot \int_{S_{ij}} G_{A22}^b(R_{ij}) \cdot \underline{T}(\gamma_j) ds' \\ + \frac{1}{j\omega a_f b_f} \int_{S_{ij}} [G_{q22}^b(R_{ij}^+) - G_{q22}^b(R_{ij}^-)] \Pi(\gamma_j) ds' \end{array} \right\} \alpha_j^f \quad (3-29) \\
& - \sum_{i=1}^{N_f} \sum_{j=1}^{N_f} \left\{ \begin{array}{l} \frac{1}{t_{ij}} \int_{C_{f1}} \underline{dl} \cdot \int_{S_{ij}} G_{A22}^a(R_{ij}) \cdot \underline{T}(\gamma_j) ds' \\ + \frac{1}{j\omega a_f b_f} \int_{S_{ij}} [G_{q22}^a(R_{ij}^+) - G_{q22}^a(R_{ij}^-)] \Pi(\gamma_j) ds' \end{array} \right\} \alpha_j^{inc}
\end{aligned}$$

which produces the matrix equation

$$[C_{ij}^{a21}] [\alpha_j^1] + [Z_{ij}^{a22}] [\alpha_j^f] - [Z_{ij}^{a22}] [\alpha_j^{inc}] \quad (3-30)$$

Finally, equation (3-11) describing the continuity of the aperture magnetic fields becomes

$$\begin{aligned}
& \sum_{i=1}^{N_1} \sum_{j=1}^{N_2} \left\{ \frac{j\omega}{t_{2j}} \int_{c_{ij}} dl \cdot \int_{s_{ij}} G_{H12}^b(R_{ij}, \zeta) \cdot T(\gamma_j) ds' \right\} \alpha_j^{b2} \\
& + \sum_{i=1}^{N_1} \sum_{j=1}^{N_2} \left\{ \int_{c_{ij}} dl \cdot \int_{s_{ij}} G_{H13}^b(R_{ij}, \zeta) \cdot T(\gamma_j) ds' \right\} \alpha_j^{b3} \\
& + \sum_{i=1}^{N_1} \sum_{j=1}^{N_1} \left\{ \begin{array}{l} \frac{j\omega}{t_{1j}} \int_{c_{ij}} dl \cdot \int_{s_{ij}} G_{F11}^a(R_{ij}) \cdot T(\gamma_j) ds' \\ + \frac{1}{j\omega a_1 b_1} \int_{s_{ij}} [G_{a11}^a(R_{ij}) - G_{b11}^a(R_{ij})] \Pi(\gamma_j) ds' \end{array} \right\} \alpha_j^1 \\
& + \sum_{i=1}^{N_1} \sum_{j=1}^{N_1} \left\{ \begin{array}{l} \frac{1}{t_{1j}} \int_{c_{ij}} dl \cdot \int_{s_{ij}} G_{F11}^b(R_{ij}) \cdot T(\gamma_j) ds' \\ + \frac{1}{j\omega a_1 b_1} \int_{s_{ij}} [G_{a11}^b(R_{ij}) - G_{b11}^b(R_{ij})] \Pi(\gamma_j) ds' \end{array} \right\} \alpha_j^1 \\
& - \sum_{i=1}^{N_1} \sum_{j=1}^{N_1} \left\{ \frac{j\omega}{t_{fj}} \int_{c_{ij}} dl \cdot \int_{s_{ij}} G_{H12}^a(R_{ij}, \zeta) \cdot T(\gamma_j) ds' \right\} \alpha_j^f \\
& - \sum_{i=1}^{N_1} \sum_{j=1}^{N_1} \left\{ \frac{j\omega}{t_{fj}} \int_{c_{ij}} dl \cdot \int_{s_{ij}} G_{H12}^b(R_{ij}, \zeta) \cdot T(\gamma_j) ds' \right\} \alpha_j^{inc}
\end{aligned} \tag{3-31}$$

The third and fourth double summations of equation (3-31) describe admittance matrices, denoted by a Y, with units of mhos per unit length [23:46]. The matrix form of equation (3-31) is

$$[C_{ij}^{b12}][\alpha_j^{b2}] + [C_{ij}^{b13}][\alpha_j^{b3}] + [Y_{ij}^{11}][\alpha_j^1] - [C_{ij}^{a12}][\alpha_j^f] - [C_{ij}^{a12}][\alpha_j^{inc}] \tag{3-32}$$

where

$$[Y_{ij}^{11}] = [Y_{ij}^{a11}] + [Y_{ij}^{b11}] \tag{3-33}$$

These four matrix equations are solved simultaneously to form the MoM matrix equation. The impedance, coupling, and admittance matrices of equations (3-26), (3-28), (3-30), and (3-32) are sub-matrices in the MoM solution matrix. The complete MoM matrix equation is

$$\begin{bmatrix} [Z_{ij}^{b22}] & [Z_{ij}^{b23}] & -[C_{ij}^{b21}] & [0] \\ [Z_{ij}^{b32}] & [Z_{ij}^{b33}] & -[C_{ij}^{b31}] & [0] \\ [C_{ij}^{b12}] & [C_{ij}^{b13}] & [Y_{ij}^{11}] & -[C_{ij}^{a12}] \\ [0] & [0] & [C_{ij}^{a21}] & [Z_{ij}^{a22}] \end{bmatrix} \begin{bmatrix} [\alpha_j^{b2}] \\ [\alpha_j^{b3}] \\ [\alpha_j^1] \\ [\alpha_j^f] \end{bmatrix} = \begin{bmatrix} [0] \\ [0] \\ [C_{ij}^{a12}] \\ [Z_{ij}^{a22}] \end{bmatrix} [\alpha_j^{inc}] \quad (3-34)$$

3.3.3 Properties of the MoM Solution Matrix. The diagonal sub-matrices in the MoM solution matrix of equation (3-34) characterize the contributions to the tangential fields on an interface created by surface currents located on the same interface. The diagonal terms of each of these sub-matrices characterize the fields of a current cell caused by the currents in that same cell. These self-impedance are the strongest and thus, each sub-matrix and the solution matrix is diagonally dominant [23:47]. While the MoM impedance matrix is considerably large, it can be inverted using standard Gaussian elimination [20:427]. However, a solution using an iterative scheme offers a savings in computer processing time [17:271].

The position of each sub-matrix of the solution matrix determines its role in describing the tangential fields. The row index identifies the observer location with rows 1 through 4 corresponding to interfaces

2b, 3b, 1a and b, and 2a, respectively. The column index identifies the source location with the same order as the row index. Thus, the sub-matrix located in row 1 and column 2 characterizes the fields observed on interface 2b resulting from sources located on interface 3b. The zero sub-matrices identify locations in the antenna where sources do not contribute to observed fields. For instance, the zero matrix in row 2, column 4 signifies the sources of interface 2a do not contribute to the fields observed at interface 3b.

The number of rows in each sub-matrix is determined by the total number of current cells on the observer plane, and the number of columns is determined by the total number of current cells in the source plane. Each diagonal sub-matrix will be a square matrix because the observer and source planes are the same for these matrices. Since each source and observer plane is represented in both dimensions of the solution matrix, the solution matrix is a square matrix with its dimension in either direction being equal to the sum of the current cells on all four interfaces of the antenna.

3.4 Challenges of the MoM Solution

Completing the MoM solution for the entire antenna is an arduous process. Before any calculations on the MoM solution are possible, the Sommerfeld integrals defining the Green's functions must be evaluated, and the expansion coefficients for J_{inc} must be calculated.

3.4.1 Evaluating the Antenna's Green's Functions. Due to the numerical complexity of evaluating the Sommerfeld integrals, the Green's functions for the antenna will not be explicitly evaluated in the software written to complete the MoM solution.

As shown by Nazar [23:74-84] and discussed by Mosig and Gardiol [21:224-226], the Green's functions are dependent only on kR , where k is the wavenumber of the input signal. The Green's function can therefore be evaluated at a finite number of points within a range of kR and interpolation can be used to find the Green's functions anywhere within the interval [19:429;19:224].

The approach used here will be to employ polynomial representations of the general Green's functions as presented by Erwert [9]. When the asymptotic form of a Green's function for $R \rightarrow 0$ is needed a combination of interpolation from tabulated data and an analytic term will be used. The asymptotic approximations are discussed in Sections 3.4.1.1 and 3.4.1.2. The approximations of the Green's functions are either sixth-order polynomials or a combination of an eighth or tenth-order polynomials. Because the Green's functions are also dependent on the applied signal's wavenumber, different polynomials must be used as the input frequency is varied.

3.4.1.1 Asymptotic Green's Functions for $R \rightarrow 0$. For the case when source and observer locations are coplanar and on the same current cell, the value of R will approach zero. Since the Sommerfeld integrals defining the Green's functions contain Hankel functions of the second kind, the integral will be undefined when $R \rightarrow 0$. To overcome the

singularity at zero, Nazar derived an asymptotic form for the Sommerfeld integrals of interest - $G_b^b A_{22}$, $G_b^b A_{33}$, $G_b^b q_{22}$ and $G_b^b q_{33}$. The asymptotic expression involves two integrals of Bessel functions over finite intervals and a constant term proportional to R^{-1} . For example, the asymptotic form of the Green's functions describing x-directed fields on interface 2b created by x-directed surface currents on interface 2b is given by [23:59]

$$G_{A22}^{bxx}(R) \approx \frac{\mu_{1b}}{2\pi} \left\{ \int_0^{\lambda_c} \frac{J_0(\lambda R) \lambda}{D_b^b(\lambda)} \left[u_{2b} \cosh(u_{2b}(b_{2b} - b_{1b})) + \mu_{b23} u_{3b} \sinh(u_{2b}(b_{2b} - b_{1b})) \right] d\lambda - \frac{1 + \mu_{b23}}{1 + \mu_{b13} + \mu_{b12} + \mu_{b23}} \int_0^{R\lambda_c} \frac{J_0(x)}{R} dx + \frac{1 + \mu_{b23}}{R(1 + \mu_{b13} + \mu_{b12} + \mu_{b23})} \right\} \quad (3-35)$$

The variables in the first and third terms of equation (3-35) are defined on the first page of Appendix A.

The integrals of equation (3-35) are now over finite intervals, are therefore finite for all R , and can be evaluated numerically. The third term of the approximation must be integrated analytically over the surface of the source for use in the method of moments solution. The evaluation of the integral is the subject of the following section.

3.4.1.2 Evaluating the Analytic Term in the Asymptotic Green's Function Expression. With the rooftop basis functions, the integral defining the surface integration over the j th x-directed current cell for the R^{-1} term in the asymptotic expression is given by

$$I(R) = \int_{x_j} \int_{S_{x_j}} \frac{1}{R} \left[1 - \frac{|x' - x_j|}{a} \right] ds' dx \quad (3-36)$$

where

x_j, y_j = the x - and y -components of the cell's position vector.

$$ds' = dy' dx'$$

$$R = [(x - x')^2 + (y_j - y')^2]^{\frac{1}{2}}$$

Completing the surface integration produces the expression

$$I = b^2 \left\{ \begin{array}{l} \frac{9\tau^2}{4} \operatorname{csch}^{-1}(3\tau) + c_1 \sinh^{-1}(3\tau) - \frac{\tau^2}{12} \operatorname{csch}^{-1}(\tau) + c_2 \sinh^{-1}(\tau) \\ + \frac{1}{2} (3\tau^2 + 1)^{-\frac{1}{2}} - \frac{1}{6} (\tau^2 + 1)^{-\frac{1}{2}} - \frac{9}{8} (3\tau^2 + 1)^{\frac{1}{2}} + \frac{13}{8} (\tau^2 + 1)^{\frac{1}{2}} \end{array} \right\} \quad (3-37)$$

where

$$\tau = \frac{a}{b}$$

$$c_1 = \frac{54a^2 - 7b^2 + 18ab}{24ab} \quad (3-38)$$

$$c_2 = \frac{b^2 - 42a^2 - 18ab}{24ab}$$

The result of the surface integration over a y -directed current cell is obtained by interchanging $a \leftrightarrow b$ in equations (3-37) and (3-38). The details of completing the integration of equation (3-36) are given in Appendix B.

Using the result of equation (3-37), the asymptotic value of the Green's function can be obtained as follows:

- 1) Using tabulated data and linear interpolation, find the contribution to the Green's function from the integral of equation (3-35).
- 2) Using numerical integration, complete the surface integrations over the source cell for the product of the integrals of equation (3-35) and the rooftop basis function.
- 3) Add the contribution of equation (3-38), multiplied by the appropriate constant, to the result of step #2. The result is the integration of the product of the Green's function and the rooftop basis function over the source cell's surface.

3.4.2 Modeling the Microstrip Feedline. To complete the MoM solution as described in section 3.3, the expansion coefficients for the surface current J_{inc} must be known. Finding the coefficients requires completion of another MoM solution using the same basis and test functions as those of the antenna's solution. The exact excitation model would depend upon the means used to excite the microstrip feedline. One common excitation is the use of a coaxial probe, and several means to model this excitation have been described by various authors [5:613;19:431-436;20:428;21:229-231] with one especially detailed model developed by Hall and Mosig for microstrip antennas with electrically thick substrates [10:370-375]. For a general mircostrip feedline,

Kobayashi presents closed-form expressions for the normalized longitudinal and transverse feedline current distributions [20].

Since the excitation model can take on such wide variations, and the purpose of this research is to obtain a more general solution for the antenna, the MoM solution of section 3.3 will be changed to eliminate dependence upon the antenna excitation technique. The modified version of the MoM solution is explained in the following section.

3.5 The 3-Plane Model - A Solution Independent of the Excitation Source

To prevent the MoM solution from being dependent upon the excitation model, the antenna model can be generalized by assuming a distribution for the magnetic currents on the aperture. By making this assumption, the feedline's role in the solution is eliminated, and the solution now depends only upon the interactions of the aperture and patches.

3.5.1 *Approximations for the Aperture Fields.* As discussed by Pozar [26:50], the best coupling of energy from the aperture to the driven patch is obtained when the aperture is a long, thin rectangular slot. With the geometry of this analysis, the long, thin rectangular slot results in the y-dimension of the aperture being considerably larger than the x-dimension. Given this configuration, the electric fields for the aperture will be dominated by an x-directed component resulting in a y-directed equivalent magnetic current on the aperture.

Since the aperture is electrically small, it is reasonable to assume the electric field of the aperture can be represented by a single piecewise sinusoidal function [27:1443;27:978]

$$\underline{E}_1^b = \hat{x} E_{1x}^b - \hat{x} \frac{\sin \left[k_e \left(\frac{L}{2} - |y| \right) \right]}{W \sin \left(\frac{k_e L}{2} \right)} \quad (3-39)$$

where

W = the x -dimension of the aperture

L = the y -dimension of the aperture

k_e = the effective wavenumber of the piecewise sine

The effective wavenumber is best represented as the average of the wavenumbers in the regions adjacent to the aperture [26:1440;29:979].

Thus, the effective wavenumber of the piecewise mode is given by

$$k_e = k_0 \left(\frac{\epsilon_r^{1a} + \epsilon_r^{1b}}{2} \right)^{\frac{1}{2}} \quad (3-40)$$

where

k_0 = free space wavenumber

ϵ_r^{1a} = the relative permittivity of the dielectric between interfaces 1a and 2a of the antenna

ϵ_r^{1b} - the relative permittivity of the dielectric between interfaces 1b and 2b of the antenna

With this approximation for the aperture electric fields, the magnetic currents can be calculated as follows

$$\underline{M}_1^b = \hat{n} \times \underline{E}_1^b = \hat{z} \times \hat{x} E_{1x}^b = \hat{y} \frac{\sin \left[k_e \left(\frac{L}{2} - |y| \right) \right]}{W \sin \left(\frac{k_e L}{2} \right)} \quad (3-41)$$

By approximating the aperture magnetic currents in this manner, the solution of the antenna becomes a matter of satisfying the first two boundary conditions in Table 3-1.

3.5.2 Modified Matrix Equation. As discussed previously, on each patch the tangential electric fields are the sum of contributions from the magnetic current of the aperture, the surface currents on the patch itself, and the surface currents of the remaining patch. Since the magnetic currents of the aperture are now a known variable, the fields created by the magnetic currents become the forcing function in the field equations. Thus, the matrix equation satisfying the first two boundary conditions of Table 3-1 is

$$\begin{bmatrix} [Z_{ij}^{b22}] & [Z_{ij}^{b23}] \\ [Z_{ij}^{b32}] & [Z_{ij}^{b33}] \end{bmatrix} \begin{bmatrix} [\alpha_j^{b2}] \\ [\alpha_j^{b3}] \end{bmatrix} = \begin{bmatrix} \langle \underline{w}_i, \underline{E}_{21}^b \rangle \\ \langle \underline{w}_i, \underline{E}_{31}^b \rangle \end{bmatrix} \quad (3-42)$$

where all the elements on the left of the equation are the same as those previously specified in equations (3-27) and (3-31).

The inner-products comprising the elements of the column matrix to the right of the equals sign in equation (3-42) are given by

$$\begin{aligned} \langle \underline{w}_i, \underline{E}_i^{b21} \rangle &= \int_{C_{2i}} \underline{dl} \cdot \int_{Ap} \underline{G}_{E21}^b(R, \zeta) \cdot \underline{M}_i^b(\rho') ds' \\ \langle \underline{w}_i, \underline{E}_i^{b31} \rangle &= \int_{C_{3i}} \underline{dl} \cdot \int_{Ap} \underline{G}_{E31}^b(R, \zeta) \cdot \underline{M}_i^b(\rho') ds' \end{aligned} \quad (3-43)$$

Equation (3-42) is the method of moments matrix equation that will be solved in this thesis.

3.6 Solving the MoM Matrix Equation

The solution matrix of equation (3-34) and impedance matrix of equation (3-42) both have large dimensions. For example, consider an antenna with dimensions shown in Table 2. Using the charge cell dimension of $a = 0.05\lambda$ and choosing five y-directed charge cells across each plane of the antenna, the dimensions of the square solution matrix

of equation (3-34) would be 448, and with the 3-plane model, the square impedance matrix would have dimensions of 170. Solving the MoM matrix

Table 3-2 An Example Antenna with its Associated MoM Segmentation

Antenna Element	x-dimensions (wavelengths)	x-directed current cells	y-directed current cells
Feedline	1.5	145	120
Aperture	0.1	5	8
Lower Patch	0.5	45	40
Upper Patch	0.5	45	40

equation of the 3-plane model using Gaussian elimination to invert the impedance matrix is feasible [20:427]. However, for the larger matrix of the complete antenna model, an iterative solution scheme might prove to be more advantageous.

3.6.1 Solving the Matrix Equation via Iteration. As discussed by Moore and Pizar [17:270], iterative schemes offer economies of computer storage and processing time, as compared to Gaussian elimination or other factorization approaches, when the matrices in the MoM solution are very large. Since the square impedance matrices of the three or four plane MoM solution may have very large dimensions for certain geometries, development of an iterative scheme for solving the MoM matrix equation is worthwhile.

3.6.2 Basic Iterative Method. For the matrix equation $ZI = V$, the matrix Z may be decomposed such that

$$Z = Z_0 + Z_1 \quad (3-44)$$

where Z_0 is more easily inverted than Z . By substituting equation (3-44) into the original matrix equation, the equation may be rewritten

$$Z_0 \underline{I} = \underline{V} - Z_1 \underline{I} \quad (3-45)$$

Based on equation (3-44), an iterative process can be defined such that [16:272]

$$Z_0 \underline{I}^{(k+1)} = \underline{V} - Z_1 \underline{I}^{(k)} ; k = 0, 1, 2, \dots \quad (3-46)$$

Moore and Pizer discuss several iterative schemes based on a priori knowledge of various characteristics of the matrix system being solved. Earlier discussions of the MoM matrix equation and characteristics of the Z matrix have emphasized the fact that the MoM solution and impedance matrices are diagonally dominant, and one approach highlighted by Moore and Pizer is well suited to a system with this characteristic.

3.6.3 An Iterative Approach Suited to the MoM Solution. The iterative scheme best suited to the MoM solution of the complete antenna model was proposed by Ferguson et al. [9:230-235] and begins with the decomposition of Z such that

$$Z = L + B + U$$

(3-47)

where B is a banded matrix formed by elements on either side of the diagonal of Z . The matrices L and U are the lower and upper triangular matrices, respectively, left when the elements of B are replaced by zero in Z .

The key to this scheme, making it ideally suited to the solution of the aperture-fed, stacked patch antenna, is that the matrix B must contain the largest elements of Z in order for the system to converge. Since the Z matrix of the MoM solution is diagonally dominant, this condition will always be satisfied. Also, since the largest elements of the MoM matrix are already on the diagonal, no row pivoting is required during decomposition which results in the most efficient iterative solution scheme [9:230].

Using this representation for Z , the iterative scheme becomes

$$\underline{I}^{(k+1)} = B^{-1} [\underline{V} - (L + U) \underline{I}^{(k)}] \quad (3-48)$$

The iteration is repeated until a previously selected stopping criterion is satisfied. One criterion presented by Moore and Pizer [17:276] is based on the relative change in the norms of successive solutions. Denote the present iterated solution with a superscript $(k+1)$ and the last iteration with superscript (k) , and suppose the vector \underline{I} contains N elements. The first step in determining satisfac-

tion of the stopping criterion is to form the difference vector $\delta \underline{I}^{(k+1)}$ where

$$\delta \underline{I}^{(k+1)} = \underline{I}^{(k+1)} - \underline{I}^{(k)} \quad (3-49)$$

where the i th element of the vector $\delta \underline{I}^{(k+1)}$ is the difference between the i th element of $\underline{I}^{(k+1)}$ and $\underline{I}^{(k)}$. Next, the norm of $\delta \underline{I}^{(k+1)}$ is calculated

$$|\delta \underline{I}^{(k+1)}|^2 = \sum_{i=1}^N \delta \underline{I}_i^{(k+1)} \delta \underline{I}_i^{(k+1)*} \quad (3-50)$$

where the * indicates complex conjugate. Similarly, the norm of $\underline{I}^{(k)}$ is found. The stopping criterion is satisfied when

$$|\delta \underline{I}^{(k)}| < \epsilon |\underline{I}^{(k+1)}| \quad (3-51)$$

where ϵ is selected based on the required accuracy of the solution.

Ferguson *et al.* report processor time saving of 5 to 10 times, and up to 23 times, relative to Gaussian elimination. However, this particular scheme does not allow any computer memory savings unless some algorithm for disc storage of the matrices in the scheme is employed.

3.7 Calculating the Fields of the Antenna

While the calculations of the fields on the antenna interfaces will not be a part of this effort, the software developed to complete the MoM solution can be used to do so. This section outlines how the fields on the antenna interface and the far-field patterns can be calculated using the results of the MoM solution.

3.7.1 Calculating the fields on the Antenna Interfaces. After the surface current and charge density coefficients are known, all the sources on the antenna are defined, and the fields at any location on either of the three interfaces of the 3-plane antenna model can be calculated using many of the same Green's function data as used in the MoM solution. The only additional data needed is the analytic expression for the divergence of the surface charge Green's functions so that the surface charge field contributions of equations (3-6) and (3-7) can be calculated.

Once the divergence of the surface charge Green's functions is known, the subroutines of the MoM software can be used to complete the integrations needed to find the fields at any point on the antenna's interfaces.

One reason to calculate the fields on the interfaces is that doing so would provide a means to validate the MoM solution. If the solution is correct, the fields at any location on either of the two patches should be approximately equal to zero. Another reason to calculate the fields would be to calculate the radiation patterns of the antenna. One

approach to finding the antenna patterns is presented in the following section.

3.7.2 *Calculating the Antenna Far-Field Patterns.* As mentioned in Section 1.1, radiation from microstrip antennas is produced by the fringing fields along the edges of the microstrip patch. In the aperture-fed, stacked patch microstrip antenna the fringing fields of the patch on interface 3b produce the radiation. One approach to finding the antenna field patterns is to model the fringing fields of the patch with equivalent radiating apertures. The far-field patterns of the antenna can then be calculated using theory for radiating apertures.

3.7.2.1 *An Aperture Model for the Antenna.* Hammer *et al.* have shown the validity of using an aperture model to calculate the radiated fields of a microstrip antennas [12]. The first step of the modelling is the construction of four apertures along the edges of the antenna's radiating element. Next, the tangential fields on the interface of the radiating patch are calculated, and an equivalent electric field distribution is found such that the following relationship is satisfied:

$$\int_0^a |E_t| \cdot dl = E_a \cdot 2a \quad (3-52)$$

where

E_t - the tangential electric field value

E_a - the equivalent field distribution value

2a - the width of the radiation aperture

Actually, the value of E_t decreases to zero at a finite distance from the patch edge, and the upper limit of the integral in equation (3-52) can be replaced with a distance L where, in general, L is much less than the value of the free-space wavelength [12:267].

In [12], a closed-resonator model is used to approximate the tangential field magnitude. In this analysis, the Green's functions and the electric and magnetic surface currents permit the calculation of the tangential fields. Once the tangential fields have been calculated, the actual x-component and y-component of the fields can be replaced with an equivalent distribution such that the relation of equation (3-52) is satisfied for the x-directed and y-directed fields. This procedure produces an aperture model for the antenna as illustrated in Figure 3-4. Since the radiating apertures of the antenna model have constant, uniform field distributions, the far-field patterns are readily calculated.

3.7.2.2 Far-Field Pattern Equations. The far-field pattern is the sum of the pattern produced by the radiation of each aperture. To begin, consider aperture 1 of Figure 3-4 with equivalent tangential fields represented by the following expression:

$$\underline{E}_{t1} = E_{x1}\hat{x} + E_{y1}\hat{y} \quad (3-53)$$

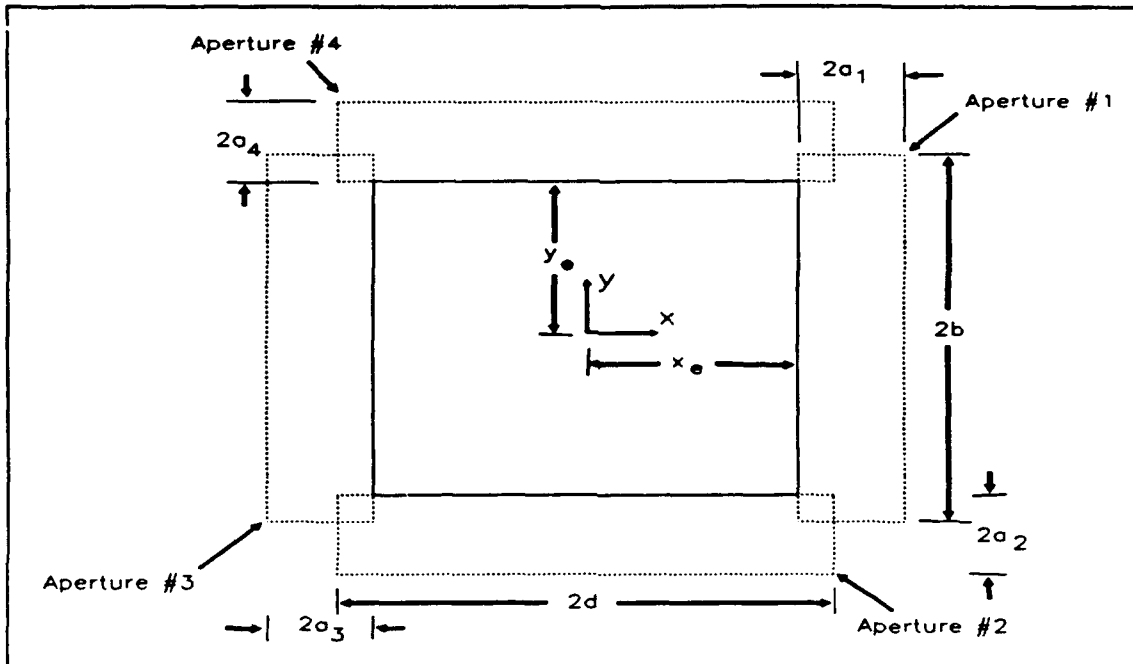


Figure 3-4 Aperture Model for Calculating Far-Field Radiation Patterns

The equivalent field principle can be used to obtain an expression for the magnetic surface currents of the aperture [2:460]:

$$\underline{M}_{a1} = -2\hat{n} \times \underline{E}_{t1} = 2E_{y1}\hat{x} - 2E_{x1}\hat{y} \quad (3-54)$$

Since the magnetic surface current can be expressed in terms of the components of the tangential fields, the components of the far-field pattern of the aperture can be found using the relationships [2:455-458]

$$E_{\theta 1} = [-E_{y1} \sin\varphi - E_{x1} \cos\varphi] \int_{S'} e^{j k_0 r' \cos\theta} ds' \quad (3-55)$$

$$E_{\varphi 1} = [E_{y1} \cos\theta \cos\varphi - E_{x1} \cos\theta \sin\varphi] \int_{S'} e^{j k_0 r' \cos\varphi} ds'$$

where

S' = the aperture surface

$$\psi = x' \cos\theta \cos\varphi + y' \cos\theta \sin\varphi$$

and the constants in the expression have been neglected since only the field pattern equations are desired.

IV. Method of Moments Software Description

This chapter presents the details of the FORTRAN software developed to complete the MoM solution for the 3-plane model of the aperture-fed, stacked patch microstrip antenna. The chapter begins by deriving the numerical integration equations needed to perform the various integrations of the MoM solution. Next, the algorithms and logic of the subroutines of the MoM solution software are described.

4.1 Numerical Integration Equations

The major task of completing the MoM solution for the antenna is performing the integrations needed to evaluate the elements of the MoM matrix equation. In the interest of accuracy and economy, Gaussian quadrature is used to complete all of these integrations.

To begin, the number of integration nodes to be used in the Gaussian quadrature must be determined. The selection of the number of nodes is based on the numerical behavior of the integrand within the interval of integration. If the integrand is oscillatory within the

interval, a larger number of nodes is required to accurately evaluate the integral. Therefore, the numerical stability of the integrands of the matrix elements must be investigated before a selection of the number of nodes is made.

Since the integrands are products of a Green's function and either a linear rooftop function or the constant Π function, the numerical characteristics of the Green's function will dominate the integrand's behavior. For the surface and line integrals in the MoM solution, the arguments of the Green's functions are rather small. Based on data presented by Nazar [23:74-84], under these conditions the real and imaginary parts of the Green's functions are well behaved. Therefore a relatively small number of quadrature nodes should suffice. To simplify software development and use, the same number of quadrature nodes will be used for all integrations. For the remainder of this discussion, five node quadrature will be assumed.

To derive the numerical integration equations, the integrations for the impedance sub-matrix describing the fields on interface 2b produced by the surface currents and charge density of interface 3b will be considered:

$$[Z_{ij}^{b23}] = \sum_{i=1}^{N_2} \sum_{j=1}^{N_3} \left\{ \begin{array}{l} \frac{j\omega}{\epsilon_{3j}} \int_{C_{21}} \cdot \frac{dl}{ds_{3j}} \int_{S_{3j}} G_{A23}^b(R_{ij}) dl \cdot T(\gamma_{3j}) ds' \\ + \frac{1}{j\omega a_3 b_3} \int_{S_{3j}} [G_{q23}^b(R_{ij}) - G_{q23}^b(R_{ij}^-)] \Pi(\gamma_{3j}) ds' \end{array} \right\} \quad (4-1)$$

This expression is typical of the expressions defining the remaining sub-matrices of the MoM impedance matrix and the numerical integration equations for this sub-matrix can easily be adapted for those sub-matrices.

To begin, the dot product operations in equations (4-1) must be completed. First, the dot product of the dyadic Green's function and the rooftop basis functions in the source surface integration will be simplified. Recall for $1 \leq j \leq N_{3x}$, the rooftop vector functions are x-directed, and for $N_{3x} < j \leq N_3$, the rooftop vector functions are y-directed. Therefore, the dot product between the dyadic Green's function and the rooftop vector functions produces the following vectors:

$$\underline{G}(R_{ij}) \cdot \underline{T}(\gamma_{3j}) = \begin{cases} [\hat{x}G_{A23}^{bxx}(R_{ij}) + \hat{y}G_{A23}^{byx}(R_{ij})]T_x(\gamma_{3j}) ; 1 \leq j \leq N_{3x} \\ [\hat{x}G_{A23}^{bxy}(R_{ij}) + \hat{y}G_{A23}^{byy}(R_{ij})]T_y(\gamma_{3j}) ; N_{3x} < j \leq N_3 \end{cases} \quad (4-2)$$

Next, consider the line integration along the observer current cell's test segment dotted with the surface integration over the source current cell surface. The test segments are x-directed for $1 \leq i \leq N_{2x}$ and y-directed for $N_{2x} < i \leq N_2$. The dot product of the line and surface integrals is then

$$\begin{aligned}
& \int_{C_{21}} \frac{dl}{ds} \cdot \int_{S_{3j}} G_{A23}^b(R_{ij}) \cdot T(\gamma_{3j}) ds' \\
& - \left\{ \begin{array}{l} \left\{ \begin{array}{l} \int_{C_{2xi}} dx \int_{S_{3xj}} G_{A23}^{bxz}(R_{ij}) T_x(\gamma_{3j}) ds' ; 1 \leq i \leq N_{2x} \\ \int_{C_{2yi}} dy \int_{S_{3xj}} G_{A23}^{byz}(R_{ij}) T_x(\gamma_{3j}) ds' ; N_{2x} < i \leq N_2 \end{array} \right\} 1 \leq j \leq N_{3x} \\ \left\{ \begin{array}{l} \int_{C_{2xi}} dx \int_{S_{3yj}} G_{A23}^{bxy}(R_{ij}) T_y(\gamma_{3j}) ds' ; 1 \leq i \leq N_{2x} \\ \int_{C_{2yi}} dy \int_{S_{3yj}} G_{A23}^{bzy}(R_{ij}) T_y(\gamma_{3j}) ds' ; N_{2x} < i \leq N_2 \end{array} \right\} N_{3x} < j \leq N_3 \end{array} \right. \quad (4-3)
\end{aligned}$$

4.1.1 *Impedance Sub-Matrix Gaussian Quadrature Equations.* Using five-node Gaussian quadrature, and integration over the interval $x \in [-1,1]$ can be approximated by the summation

$$\int_{-1}^1 f(x) dx \approx \sum_{n=1}^5 w_n f(x_n) \quad (4-4)$$

where

w_n = the weight assigned to the n th Gaussian quadrature node in the interval $[-1,1]$

x_n = the location of the n th Gaussian quadrature node in the interval $[-1,1]$

To complete the triple integrations of equation (4-1), the single variable quadrature is extended to incorporate three variables. Then,

for example, the triple integrations of equation (4-4) for the index ranges $1 \leq j \leq N_{3x}$ and $1 \leq i \leq N_{2x}$ can be approximated by the triple summation

$$\begin{aligned} & \int_{C_{2xi}} dx \int_{S_{3xj}} G_{A23}^{bxz}(R_{ij}) T_z(\gamma_j) ds' \\ & \approx \sum_{l=1}^5 \sum_{m=1}^5 \sum_{n=1}^5 w_l w_m w_n G_{A23}^{bxz}(\rho_{il}, \rho'_{jm}) T_z(\gamma_{jmn}) \end{aligned} \quad (4-5)$$

where

w_l, w_m, w_n = the Gaussian quadrature weights as determined by the value of their subscript variables

l = the quadrature node index for the observer current cell's test segment

m, n = the quadrature node indices for the source current cell's x-coordinate and y coordinate, respectively

The position vectors ρ_{il} and ρ'_{jm} in equation (4-5) now require clarification. Since the Gaussian quadrature nodes and weights are generally available for the interval $[-1, 1]$, a coordinate transformation must be made with regard to the integration variables of equation (4-5). The appropriate transformation is given by [4:2-83]

$$\int_{\lambda_1}^{\lambda_2} f(t) dt = \frac{\lambda_2 - \lambda_1}{2} \int_{-1}^1 f \left[\frac{\lambda_2 + \lambda_1 + x_n(\lambda_2 - \lambda_1)}{2} \right] dx \quad (4-6)$$

On the x-directed observer current cells, the line integration along the cell's test segments means $\lambda_1 = x_i - a_2/2$ and $\lambda_2 = x_i + a_2/2$. Then, according to equation (4-6), the scale factor of the coordinate transformation is $a_2/2$, and the position vector ρ_{i1} is

$$\rho_{i1} = \hat{x} \left[x_i + \frac{x_i a_2}{2} \right] + \hat{y} y_i ; 1 \leq i \leq N_{2x} \quad (4-7)$$

where

x_i = the i th Gaussian quadrature node in the interval $[-1,1]$

x_i and y_i = the x- and y-coordinates of the position vector ρ_{xi}

Along a y-directed observer test segment, $\lambda_1 = y_i - b_2/2$ and $\lambda_2 = y_i + b_2/2$. The coordinate transformation generates a scale factor of $b_2/2$, and the position vector ρ_{i1} is

$$\rho_{i1} = \hat{x} x_i + \hat{y} \left[y_i + \frac{y_i b_2}{2} \right] ; N_{2x} < i \leq N_2 \quad (4-8)$$

where

y_i = the i th Gaussian quadrature node in the interval $[-1,1]$

x_i and y_i = the x- and y-coordinates of the position vector ρ_{yi}

The surface integrations require transformations in both the x- and y-coordinates. Over an x-directed current cell of interface 3b, the

intervals for the surface integrations are $x \in [x_j - a_3, x_j + a_3]$ and $y \in [y_j - b_3/2, y_j + b_3/2]$. Thus, the coordinate transformation scale factor is $a_3 b_3/2$, and the position vector ρ'_{jmn} is

$$\rho'_{jmn} = \hat{x}(x_j + x_m a_3) + \hat{y}\left(y_j + \frac{y_m b_3}{2}\right); 1 \leq j \leq N_{3x} \quad (4-9)$$

where

x_m = the m th quadrature node location in the interval $[-1,1]$

y_n = the n th quadrature node location in the interval $[-1,1]$

Over the surface of a y -directed cell $x \in [x_j - a_3/2, x_j + a_3/2]$ and $y \in [y_j - b_3, y_j + b_3]$. The scale factor is again $a_3 b_3/2$, and ρ'_{jmn} is given by

$$\rho'_{jmn} = \hat{x}\left(x_j + \frac{x_m a_3}{2}\right) + \hat{y}(y_j + y_m b_3); N_{3x} < j \leq N_3 \quad (4-10)$$

With these definitions for the position vectors, the variable γ_{jmn} becomes

$$\gamma_{jmn} = \begin{cases} \hat{x} \cdot (\rho'_{jmn} - \rho'_j) ; 1 \leq j \leq N_{3x} \\ \hat{y} \cdot (\rho'_{jmn} - \rho'_j) ; N_{3x} < j \leq N_3 \end{cases} \quad (4-11)$$

Substituting the appropriate coordinate transformation scale factors and summation approximations for the integrations of (4-1), the numerical integration equations for the impedance sub-matrix becomes

$$[Z_{ij}^{b23}] \approx \sum_{i=1}^{N_2} \sum_{k=1}^{N_3} \left\{ \begin{array}{l} \left[\sum_{l=1}^5 \sum_{m=1}^5 \sum_{n=1}^5 w_{lmn} \left\{ \begin{array}{l} \frac{j\omega a_2 a_3}{4} GT_{A23}^{bxx} ; 1 \leq i \leq N_{2x} \\ \frac{j\omega b_2 a_3}{4} GT_{A23}^{byx} ; N_{2x} < i \leq N_2 \end{array} \right\} \right]_{1 \leq k \leq N_{3x}} \\ + \frac{1}{j2\omega} \sum_{m=1}^5 \sum_{n=1}^5 w_{mn} GP_{q23}^x \end{array} \right\} \\ \left\{ \begin{array}{l} \left[\sum_{l=1}^5 \sum_{m=1}^5 \sum_{n=1}^5 w_{lmn} \left\{ \begin{array}{l} \frac{j\omega a_2 b_3}{4} GT_{A23}^{bxy} ; 1 \leq i \leq N_{2x} \\ \frac{j\omega b_2 b_3}{4} GT_{A23}^{byy} ; N_{2x} < i \leq N_2 \end{array} \right\} \right]_{N_{3x} \leq k \leq N_{3x}} \\ + \frac{1}{j2\omega} \sum_{m=1}^5 \sum_{n=1}^5 w_{mn} GP_{q23}^{y+} \end{array} \right\} \end{array} \right\} \quad (4-12)$$

where the summation index j of equations (3-24), (3-27), (3-29), and (3-31) has been replaced with the index k to prevent confusion with the use of j to indicate the $\sqrt{-1}$. The other variables of equation (4-12) are defined as follows:

$$w_{lmn} = w_l w_m w_n$$

$$w_{mn} = w_m w_n$$

$$GT_{A23}^{bxx} = G_{A23}^{bxx}(\rho_{il}, \rho'_{jmn}) T_x(\gamma_{jmn})$$

$$GT_{A23}^{byx} = G_{A23}^{byx}(\rho_{il}, \rho'_{jmn}) T_x(\gamma_{jmn})$$

$$GT_{A23}^{bxy} = G_{A23}^{bxy}(\rho_{il}, \rho'_{jmn}) T_y(\gamma_{jmn})$$

$$GT_{A23}^{byy} = G_{A23}^{byy}(\rho_{il}, \rho'_{jmn}) T_y(\gamma_{jmn})$$

$$GP_{q23}^x = [G_{q23}^b(\rho_{xi}^+, \rho'_{jmn}) - G_{q23}^b(\rho_{xi}^-, \rho'_{jmn})] \Pi_x(\gamma_{jmn})$$

$$GP_{q23}^y = [G_{q23}^b(\rho_{yi}^+, \rho'_{jmn}) - G_{q23}^b(\rho_{yi}^-, \rho'_{jmn})] \Pi_y(\gamma_{jmn})$$

(4-13)

4.1.2 *Inner-Product Gaussian Quadrature Equations.* The elements of the forcing function in the 3-plane MoM matrix equation are defined in equation (3-43). As with the impedance sub-matrix, the first step in obtaining the Gaussian quadrature equations for the inner-products is understanding the significance of the dot product between the dyadic Green's function and the magnetic surface current vector of the aperture. From equation (3-39), the magnetic surface current vector is y-directed, therefore the dot-product of the general dyadic Green's function \underline{G}_E^b and the magnetic surface current vector is

$$\underline{G}_E^b \cdot \underline{M}_1^b = \hat{x} G_E^{bxy} M_y + \hat{y} G_E^{byy} M_y \quad (4-14)$$

On the x-directed current cells, the test functions, $w_i(x)$, are x-directed, and over the y-directed current cells they are y-directed.

Thus, the dot product between the line and surface integrals of equation (3-43) produces the following:

$$\langle \underline{w}_i, \underline{E}_i^b \rangle = \begin{cases} \int_{C_{xi}} dx \int_{S_{1b}} G_E^{bxy}(\rho_i, \rho') M_y(y') ds' ; 1 \leq i \leq N_x \\ \int_{C_{yi}} dy \int_{S_{1b}} G_E^{byy}(\rho_i, \rho') M_y(y') ds' ; N_x < i \leq N \end{cases} \quad (4-15)$$

As with the impedance elements, Gaussian quadrature is used to numerically evaluate the integrations of equation (4-15) using the same summation index assignments as for equations (3-24), (3-27), (3-29) and (3-31). On the observer current cells, the paths C_{xi} and C_{yi} are such that $x \in [x_i - a/2, x_i + a/2]$ and $y \in [y_i - b/2, y_i + b/2]$, respectively. Therefore, the coordinate transformation into the interval $[-1, 1]$ produces the scale factor $a/2$ on the x-directed current cells and $b/2$ on the y-directed current cells. The position vector ρ_{il} is the same as defined in equations (4-7) and (4-8).

Since the center of the aperture is defined as the origin of the antenna's coordinate system, the antenna's aperture surface is defined by $x \in [-W/2, W/2]$ and $y \in [-L/2, L/2]$. With the required coordinate transformation, a scale factor of $WL/4$ is obtained, and the source position vector is defined

$$\rho'_{mn} = \hat{x} \left(\frac{x_n W}{2} \right) + \hat{y} \left(\frac{y_m L}{2} \right) \quad (4-16)$$

where

x_n and y_m - the m th and n th Gaussian quadrature nodes in the interval $[-1,1]$

Using these definitions, the numerical approximations for the inner-products of equation (3-42) are

$$\begin{aligned} \langle w_i, E_{i21}^b \rangle &\approx \sum_{l=1}^5 \sum_{m=1}^5 \sum_{n=1}^5 w_{lmn} \begin{cases} \frac{a_2 WL}{8} G_{E21}^{bxy}(\rho_{i1}, \rho'_{mn}) M_y(y') ; 1 \leq i \leq N_{2x} \\ \frac{b_2 WL}{8} G_{E21}^{byy}(\rho_{i1}, \rho'_{mn}) M_y(y') ; N_{2x} \leq i \leq N_2 \end{cases} \\ \langle w_i, E_{i31}^b \rangle &\approx \sum_{l=1}^5 \sum_{m=1}^5 \sum_{n=1}^5 w_{lmn} \begin{cases} \frac{a_3 WL}{8} G_{E31}^{bxy}(\rho_{i1}, \rho'_{mn}) M_y(y') ; 1 \leq i \leq N_{3x} \\ \frac{b_3 WL}{8} G_{E31}^{byy}(\rho_{i1}, \rho'_{mn}) M_y(y') ; N_{3x} \leq i \leq N_3 \end{cases} \end{aligned} \quad (4-17)$$

4.2 Software Overview

The MoM solution software is designed around evaluating the summations of equations (4-12) and (4-17). The operations of equation (4-17) are very similar to those of equation (4-12), therefore identifying the requirements for evaluating equation (4-12) will also serve to identify those for equation (4-17).

Equation (4-12) must be evaluated to form each of the four impedance sub-matrices that form the MoM impedance matrix. Calculating the elements of each impedance sub-matrix requires the following steps:

- (1) Establish the index of the observer current cell, this is the value of summation index i of equation (4-12) and the row index for the element's location within the impedance sub-matrix.
- (2) For each observer index, complete the triple summation over indices l , m , and n of (4-12) for each current cell on the source plane. The source current cell is determined by summation index j of equation (4-12). The index j also determines the column index of the element's location within the impedance sub-matrix.

Completing the triple summation over indices l , m , and n in equation (4-12) requires the following steps:

- (1) Establish the value of index l which controls the progression over the quadrature nodes of the observer current cell test segment.
- (2) For each node on the test segment, complete the summation over indices m and n . For each of the possible combinations of indices l , m , and n , $|\rho_{ii} - \rho'_{jmn}|$ must be calculated according to equations (4-7) or (4-8) and (4-9) or (4-10) and the surface

current or surface charge density basis function must be calculated. Based on the value of $|\rho_{11} - \rho'_{jmn}|$, the appropriate Green's function must be evaluated using the polynomial model.

The difference between completing the operations of equation (4-17) and (4-12) is that for equation (4-17) the source plane is now the complete aperture, and the piecewise sinusoidal magnetic current distribution function is used instead of the rooftop basis function.

Completing the antenna solution involves three basic functions. First, antenna parameters - operating frequency, dielectric permitivities and permeabilities, element dimensions - and the Green's functions' polynomial coefficients must be read from data files. Next, data for calculating the integration node position vectors must be calculated. The MoM matrix elements are then calculated and the MoM matrix equation is solved to obtain the expansion coefficients for the surface currents and surface charge densities. Finally, the surface currents are calculated using the expansion coefficients.

The MoM software consists of a main program and 13 subroutines. The function of the main program is to call subroutines in the appropriate order and set operation flags and variables for the subroutines. Since the main program does not complete any major portion of the solution, it will not be described in detail. Instead, any inputs to subroutines provided by the main program will be described as each subroutine is described. The following sections detail the subroutines that were developed to complete the three basic functions needed to

complete the MoM solution. Complete listings of the MoM software are contained in the Computer Program Supplement for this thesis.

4.3 Antenna Data Subroutines

Three subroutines are used to either read data for the solution or calculate data needed in the solution. These subroutines are the first executed by the main program.

4.3.1 Subroutine INPUT. The data input is accomplished by subroutine INPUT. Subroutine INPUT is used to read data from two separate data files and then perform several short calculations with the data. The first data file accessed is file GEO.DAT. This file contains seven lines of antenna data. The expected entries and read formats for the data file are as follows:

Line 1) The relative permeabilities of the dielectric substrates between interfaces 1b and 2b, named MUR1B, between interfaces 2b and 3b, named MUR2B, and above interface 3b, named MUR3B. All values on the same line in the same order. The read format for these values is five columns with three decimal places.

Line 2) The relative permittivities of the dielectric substrates between interfaces 1a and 2a, named EPSR1A, between interfaces 1b and 2b, named EPSR1B, between interfaces

2b and 3b, named EPSR2B, and above interface 3b, named EPSR3B. All values on the same line with the value for EPSR1A first. The read format for these values is five columns with three decimal places. The variables EPSR1A and EPRSR1B are then used to calculate the effective wavenumber, variable KE, for the aperture's magnetic field approximation.

Line 3) The operating frequency of the antenna in GHz. The read format for the frequency is five columns with two decimal places, thus limiting the maximum operating frequency to 99.99 GHz. However, the read format can be changed to accommodate any higher frequencies, there are not any software features that would prevent raising the maximum possible frequency. The frequency is converted to radians/second and assigned the variable name OMEGA.

Line 4) The number of integration nodes to be used for all line and surface integrations. The value is read using a one column integer format and is assigned the variable name NUMNODES. The software is written for four or six node Gaussian quadrature.

Lines 5-7) These lines contain the geometry data of the antenna. Line 5 contains data for the aperture, Line 6

contains data for the patch of interface 2b, and Line 7 contains data for the patch of interface 3b. Each line contains the x-dimension of the aperture or patch, the y-dimension of the aperture or patch, the height of the interface above the aperture, and then the x- and y-distances between the patch's center relative to the aperture's center. The origin of the antenna is set at the aperture center, so the height and offset entries on Line 4 will all be zero. All dimension entries in the data file are in units of centimeters. After the dimension data is read, it is converted to units of meters and placed in the one-dimensional arrays XDIMEN, YDIMEN, ZPLANE, XOFFSET, and YOFFSET. The array indices of these arrays designate to which element of the antenna the dimension applies, with one corresponding to the aperture, two corresponding to the patch on interface 2b, and three corresponding to the patch on interface 3b. All dimensional data is read with a format of six columns and three decimal places.

The second data file accessed is file GREENFS.DAT. This file contains the data for the polynomial representations of the antenna's Green's functions. The coefficients are stored in 3 three-dimensional arrays - GBA, IB, and GBQ. The details of the polynomial models for the various Green's functions are given in Appendix A.

Array GBA contains the polynomial coefficients for the three Green's functions that have subscripts Ast , where s and $t \in [2,3]$. The first index of an element in array GBA designates which Green's function the coefficients belong to - 1 \leftrightarrow G_{A22} , 2 \leftrightarrow G_{A33} , and 3 \leftrightarrow G_{A23} or G_{A32} . For the $A22$ Green's functions, the function with superscript bxx equals the function with superscript byy , and the functions with superscript bxy and byx are zero. Thus, the coefficients in array GBA with a first index equal to one represents all non-zero Green's functions with subscript $A22$. Similarly, the Green's functions subscripted $A33$ have the bxx function equal to byy , with byx and bxy equal to zero. The third row of array GBA contains the coefficients of the Green's G_{A23} or G_{A32} . For these Green's functions, the functions with superscript bxx are equal to those with superscript byy , and the functions with superscript bxy or byx are zero. Additionally, the Green's functions with subscript $A23$ are equal to those with subscript $A32$.

The Green's functions that have a superscript of $E21$ or $E31$ are defined by two or more Sommerfeld integrals, and array IB contains the coefficients for the polynomials representing these integrals. The first index of array IB determines which of the six integral parts the coefficients represent. Array elements with a first index of 1, 3, and 5 correspond to $E21$ Green's function, and the elements with a first index of 2, 4, and 6 correspond to the $E31$ Green's function.

Array GBQ contains coefficients for the Green's functions needed to calculate the electric fields created by the surface charge density.

The first index of the array corresponds to the subscript of the Green's function - 1 = q22, 2 = q33, 3 = q23, and 4 = q32.

The polynomial models for the G_A and G_E Green's functions all have the same form - real component represented by a polynomial whose form is determined by the value of R, and an imaginary component represented by the same polynomial over all values of R. For these functions, a second index equal to 1 indicates coefficients for the polynomial modelling the real component for $R < .01$, and a second index equal to 2 indicates coefficients for the polynomial modelling the real component when $R > 0.01$. The elements with a second coefficient equal to 3 contain the coefficients for the polynomial modelling the imaginary component of the Green's functions. The third dimension of the array elements in arrays GBA and IB indicates the coefficient subscript as detailed in Appendix A. The value of the third index is equal to the coefficient subscript plus one.

The G_q Green's functions are modeled with one polynomial which is valid over all values of R representing the real component, and different polynomials valid over two different intervals of R representing the imaginary component. The second index of array GBQ has the same function as the second index of arrays GBA and IB, except an index value of one designates the polynomial for the real component, a second index of two designates the polynomial data for the interval $R < 0.01$, and an index of 3 indicates data for the interval $R > 0.01$.

The coefficients are all real values and are first read into array GBA, then IB, and GBQ. Each Green's function has a polynomial model for

its real component or imaginary component valid only for specific ranges of R, and the first line defines these ranges. The next 63 lines contain the data for arrays GBA and IB. The data is arranged such that the coefficients of the polynomial of the function's real component for $R < 0.01$ are on the first two lines; five then four coefficients per line. Next come the coefficients for the $R > 0.01$ real component polynomial; two lines with five coefficients per line then a single coefficient. Finally, the coefficients for the imaginary component are on lines six and seven; five then two coefficients per line.

The last 28 lines of the GREENFS.DAT file contain the coefficients for the G_q Green's functions; seven lines per Green's function. The first two lines contain the coefficients for the real component's polynomial; five then two coefficients per line. Lines three and four contain the coefficients for the interval $R < 0.01$ polynomial of the imaginary component; five then four coefficients per line. Lines five through seven contain the coefficients of the imaginary component's polynomials for $R > 0.01$; with five coefficients per line on lines five and six and one coefficient on line seven. The coefficients are read using the format 1PE16.7.

4.3.1 Subroutine SEGMENT. The first data calculation subroutine is named SEGMENT. This subroutine calculates the data needed to determine the value of R for the surface and line integration nodes on all planes.

As discussed in the details of the MoM solution, each of the patches are divided into N_x x-directed current cells and N_y y-directed

current cells. Each charge cell has an x-dimension of a and a y-dimension of b . Following Mosig's work [17:320], the position vector data is calculated using $a = 0.05\lambda$ and b such that there are five y-directed current cells for each patch. To calculate the value of a , the subroutine assumes the x-dimension of the patch on interface 3b is approximately $\lambda/2$, thus a is equal to one-tenth of the patch's x-dimension. Using the a value for interface 3b, the patch on interface 2b is divided so that its a value is less than or equal to that of interface 2b. Having established the dimensions of the charge cells, the current cell dimensions are known, and position vector data can be found.

To calculate and store the position vector data, each patch's current cells are modeled as two-dimensional arrays. For example, Figure 4-1 illustrates the case of five x-directed charge cells and five y-directed charge cells across the patch. In this case, a 4x5 array of x-directed current cells and a 5x5 array of y-directed current cells is obtained. The first x-directed current cell, in the upper left corner of the patch, corresponds to element (1,1) of the current cell array and the twentieth x-directed current cell, in the lower right corner, corresponds to element (4,5).

Since the current cell position vector locates the cell's center, all current cells in the same column of the array have equal x-components in their position vectors, and all current cells in the same row of the array have equal y-components. With the origin at the lower left of the patch, the x- and y-components of the position vector for any current cell are

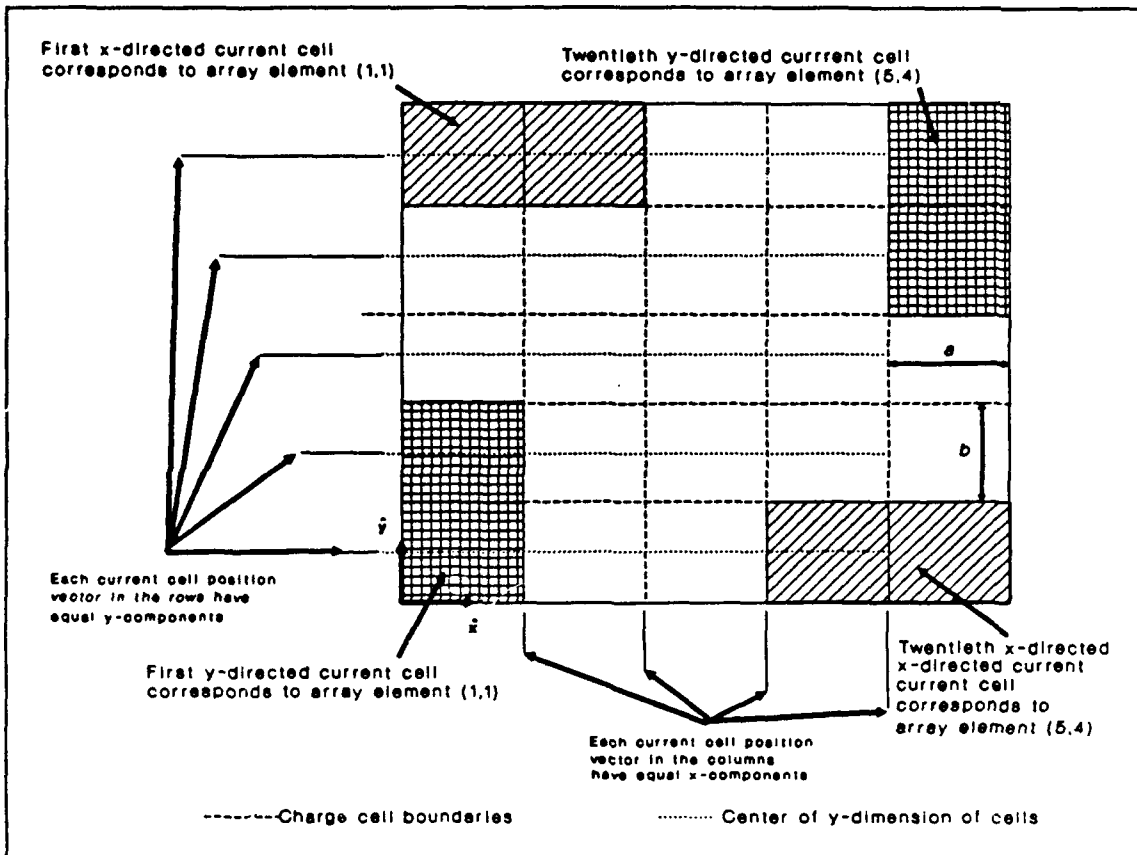


Figure 4-1 Array Representation of Current Cells on the Antenna Patch-es.

$$x_{rc} = c a \quad (4-18)$$

$$y_{rc} = W - \left[\frac{rb}{2} \right]$$

where

r = the array row index of the current cell

c = the array column index of the current cell

W = the y-dimension of the patch

On the patch of Figure 4-1, the y-directed current cells form a 4x5 array, with the first y-directed current cell corresponding to element (1,1) being located in the lower, left corner of the patch. The elements in the y-directed current cell array are numbered such that a larger column index indicates an increase in the y-direction, and a larger row index indicates an increase in the x-direction. With this convention, the twentieth y-directed current cell, corresponding to array element (4,5), is located in the upper right corner of the patch. In this instance, the position vectors of the current cells in the same array row will have equal x-components, and the position vectors of current cells in the same column will have equal y-components. The position vector components for the y-directed current cells are given by

$$\begin{aligned} x_{rc} &= \frac{ra}{2} \\ y_{rc} &= cb \end{aligned} \tag{4-19}$$

To translate the origin from the lower left corner to the center of the patch, one half the x-dimension of the patch is subtracted from each x-component, and one half the y-dimension of the patch is subtracted from the y-component. To compensate for the possible offset between the patch and aperture centers, the patch's center offset values are added to the appropriate coordinates.

Using this array model, subroutine SEGMENT calculates the position vector x- and y-components for the rows and columns of current cells

storing them in 4 two-dimensional arrays. The data arrays XXCOORD and XYCOORD contain the position vector components for the columns and rows, respectively, of x-directed current cells on the patch, and data arrays YXCOORD and YYCOORD contain the same information for the rows and columns of the y-directed cells. The first index of these data arrays designates the array row or column in which the cell is located, and the second index identifies on which plane the cell is located.

The surface integration node position vector components are calculated using similar array models, except the array is contained within an x-directed or y-directed current cell. The node array is square, with dimensions being equal to the number of Gaussian quadrature nodes, variable NUMNODES. The nodes are arranged in the array such that element (1,1) corresponds to the node with the most negative x-coordinate and most positive y-coordinate, and element (NUMNODES,NUMNODES) is the node with the most positive x-coordinate and the most negative y-coordinate. With the origin located at the current cell's center, on x-directed current cells the coordinates for the integration node array rows and columns are

$$\begin{aligned}x_{mn} &= x_n a \\y_{mn} &= \frac{-y_m b}{2}\end{aligned}\tag{4-20}$$

where

m and n = the summation indices as used in equations (4-12) and (4-17), m corresponds to the node array's row index, n corresponds to the node array's column index

x_n = the value of the n th integration node on $x \in [-1,1]$

y_m = the value of the m th integration node on $y \in [-1,1]$

For y-directed current cells, the coordinates of the integration node array rows and columns are

$$\begin{aligned}x_{mn} &= \frac{x_n a}{2} \\y_{mn} &= -y_m b\end{aligned}\tag{4-21}$$

The position data of the surface integration nodes is stored in 4 two-dimensional arrays. For nodes on an x-directed current cell, the data array XCOL contains the x-coordinates for the node array columns, and the data array XROW contains the y-coordinates for the rows. In a y-directed current cell, the x-coordinates of the rows in the node array are contained in the data array YROW, and the y-coordinates of the node array columns are contained in data array YCOL. For all node coordinate data arrays, the first index designates the quadrature node with which the coordinate matches, and the second index designates on which plane the node is located.

The line integration nodes are modeled as a one-dimensional array along the test segment of the observer current cell. For an x-directed

current cell, the test segment is centered in the cell with respect to the y-direction, and the segment covers the interval $x \in [-a/2, a/2]$. Since the test segment is centered with respect to the y-direction, the y-coordinate for all nodes along the test segment is zero, and the x-coordinate is

$$x_1 = \frac{n_1 a}{2} \quad (4-22)$$

where

n_1 = the value of the lth integration node in the interval $[-1,1]$
 l = the summation index as used in (4-12) and (4-17)

On a y-directed current cell, the test segment is centered with respect to the x-direction, thus the x-coordinate of all nodes along the test segment is zero. Since the y-directed test segment covers the interval $y \in [-b/2, b/2]$, the y-coordinate of the nodes along the test segment are

$$y_1 = \frac{n_1 b}{2} \quad (4-23)$$

The line integration node coordinates are stored in 2 two-dimensional data arrays. The data array SEGX contains the node coordinates for the line integration nodes along the test segment of an x-directed

current cell, and SEGY contains the coordinates for the nodes along the test segment of a y-directed cells. The first index of the data array elements identifies with which node the coordinate belongs, and the second index identifies the plane on which plane the node is located.

Since the antenna aperture is not divided into charge and current cells, its position vector calculations are slightly different. Subroutine SEGMENT treats the aperture as a single x-directed current cell centered on the origin, thus the values of XXCOORD(1,1) and XYCOORD(1,1) are both zero. The coordinates of the aperture's integration nodes are

$$\begin{aligned}x'_{mn} &= \frac{x_n W}{2} \\y'_{mn} &= \frac{-y_m L}{2}\end{aligned}\tag{4-24}$$

The aperture surface integration node position vector components are stored in the data arrays XROW and XCOL using the same index assignment conventions as for the nodes on the antenna patches.

Since the aperture serves only as a source plane in the three plane solution, there is no need to calculate integration node position vector data for observer cell line integrations.

4.3.2 Subroutine ASYGFS. Subroutine ASYGFS evaluates the value of the 1/R term in the asymptotic form of the Green's functions G_{A22} , G_{A33} , G_{q22} , and G_{q33} which is given by equation (3-37). The subroutine first calculates the scaling factor for the surface current, array JFACT, or surface charge, array QFACT, Green's functions based on the

plane of interest, then the expression of (3-37) is evaluated. The total contribution of the $1/R$ term is calculated by multiplying the value of equation (3-37) by the appropriate scale function. The contribution of the $1/R$ term is stored in two, 2-dimensional arrays. Array JASYVAL contains the contribution for Green's functions G_{A22} and G_{A33} . The array QASYVAL contains the contribution to Green's functions G_{q22} and G_{q33} . For both arrays, the first index indicates to which plane the contribution belongs - 2 = interface 2b and 3 = interface 3b. The second index of the arrays indicates to which orientation of cell the contribution belongs - 1 = an x-directed current cell and 2 = a y-directed current cell.

4.4 Method of Moments Matrix Equation Subroutines

The MoM matrix equation is constructed and solved using the first level subroutines EVALSUB, EVALRHS and SOLVNRVS. Subroutine EVALSUB evaluates the elements of each impedance sub-matrix and places the elements in the proper locations of the MoM impedance matrix. The subroutine EVALRHS calculates the column matrix of inner products that form the forcing function of the MoM matrix equation. Subroutine SOLVNRVS is used to solve the MoM matrix equation via inversion of the impedance matrix. All these subroutines rely on second or third level subroutines to complete their task. The descriptions of these lower

level subroutines and their functions immediately follow the description of the higher level subroutine that uses them.

4.4.1 Subroutine EVALSUB. As mentioned above, EVALSUB evaluates the impedance sub-matrices of the MoM impedance matrix. Subroutine EVALSUB only calculates the impedance matrix for the observer/source plane combination designated by the main program, thus four calls to EVALSUB are needed to complete the MoM impedance matrix. As each element of the sub-matrices are evaluated, EVALSUB stores the element in the MoM impedance matrix, program variable Z. By inserting the elements directly into the MoM impedance matrix, program memory requirements are reduced because the need for a large array to store the impedance sub-matrix is eliminated, and program execution time is saved because the time required to transfer the sub-matrices from temporary locations into the Z matrix is eliminated.

To complete it's assigned task, subroutine EVALSUB performs the summations of equation (4-12) for each combination of the observer plane current cell index, variable name INDEXOBS, and the source plane current cell index, variable name INDEXSRC. The variable INDEXOBS corresponds to the summation index i of equation (4-12), and variable INDEXSRC corresponds to the summation index j of equation (4-12). To increment through the observer/source cell combinations, EVALSUB uses a two-level, nested do loop. The outer loop controls variable INDEXOBS, and the inner loop controls variable INDEXSRC. Since the observer plane current cell index controls the row index of the element in the impedance sub-matrix and the source cell index controls the column index, these two do

loops actually determine which element of the sub-matrix is being evaluated.

Before the summations are started, EVALSUB uses row and column indices of the present impedance matrix element, the appropriate scale factor, variable SCALEC, for the summations

$$SCALEC = \begin{cases} \frac{j\omega aa'}{4} ; & \text{INDEXSRC} \leq N'_x, \text{INDEXOBS} \leq N_x \\ \frac{j\omega bb'}{4} ; & \text{INDEXSRC} > N'_x, \text{INDEXOBS} > N_x \end{cases} \quad (4-25)$$

where the prime indicates source plane variables.

Since the Green's functions with superscripts b_{yx} and b_{xy} in equation (4-12) are zero, the triple summations of the equation are only calculated when the observer and source cells are both x-directed or y-directed cell and the value of SCALEC is only needed for the ranges of indices i and j as indicated in equation (4-25). The triple summations of equation (4-12) are calculated in part by EVALSUB and in part by a second level subroutine named SURFINT. Subroutine EVALSUB completes the summation over the index l of equation (4-12), and SURFINT evaluates all summations for the indices m and n of equation (4-12). The details of subroutine SURFINT are presented section 4.4.2.

To complete the triple summations of equation (4-12), EVALSUB uses a do loop that is executed once for each node on the observer cell test segment. At each node, SURFINT is called to calculate the double summation over indices m and n returning the result in variable VALUSURF.

Subroutine EVALSUB then sums the product of VALUSURF, the appropriate Gaussian node weight, and SCALEC for all nodes on the test segment. The sum for all test segment nodes is assigned the variable name CELEMENT.

After completing the evaluation of the surface current field contributions, the fields produced by the surface charge density are calculated with two calls to SURFINT. The first call evaluates the sum over indices m and n with the observer point located at ρ_{xj}^+ , and the second evaluates contributions for the observer point at ρ_{xj}^- . The variable LQ is used to inform subroutine SURFINT that the call is for evaluation of a charge contribution. The flag LQ can have three values, LQ = 0 implies the call to SURFINT is for evaluation of surface current field contributions, LQ = 1 implies the call is for surface charge field contributions at ρ_{xj}^+ , and LQ = 2 implies the call is for surface charge field contributions at ρ_{xj}^- . Subroutine SURFINT returns the value of the double summation in variable VALUSURF, then EVALSUB multiplies the value by SCALEQ = $(j2\omega)^{-1}$. The contributions of the surface charge density are placed in variable QELEMENT. The final value of the sub-matrix element is found by adding variables CELEMENT and QELEMENT.

The sub-matrix element is then placed in the proper element location of Z, the MoM impedance matrix. Subroutine EVALSUB calculates the Z matrix location for each sub-matrix element using the variables ISTRTRROW, ISTRTCOL, INDEXOBS, and INDEXSRC. The variables ISTRTRROW and ISTRTCOL identify the MoM impedance matrix row and column in which the first element of the current impedance sub-matrix is located. Thus, the

MoM impedance matrix row index is (ISTRTRW - INDEXOBS - 1). The column index for the sub-matrix element is (ISTRTCOL - INDEXSRC - 1).

4.4.2 *Subroutine SURFINT*. The second level subroutine SURFINT is used by first level subroutines EVALSUB and EVALRHS to calculate the variable VALUSURF. When called by subroutine EVALSUB, SURFINT performs the double summations over the indices m and n in equation (4-12). When called by EVALRHS, SURFINT calculates the double summation over indices m and n of equation (4-17).

To complete the double summations, SURFINT uses a two-layer, nested do loop. The outer loop controls summation index m in equations (4-12) and (4-17) through variable MSURFY. As implied by its name, MSURFY controls the y-coordinate, or the node array column index, of the source cell surface integration nodes. The inner do loop controls the summation index n of equation (4-12) and (4-17) through variable NSURFX. Index NSURFX controls the x-coordinate, or the node arr row index, of the source cell surface integration nodes. The number of times these two do loops are executed is determined by the value of NUMNODES.

When called by EVALSUB to find fields from surface currents, SURFINT completes the double summations over the source cell surface integration nodes for the present observer test segment node. SURFINT calls the third level subroutine RHOFIND to calculate R for the present source surface integration and observer test segment nodes. Subroutine RHOFIND uses the variables INDEXOBS, INDEXSRC, MSURFY, and NSURFX and appropriate elements of the node coordinate data arrays to determine the coordinates for the observer and source plane integration nodes. Details

of RHOFIND are presented in section 4.4.3. The value of R is returned in variable RHODIFF. Subroutine RHOFIND also calculates the rooftop function, variable CAPT. Next, SURFINT calls subroutine EVALGRN to find value of the appropriate Green's for the present value of RHODIFF which is returned in variable GF. Details of subroutine EVALGRN are given in section 4.4.4.

Next, the product of the Gaussian node weights for MSURFY and NSURFX is computed and given the variable name GAIN. If the call from EVALSUB was for evaluation of a surface current contribution, the variable LQ will be set to 0 by EVALSUB, and the product of GAIN, CAPT, and GF is summed for all surface integration nodes to obtain VALUSURF.

If the call from EVALSUB is for the evaluation of a surface charge contribution, the value of variable LQ will be 1 or 2 and VALUSURF is calculated differently. In this case, subroutine RHOFIND will calculate RHODIFF and the surface charge density basis function, variable PI, for the observer being located at the appropriate end of the observer current cell test segment. The Green's function for the charge density contributions will then be evaluated, and the product of GAIN, PI, and GF will be summed to obtain VALUSURF.

When called by EVALRHS, SURFINT completes the summations of equation (4-17) for the aperture surface integration and the observer test segment nodes. In this case, the do loop indices MSURFY and NSURFX control the row and column indices of the array of integration nodes on the surface of the aperture. The call to subroutine RHOFIND will return RHODIFF; the value of the piecewise sinusoidal function of equation

(3-37), variable PWS; and the angle ζ , variable ZETA, as defined in equation (3-5) for y-directed sources. The appropriate Green's function polynomial and GAIN are then evaluated, and VALUSURF is obtained by summing the product of GAIN, PWS, and GF for all nodes on the aperture.

If the source and observer are coplanar and in the same current cell, the contribution of the $1/R$ term as calculated by subroutine ASYGFS is added to VALUSURF.

4.4.3 Subroutine RHOFIND. Subroutine RHOFIND is a third-level subroutine that is called by the second level subroutine SURFINT. Subroutine RHOFIND calculates R for the source and observer integration nodes, the surface current or charge density basis function or the piecewise sinusoidal function for the source integration node, and the angle ζ .

Subroutine RHOFIND first finds the position coordinates for the source integration node. The first task is to find the position of the current cell relative to the plane's center. Next, the position of the present integration node relative to the cell's center is found. The integration node's position relative to the antenna's origin is then found using the relative positions of the cell and node.

Using the array model to represent the current cell's on the planes of the antenna means finding the position coordinates of any cell is accomplished by first determining the array row and column indices for the cell and then extracting position data from the appropriate data arrays, XXCOORD and XYCOORD or YXCOORD and YYCOORD.

The array indices are found by using variable INSEXSRC to determine the cell's ordinal number within the array of x-directed or y-directed current cells. Recall, $1 \leq \text{INDEXSRC} \leq N$, where N is the total number of x- and y-directed cells on the source plane. The current cells on a plane are numbered such that $\text{INDEXSRC} = 1$ for the first x-directed cell and $\text{INDEXSRC} = N$ for the last y-directed cell. Therefore, for an x-directed current cell, INDEXSRC is the cell's ordinal number.

Once the ordinal number is known, the row and column indices are found in two steps. First, the ordinal number is divided by the number of current cells per row of the x-directed cell array. The whole number portion of the quotient is one greater than the cell's row index, variable IROW. For instance with 4 cells in a row and an ordinal number of 9, the quotient is 2.25, thus $\text{IROW} = 3$.

Next the column index, variable ICOL, is found by subtracting the product of the row index less one and the number of cells in a row of the x-directed cell array from the cell's ordinal number. Continuing the example, with the row index of 3, $\text{ICOL} = 9 - [4 \times (3-1)] = 1$. Thus, for the patch of Figure 8, the ninth x-directed cell corresponds to element (3,1) of the current cell array. The x-coordinate of this cell's center is contained in data array element $\text{XXCOORD}(3, \text{JSRCPLAN})$, and the cell center's y-coordinate is contained in $\text{XYCOORD}(1, \text{JSRCPLAN})$.

To obtain the ordinal number for a y-directed cell, the number of x-directed cells on the plane, variable $\text{NX}(\text{JSRCPLAN})$, must be subtracted from the value of INDEXSRC. The indices IROW and ICOL are then calcu-

lated in the same steps as those for an x-directed cell. The x-coordinate of the cell's center is YXCOORD(IROW,JSRCPLAN) and the y-coordinate of the cell's center is YYCOORD(ICOL,JSRCPLAN).

Since SURFINT progresses through the array of integration nodes on the current cell using a row and column index, no manipulations of the integration node indices are needed. For all cells, the x-coordinate of the node's relative position is XCOL(NSURFX,JSRCPLAN) and the y-coordinate is YROW(MSURFY,JSRCPLAN)

The cell and node relative position coordinates are summed to find the node's absolute position coordinates and the values are stored in the one dimensional array RHOPRIME. Element RHOPRIME(1) contains the x-coordinate of the node's location, and the element RHOPRIME(2) contains the y-coordinate.

Having determined the source node position, the basis functions of equations (3-13) and (3-18) and the magnetic current of equation (3-40) can be calculated. From equations (3-13) and (3-18), the basis functions are dependent on the value of $(\rho'_j - \rho'_{imm})$, which is actually the position of the integration node relative to the center of the cell. Thus, the surface current basis function, CAPT, and the surface charge density basis function, PI, are calculated as follows

$$\text{CAPT} = \begin{cases}
 1 + \frac{\text{XCOL(NSURFX, JSRCPLAN)}}{\text{A(JSRCPLAN)}} & \text{XCOL(NSURFX, JSRCPLAN)} < 0 \\
 1 - \frac{\text{XCOL(NSURFX, JSRCPLAN)}}{\text{A(JSRCPLAN)}} & \text{XCOL(NSURFX, JSRCPLAN)} > 0 \\
 1; \text{Otherwise} &
 \end{cases} \quad \begin{array}{l} \text{INDEXSRC} \\ < \text{NX(JSRCPLAN)} \end{array} \quad (4-26)$$

$$\text{PI} = \begin{cases}
 -1 & \text{XCOL(NSURFX, JSRCPLAN)} < 0 \\
 1 & \text{XCOL(NSURFX, JSRCPLAN)} > 0 \\
 0; \text{Otherwise} &
 \end{cases} \quad \begin{array}{l} \text{INDEXSRC} < \text{NX(JSRCPLAN)} \end{array}$$

$$\begin{cases}
 -1 & \text{YROW(MSURFY, JSRCPLAN)} < 0 \\
 1 & \text{YROW(MSURFY, JSRCPLAN)} > 0 \\
 0; \text{Otherwise} &
 \end{cases} \quad \begin{array}{l} \text{INDEXSRC} < \text{NX(JSRCPLAN)} \end{array} \quad (4-27)$$

If the source plane is the antenna aperture, then the piecewise sinusoidal magnetic current function, variable PWS, is evaluated by RHOFIND. Since the aperture is treated as a single x-directed current cell, the integration node's y-coordinate on the aperture, variable XROW(MSURFY,1), determines the value of PWS. Subroutine SEGMENT segments the aperture such that A(1) = W/2 and B(1) = L, therefore

$$\text{PWS} = \frac{\sin \left[KE * \left(\frac{B(1)}{2} - |\text{MSURFY}(IROW, JSRCPLAN)| \right) \right]}{2 * A(1) * \sin \left(\frac{KE * B(1)}{2} \right)} \quad (4-28)$$

where * denotes scalar multiplication.

The observer test segment node location is found in the same way as the source integration node location, except the ordinal number of the cell is found based on the value of INDEXOBS, and the data arrays' second indices are now IOBSPLAN.

When the field contributions from surface currents are being evaluated, the observer cell integration node index is controlled by variable LINENODE. Since the test segments are centered in the current cell, only one coordinate is needed to locate the node relative to the current cell's center. On an x-directed cell, the line integration is along an x-directed contour, and the coordinates of the node are

$$\begin{aligned} \text{RHO}(1) &= \text{XXCOORD}(\text{ICOL}, \text{IOBSPLAN}) + \text{SEGX}(\text{LINENODE}, \text{IOBSPLAN}) \\ \text{RHO}(2) &= \text{XYCOORD}(\text{IROW}, \text{IOBSPLAN}) \end{aligned} \quad (4-29)$$

On a y-directed cell, the line integration is along a y-directed contour, and the coordinates of the node are

$$\begin{aligned} \text{RHO}(1) &= \text{XXCOORD}(\text{IROW}, \text{IOBSPLAN}) \\ \text{RHO}(2) &= \text{YYCOORD}(\text{ICOL}, \text{IOBSPLAN}) + \text{SEGY}(\text{LINENODE}, \text{IOBSPLAN}) \end{aligned} \quad (4-30)$$

If the contributions from the surface charge density is being evaluated, the observer location is at either end of the cell's test segment. The value of variable LQ informs RHOFIND at which end of the test segment the observer is located as discussed in section 4.4.1. The

location of the test segment's ends relative to the current cell's center is given in equation (11). Therefore, on an x-directed cell the x-coordinate of the test segment ends are found as follows:

$$\text{RHO}(1) = \begin{cases} \text{XXCOORD(ICOL, IOBSPLAN)} + \frac{\text{A(IOBSPLAN)}}{2}; \text{LQ} - 1 \\ \text{XXCOORD(ICOL, IOBSPLAN)} - \frac{\text{A(IOBSPLAN)}}{2}; \text{LQ} - 2 \end{cases} \quad (4-31)$$

and the y-coordinate for the end of the test segment is equal to that of the current cell's center.

For a y-directed current cell, the x-coordinate of the test segment's ends is equal to that of the current cell, and the y-coordinate for the ends is given by

$$\text{RHO}(2) = \begin{cases} \text{YYCOORD(ICOL, IOBSPLAN)} + \frac{\text{B(IOBSPLAN)}}{2}; \text{LQ} - 1 \\ \text{YYCOORD(ICOL, IOBSPLAN)} - \frac{\text{B(IOBSPLAN)}}{2}; \text{LQ} - 2 \end{cases} \quad (4-32)$$

Having calculated the x- and y-coordinates for the positions of the observer and source integration nodes, the value of variable RHODIFF, can be found

$$\text{RHODIFF} = [(RHO(1) - RHOPRIME(1))^2 + (RHO(2) - RHOPRIME(2))^2]^{\frac{1}{2}} \quad (4-33)$$

If the aperture is the source plane, JSRCPLAN = 1 and the variable ZETA is calculated in accordance for equation (3-5) for y-directed sources. Since the x- and y-coordinates of the position vectors are known, the value of ϕ and ϕ' are the inverse tangent of the y-coordinate divided by the x-coordinate.

4.4.4 Subroutine EVALGRN. Subroutine EVALGRN is a third level subroutine called by SURFINT to calculate the value of the appropriate Green's function polynomial given the present value of RHODIFF.

First, value of RHODIFF is compared to the range information obtained from data file GREENFS.DAT to determine which coefficients and polynomial form are to be used. Next, the subroutine determines which Green's function is needed based on the values of IOBSPLAN, JSRCPLAN, INDEXOBS, NX(IOBSPLAN), and LQ. Calculating the Green's function is then only a matter of evaluating the appropriate polynomials to obtain the components of the Green's functions' value. The result of the calculations is returned to SURFINT in variable GF.

4.4.4 Subroutine EVALRHS. Subroutine EVALRHS is the first-level subroutine that calculates the elements in the column matrix of inner-products as defined in equation (4-17). Subroutine EVALRHS is called twice by the main program. The first call evaluates the inner products for the patch of interface 2b and the second evaluates the inner-products for the patch of interface 3b.

In equation (4-17), the matrix element's row is determined by the observer current cell index, with one row for each cell on the observer plane. The source plane for all calculations is the antenna aperture.

Since the aperture is modeled as a single x-directed current cell, the value of INDEXSRC is always one.

Subroutine EVALRHS controls the variable INDEXOBS to calculate the inner-product for each observer cell. At each observer cell, EVALRHS completes the summations of equation (4-17) by controlling the summation over index l , variable LINENODE, and calling subroutine SURFINT to complete the summation over indices m and n of equation (4-17). For calls from EVALRHS, SURFINT returns the variable VALUSURF where

$$\text{VALUSURF} = \sum_{m=1}^{\text{NUMNODES}} \sum_{n=1}^{\text{NUMNODES}} w_m w_n \begin{cases} G_E^{bxy}(\rho_{il}, \rho'_{mn}) M_y(y') ; & 1 \leq \text{INDEXOBS} \leq N_{2x} \\ G_E^{byy}(\rho_{il}, \rho'_{mn}) M_y(y') ; & N_{2x} < \text{INDEXOBS} \leq N \end{cases} \quad (4-34)$$

Subroutine EVALRHS then uses VALUSURF to complete the calculation of the inner-product as follows:

$$\text{RHS}(\text{ISTRTRROW} + \text{INDEXOBS} - 1) = \begin{cases} \frac{aWL}{8} \sum_{l=1}^{\text{NUMNODES}} \text{VALUSURF} \\ \frac{bWL}{8} \sum_{l=1}^{\text{NUMNODES}} \text{VALUSURF} \end{cases} \quad (4-35)$$

The result of equation (4-35) is then placed in the appropriate location of the inner product data array, variable name RHS. To inform EVALRHS of the correct element index of RHS, the main program sets variable ISTRTRROW before EVALRHS is called each time. Variable ISTRTRROW

identifies in which RHS element the inner-product for the first observer cell must be stored. The index for the element of matrix RHS being calculated is given by (ISTRTRW + INDEXOBS - 1).

4.5 Matrix Equation Solution Subroutines

Subroutine SOLVNVRs solves for the expansion coefficients using matrix inversion and multiplication. The inversion of the MoM impedance matrix is completed by a second-level routine named INVERT.

4.5.1 Subroutine SOLVNVRs. Subroutine SOLVNVRs finds the solution to the general matrix equation $A\underline{x} = \underline{b}$, \underline{x} being the unknown vector, by calculating $\underline{x} = A^{-1}\underline{b}$. The subroutine call for SOLVNVRs is "CALL SOLVNVRs(Z, IDIM, RHS, ALPHAS)" where Z is the IDIM x IDIM matrix equivalent to the matrix A in the equation $A\underline{x} = \underline{b}$, RHS is the known forcing function of the equation equivalent to the vector \underline{b} , and ALPHAS is the unknown equivalent to the vector \underline{x} .

Subroutine SOLVNVRs first calls subroutine INVERT to find the inverse of Z which is returned in the matrix ZINV. Next, the solution matrix ALPHAS is calculated by forming the matrix product of ZINV and RHS.

4.5.2 Subroutine INVERT. Subroutine INVERT is a third-level subroutine called by subroutine SOLVNVRs to calculate the inverse of the matrix specified in the subroutine call. The subroutine call is 'CALL INVERT(BINPUT, IDIM, INVERSE) where BINPUT is the matrix to be inverted,

IDIM is the dimension of BINPUT, and INVERSE is the variable name assigned to the inverse of BINPUT. Subroutine INVERT uses Gaussian elimination to calculate the inverse matrix.

Since analysis of the antenna requires all original matrices be preserved, the first task of INVERSE is to transfer the matrix BINPUT into a local matrix INPUT. Duplicating the BINPUT matrix is necessary because the reduction to triangular form will overwrite elements of the original matrix with row permutation parameters. Since the inverse matrix will be calculated column by column, the alterations to the original matrix must be tracked via permutation parameters so the same alterations may be made to each identity matrix column. More detail on the permutation parameters is in the subsequent discussion.

Once the BINPUT matrix is copied, the next step is to transform the INPUT matrix into triangular form using the standard row manipulations of Gaussian elimination. Partial pivoting is used to reduce rounding errors during Gaussian elimination [12:28]. As the rows of the matrix are pivoted, the pivot changes are stored in the one-dimensional array IPIVOT. For instance, if row I was pivoted with row J during the elimination process, IPIVOT(I) would equal J. If the row was not pivoted, the element IPIVOT(I) will be I.

As each row is changed, row permutation parameters are stored in the INPUT matrix elements that would be zero with the matrix in lower triangular form. For instance, if the element INPUT(I,J) is reduced to zero by multiplying all elements of row J by the factor INPUT(I,J)/INPUT(J,J) and then subtracting the result from all elements of row I, the

permutation parameter for INPUT(I,J) is $-\text{INPUT}(I,J)/\text{INPUT}(J,J)$. The changes to every row are recorded in this manner.

After the matrix is in triangular form, the row permutation parameter contained in element INPUT(K,L) will show what factor row L was multiplied by so that subtracting row L from row K would produce a zero value for element INPUT(K,L).

With the matrix in triangular form, the inverse matrix is calculated a column at a time by backsolving the system $Ax = b$ where A is the triangular matrix INPUT, x is the ith column of the inverse matrix, and b is the ith column of the IDIM x IDIM identity matrix, local variable RHS.

Before backsolving for the inverse column elements, matrix RHS must be altered in the same way as the original INPUT matrix was altered during reduction to triangular form. The elements of RHS are transformed one at a time by repeating these three steps for each element.

1) First, as the element RHS(K) is altered, the entry for IPIVOT(K) is checked, if IPIVOT(K) $\neq K$, then elements RHS(K) and RHS(IPIVOT(K)) are exchanged.

2) Sum the products of the current entry in RHS(K) and the permutation parameters located on row K of matrix INPUT which have column indices less than K. This summation, variable name DEL(K), is the total change for RHS(K) resulting when matrix INPUT was reduced to triangular form.

3) Form the transformed RHS(K) by adding DEL(K) to RHS(K).

After these manipulations, the column matrix RHS is in the same form as if it had been placed in an augmented matrix with INPUT and undergone the row manipulations while INPUT was being reduced to triangular form.

When RHS has undergone the appropriate changes, the system can be backsolved to obtain the elements for the column of the inverse matrix. The inverse matrix elements are found beginning with element IDIM and continuing to element 1. The algorithm used to complete the backsolving is the same as that found in Figure 2-1 of [10], except the variable names have been changed to match those of subroutine INVERSE, and as each element of the inverse matrix is found, the element is placed into its proper position in the matrix INVERSE.

4.6 Data Output Subroutines

All data output from the MoM solution software is handled by the first-level subroutine OUTPUT. Subroutine OUTPUT uses the second-level subroutine JDISTR to calculate data for the surface current distributions.

4.6.1 Subroutine OUTPUT. Subroutine OUTPUT first writes the surface current expansion coefficients to file COEFFS.OUT. Before writing to file, OUTPUT performs several calculations to determine the

format to be used for the coefficients. The coefficients are written in two columns, with the coefficients for the x-directed then y-directed cells on the patch of interface 2b being the first in the file. After the coefficients are written to file, the subroutine to calculate the surface current distributions is called.

4.6.2 Subroutine JDISTR. Subroutine JDISTR calculates the value of the surface currents along the centers of each row of x-directed and y-directed current cells on both antenna patches. For each current cell, the surface current function is calculated at five sample points.

The surface current data is first calculated for the cells on the patch of interface 2b then interface 3b, with the x-directed cell data being the first calculated for both patches. There are five samples taken at equal intervals across each current cell. For instance, for x-directed cells, the sample points are spaced a distance of $a/2$ with the first point being located on the leftmost boundary of the left charge cell. With these sample point locations and the overlap of current cells, the three sample points in the right charge cell of the current cell overlap with the first three sample points in the left charge cell of the current cell immediately to the right. Subroutine JDISTR compensates for the overlap by summing the surface current contributions for both cells sharing a charge cell.

The progression over a row of charge cells is controlled by a two layer, nested do loop. The outer most loop controls the cell within the row and the inner do loop controls the index of the sample point. At each cell in the row, the index of the expansion coefficient for the

cell is first calculated, then the surface current value at the sample point is found.

After the surface current values for the complete row have been calculated, they are normalized to units of millamps/square meter. Next, the y-coordinate (x-coordinate) of the x-directed (y-directed) row's center is written to file along with the x-coordinate (y-coordinate) and surface current value at each sample point. Since the surface current is a complex quantity, the real components are written in file JREAL.OUT and the imaginary components are written to file JIMAG.OUT.

V. Results

This chapter presents the data obtained from the MoM solution software described in Chapter IV. The MoM software was used to find the solutions for two different antennas using both four and six node Gaussian quadrature. The results for each run of the software are contrasted and compared.

5.1 Physical Description of the Sample Antennas

The MoM solution data presented in this chapter was obtained using the following examples of aperture-fed, stacked patch antennas. All solutions are for an operating frequency of 3.7 GHz.

5.1.1 Antenna #1. The antenna example referred to as antenna #1 has resonance frequencies of 3.62 Ghz and 4.05 GHz [30:48] and is described as follows:

- The thickness of each substrate is 0.158 cm, and all substrates have $\epsilon_r = 2.2$ and $\mu_r = 1.0$.

- The aperture has an x-dimension of 0.15 cm and a y-dimension of 1.1 cm.
- Both patches have dimensions of 2.5 x 2.5 cm and are centered over the aperture.

The MoM segmentation results in 45 x-directed and 40 y-directed current cells on each patch. On each patch, $a = 0.25$ cm and $b = 0.5$ cm. The MoM impedance matrix is 170 x 170 and each impedance sub-matrix is 85 x 85.

5.1.2 Antenna #2. The antenna referred to as antenna #2 is identical to antenna #1, except the patch of interface 3b is 2.65 x 2.65 cm. Measurements of this design shows resonant frequencies for this antenna at 3.54 GHz and 4.15 GHz [30:51].

The MoM impedance matrix and sub-matrices for antenna #2 have the same dimensions. The cell dimensions for the patch on interface 2b are the same as for antenna #1, but on the patch of interface 3b, $a = 0.265$ cm and $b = 0.53$ cm.

5.2 Surface Current Data

Figures 5-1 through 5-10 are plots of the surface current data as calculated by the MoM software. The plots were made using data obtained from the files JREAL.DAT and JIMAG.DAT and are presented in pairs, with the real component of the surface current shown in the left plot and the

imaginary in the right plot. As discussed in Section 4.6.2, subroutine JDISTR produces data at sample points located in the center of the current cells along the row, and the location of the row is given above each plot.

5.2.1 *Surface Currents on Antenna #1.* Figure 5-1 shows the x-directed currents in the top three of the five rows of x-directed current cells on the patch of interface 2b for antenna #1. Comparison of the magnitudes of the real and imaginary components of the currents shows the imaginary component of the currents are clearly dominant. The reason for this dominance is that the antenna is operating near resonance at 3.7 GHz and at resonance the surface currents are always dominated by the imaginary component [18:321]. Also, both components are symmetric along the x- and y-axes with respect to the cell's center.

Figure 5-1 also shows how the real components of the currents are fairly constant as the cell's is traversed along the y-axis. On the other hand, the imaginary components vary appreciably along the y-axis, peaking in magnitude at the cell's center (see plot (c) of Figure 5-1). This peak in the imaginary component of the currents means the strongest coupling occurs at the patch's center. These same features are evident in the x-directed currents on the patch of interface 3b (see Figure 5-4).

Figures 5-2 and 5-3 show the y-directed currents on the patch of interface 2b. Figure 5-2 shows currents in the first three rows of y-directed current cells on the patch, and Figure 5-3 shows the currents in rows four, five, and six. While the magnitudes of the y-directed

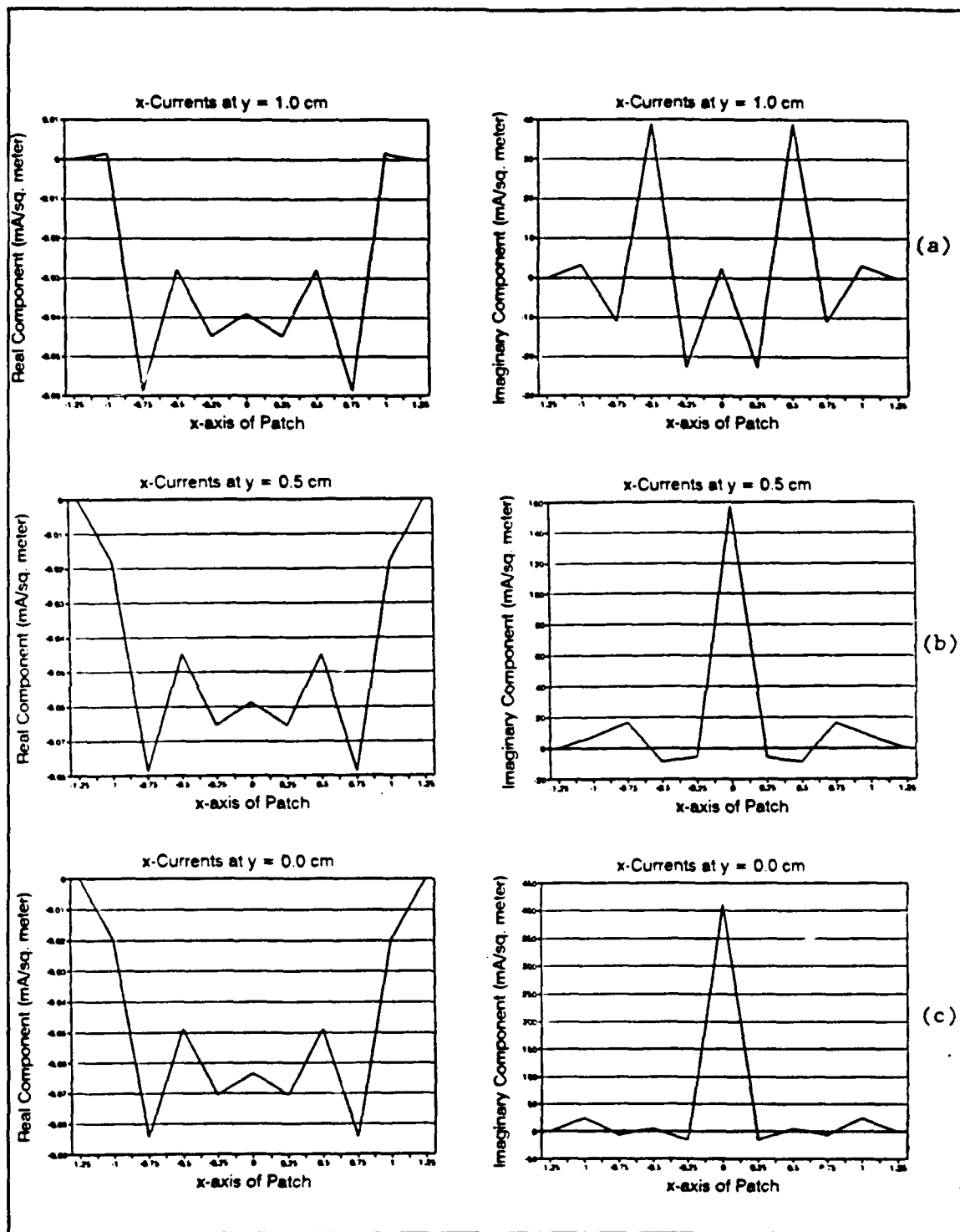


Figure 5-1 Plots of x-directed Surface Currents for the First Three Rows of x-Cells on the Patch of Interface 2b, Antenna #1 (data from four node quadrature)

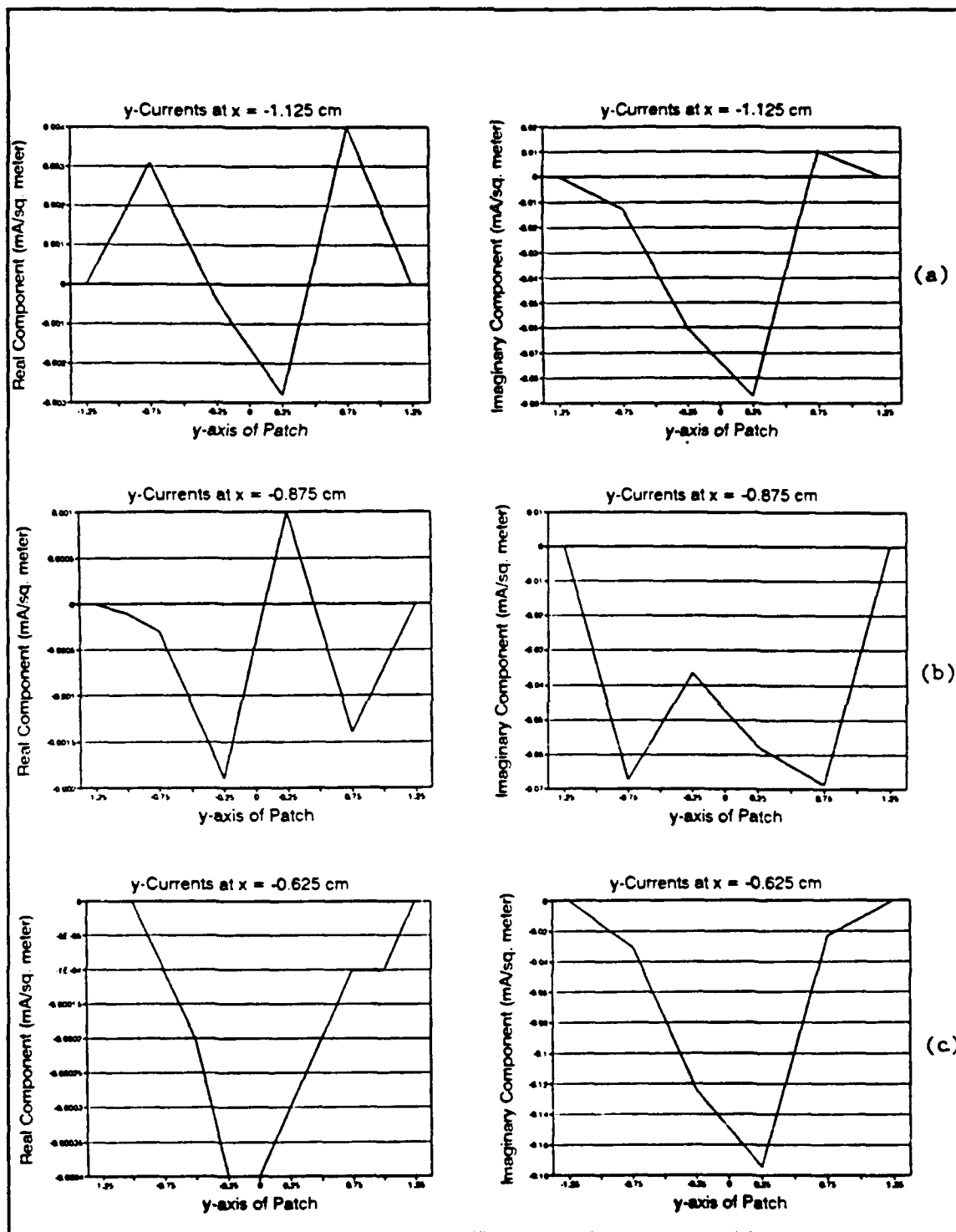


Figure 5-2 Plots of y-directed Surface Currents for the First Three Rows of y-cells on the Patch of Interface 2b, Antenna #1; (data from four node quadrature)

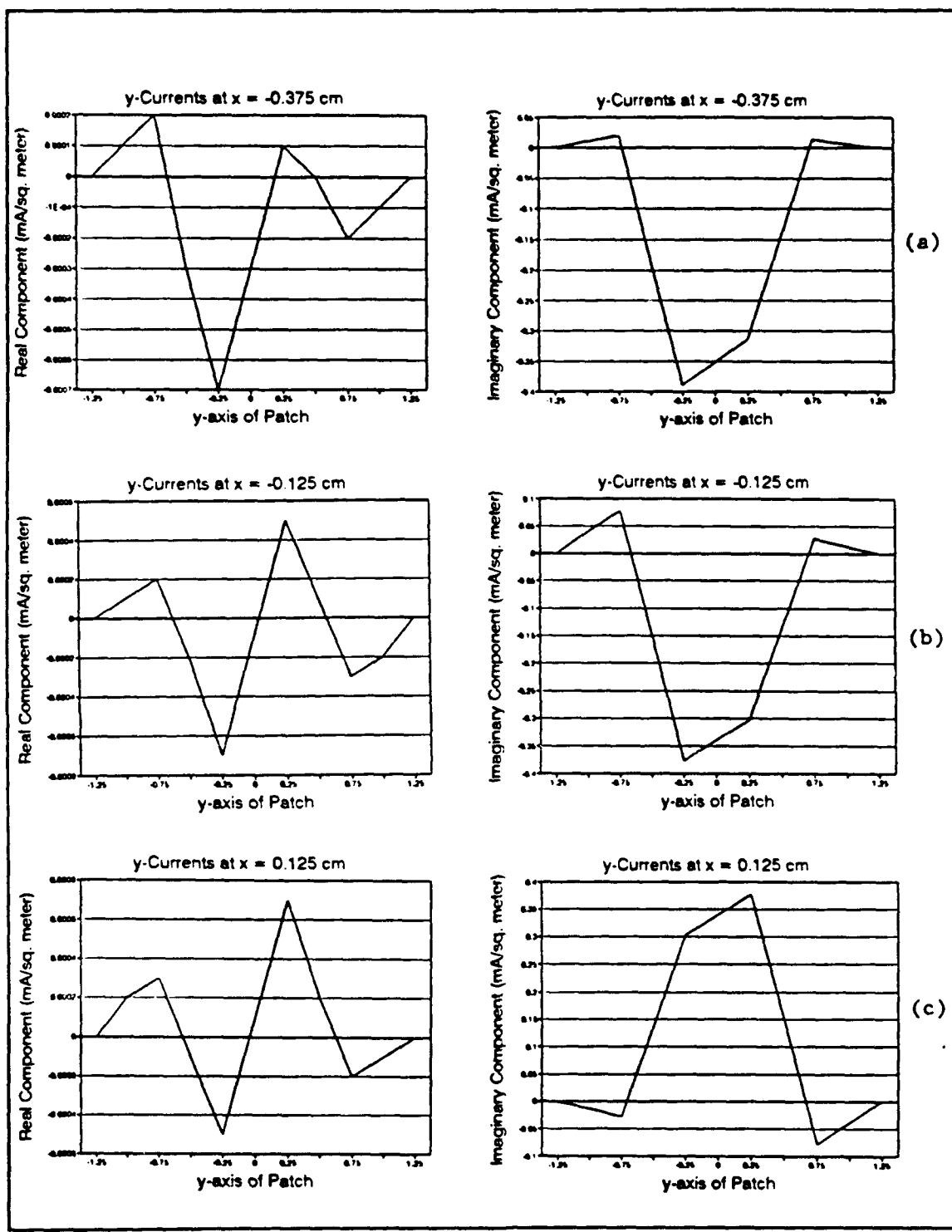


Figure 5-3 Plots of y-directed Surface Currents for Rows Four, Five, and Six of y-cells on the Patch of Interface 2b, Antenna #1 (data from four node quadrature)

currents are much smaller than those of the x-directed currents, the dominance of the imaginary component of the currents is evident. In contrast to the x-directed currents, the y-currents appear to show no symmetry at all. However, close comparison of plots (b) and (c) in Figure 5-2 shows the surface currents are symmetric along the cell's x-axis with respect to the center of the cell, but as the center of the cell is crossed, the currents experience a 180° phase shift. This feature is also evident in all data obtained for the y-directed currents. (see Figure 5-6, plots (b) and (c) and Figure 5-10, plots (a) and (b)).

Figures 5-4 through 5-6 show the surface currents on the patch of interface 3b. These currents have the same general features as those explained for the patch of interface 2b. As compared to the currents of interface 2b, the currents of interface 3b are about one order of magnitude smaller than those of interface 2b. Also, a comparison of plots (a) and (b) of Figures 5-1 and 5-4 shows that there is a phase shift of 180° between the imaginary components of the currents on the two patches. As was the case with the patch of interface 2b, the imaginary component of the currents peaks at the cell's center.

Figures 5-7 and 5-8 are plots of the same currents as shown in Figures 5-1 and 5-4, respectively, except data plotted in Figures 5-7 and 5-8 were obtained using six node quadrature. While the distributions of the real current components have the same general shapes for four and six node quadrature, the distributions of the imaginary

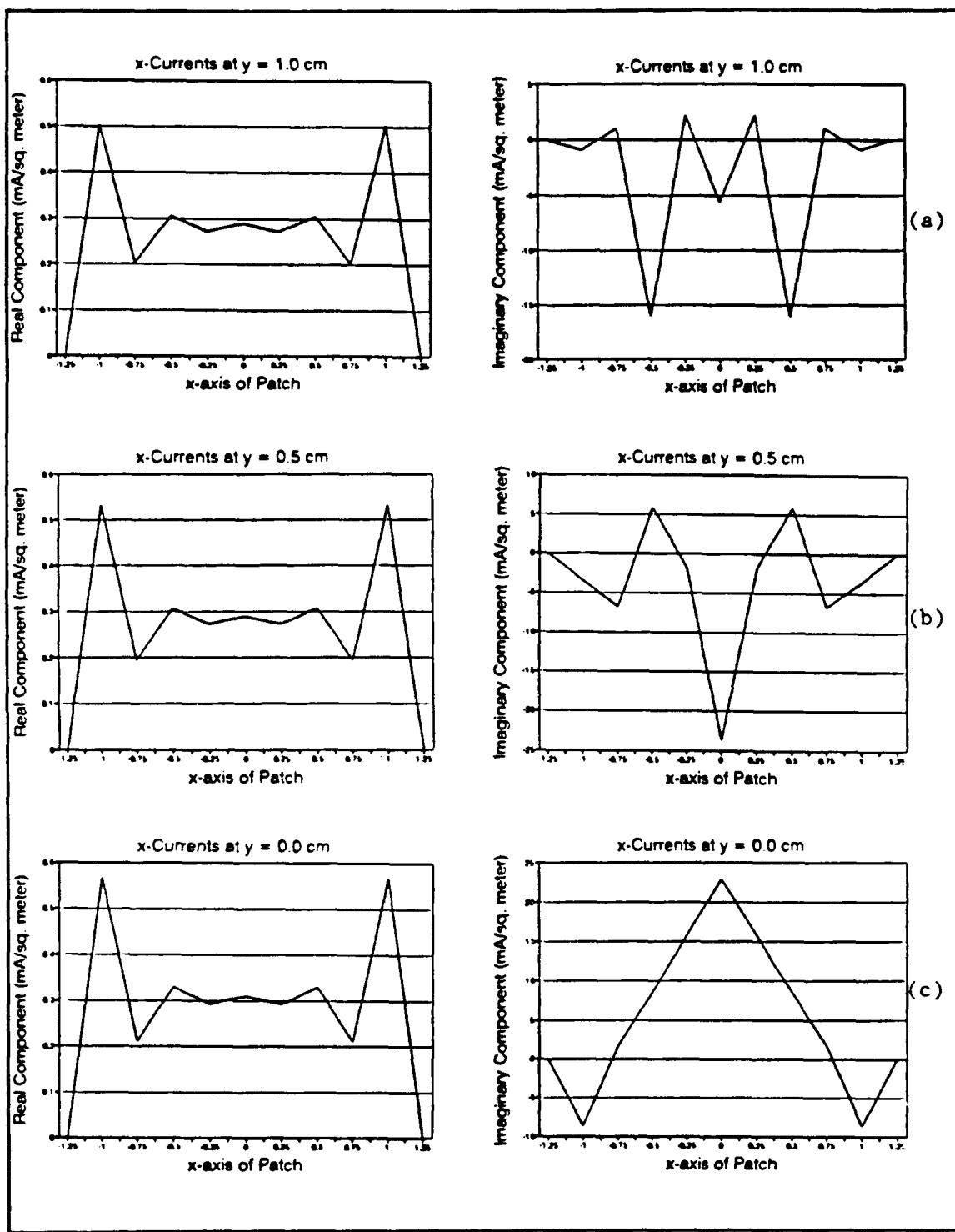


Figure 5-4 Plots of x-directed Currents for the First Three Rows of x-cells on the Patch of Interface 3b, Antenna #1 (data from four node quadrature)

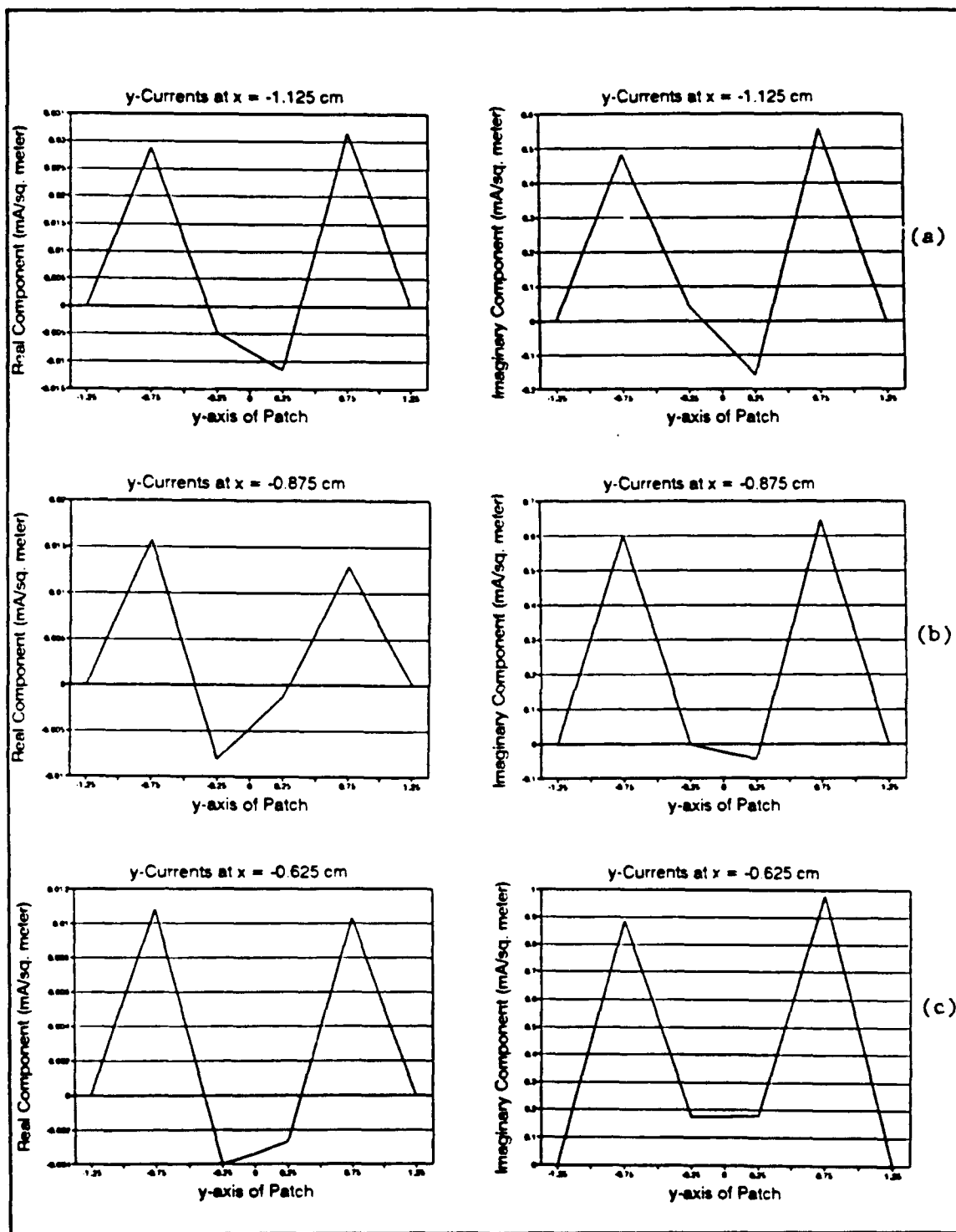


Figure 5-5 Plots of y-directed Currents for the First Three Rows of y-cells on the Patch of Interface 3b, Antenna #1 (data from four node quadrature)

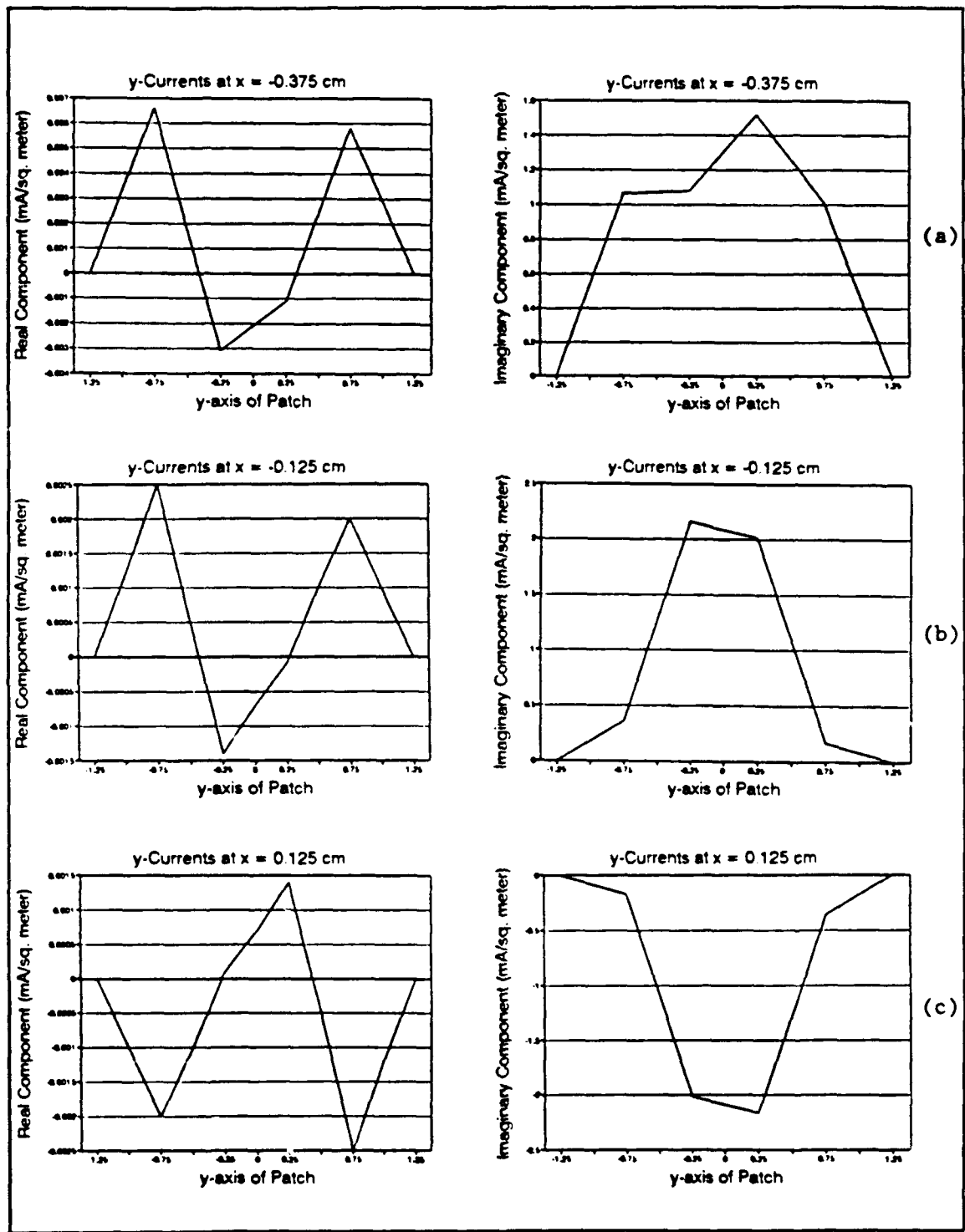


Figure 5-6 Plots of y-directed currents for the First Three Rows of y-cells on the Patch of Interface 3b, Antenna #1 (data from four node quadrature)

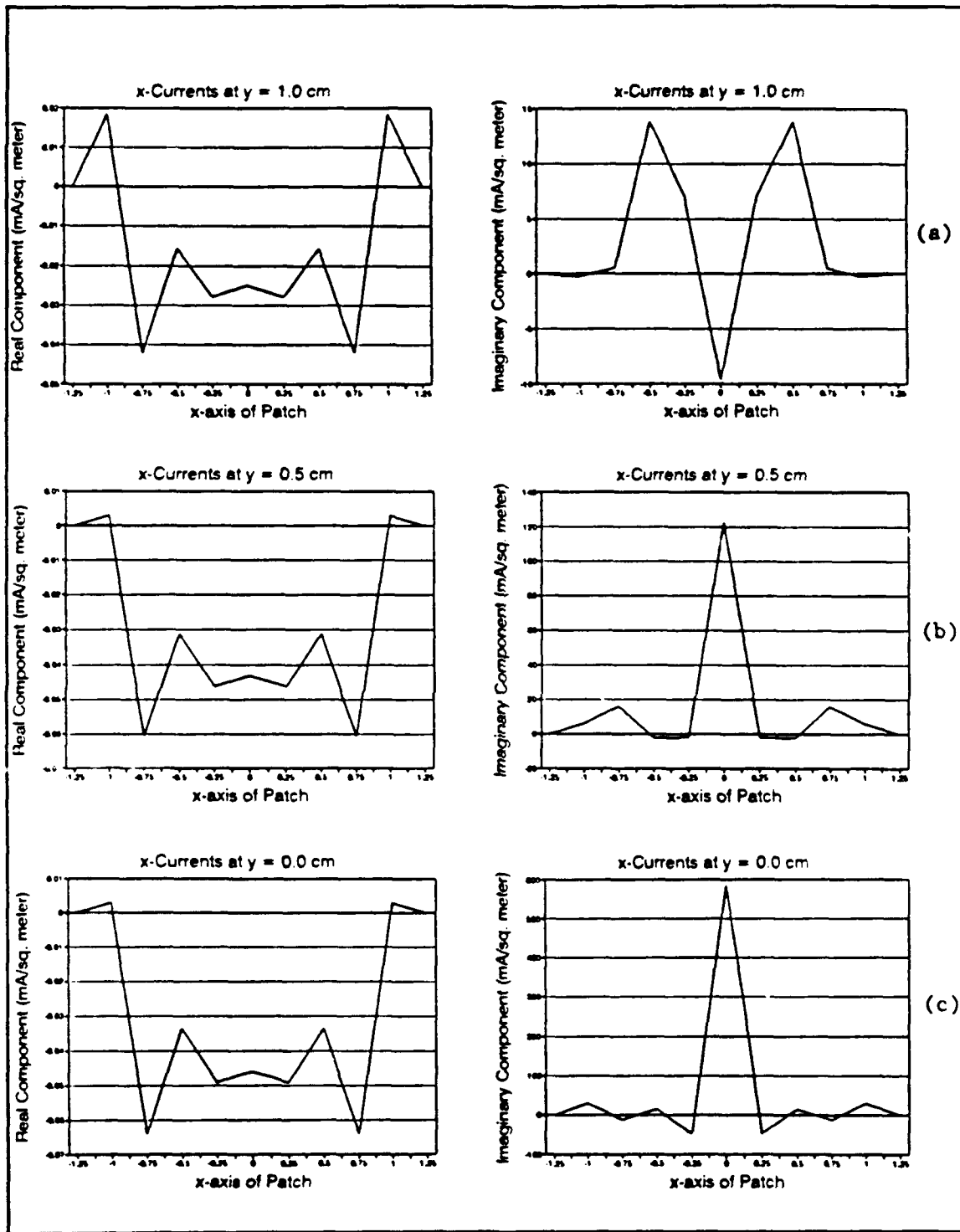


Figure 5-7 Plots of x-directed Currents for the First Three Rows of x-cells on the Patch of Interface 2b, Antenna #1 (data from six node quadrature)

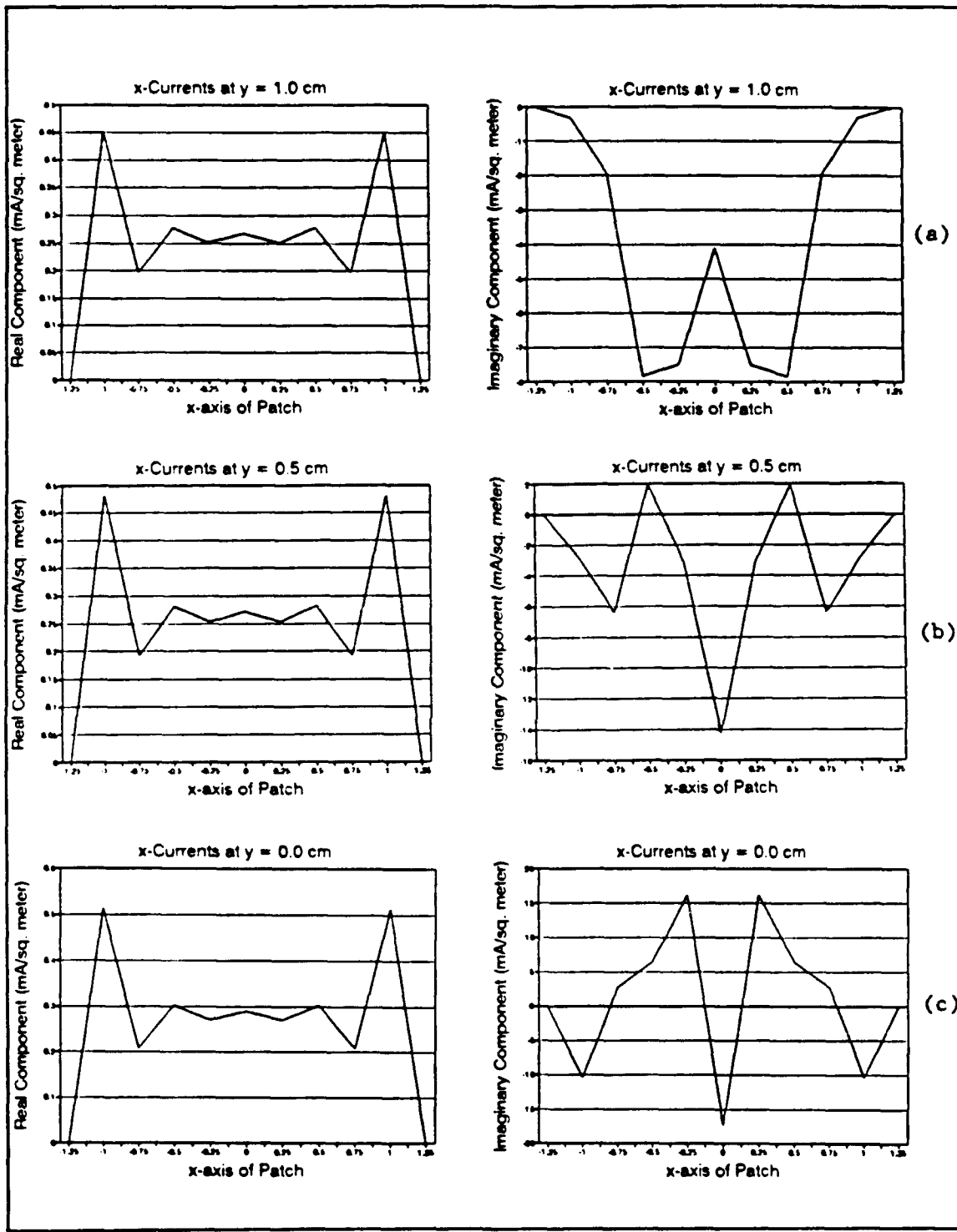


Figure 5-8 Plots of x-directed Currents for the First Three Rows of x-cells on the Patch of Interface 3b, Antenna #1 (data from six node quadrature)

components vary significantly. The disagreement between results is best shown by a comparison of plot (c) in Figures 5-7 and 5-8. This disagreement could be caused by an inaccuracy of the Green's function approximations. Tests of the approximations showed the approximations were accurate for $R > 0.0008$. For six node quadrature with source and observer located in the same cell, the values of R can go well below this limit, so there are some errors in the Green's function for this case. Since the self-terms of the impedance matrix are dominant, the error in the Green's functions has a pronounced impact on the results.

5.2.2 *Surface Currents on Antenna #2.* Figure 5-9 shows the x-directed currents for the first three rows of x-cells on the patch of interface 3b for antenna #2. Comparisons with Figure 5-4 show the current distribution are generally the same, but the current magnitudes on antenna #2 are larger than those of antenna #1. This increase in current magnitude is most likely due to the fact that the larger patch of antenna #2 results in stronger coupling with the sources of the antenna. Comparisons of tabulated current distributions data show the surface current magnitudes on the patch of interface 2b in antenna #2 are about 10% smaller than the same currents in antenna #1. This finding also supports the idea that the larger patch on interface 3b results in stronger electromagnetic coupling with the sources in the antenna.

Figure 5-10 shows the y-directed currents in rows five and six on the patch of interface 3b in antenna #2. Compared to the same y-directed currents on antenna #1, these currents are slightly greater in

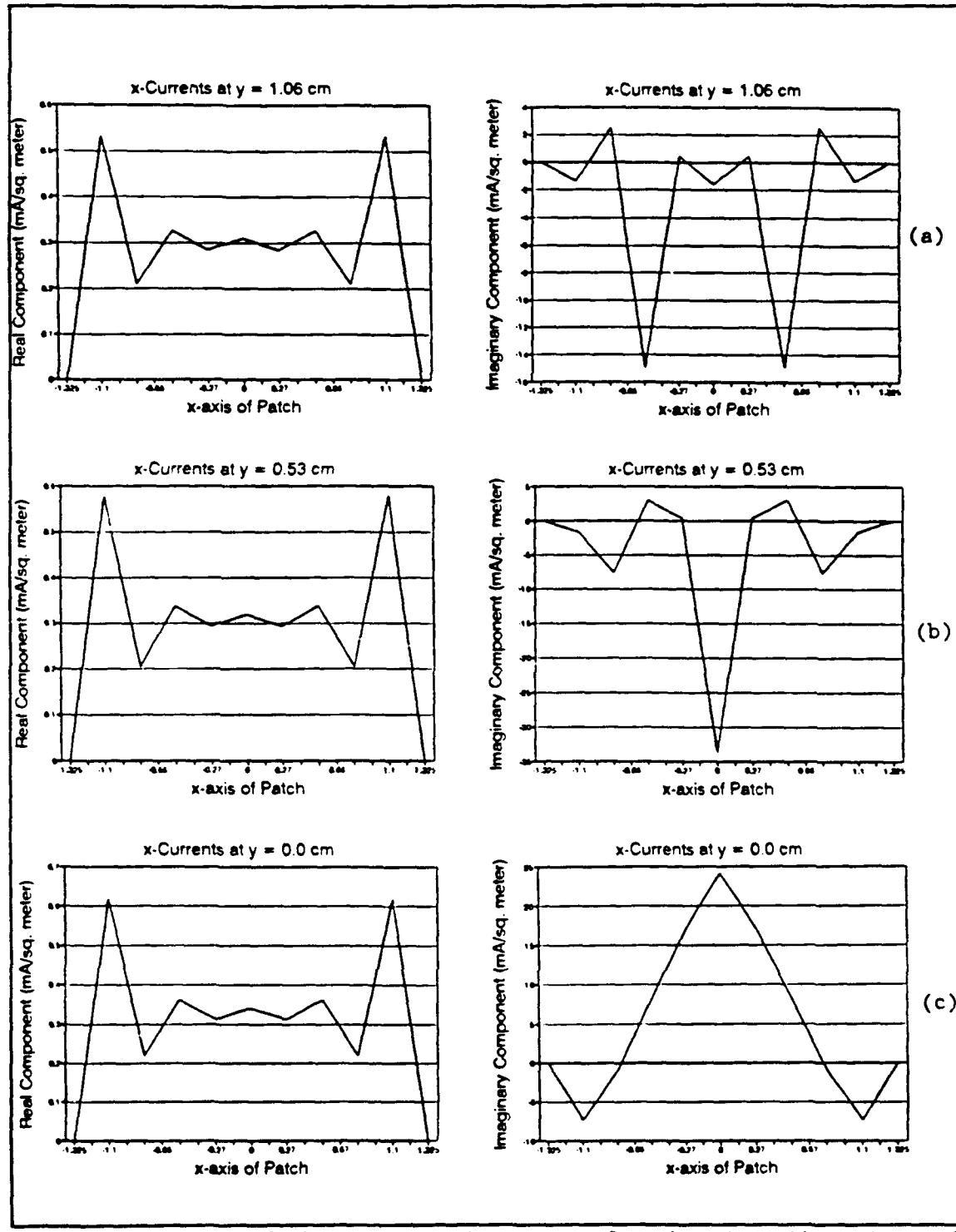


Figure 5-9 Plots of the x-directed Currents for the First Three Rows of x-cells on the Patch of Interface 3b, Antenna #2 (data from four node quadrature)

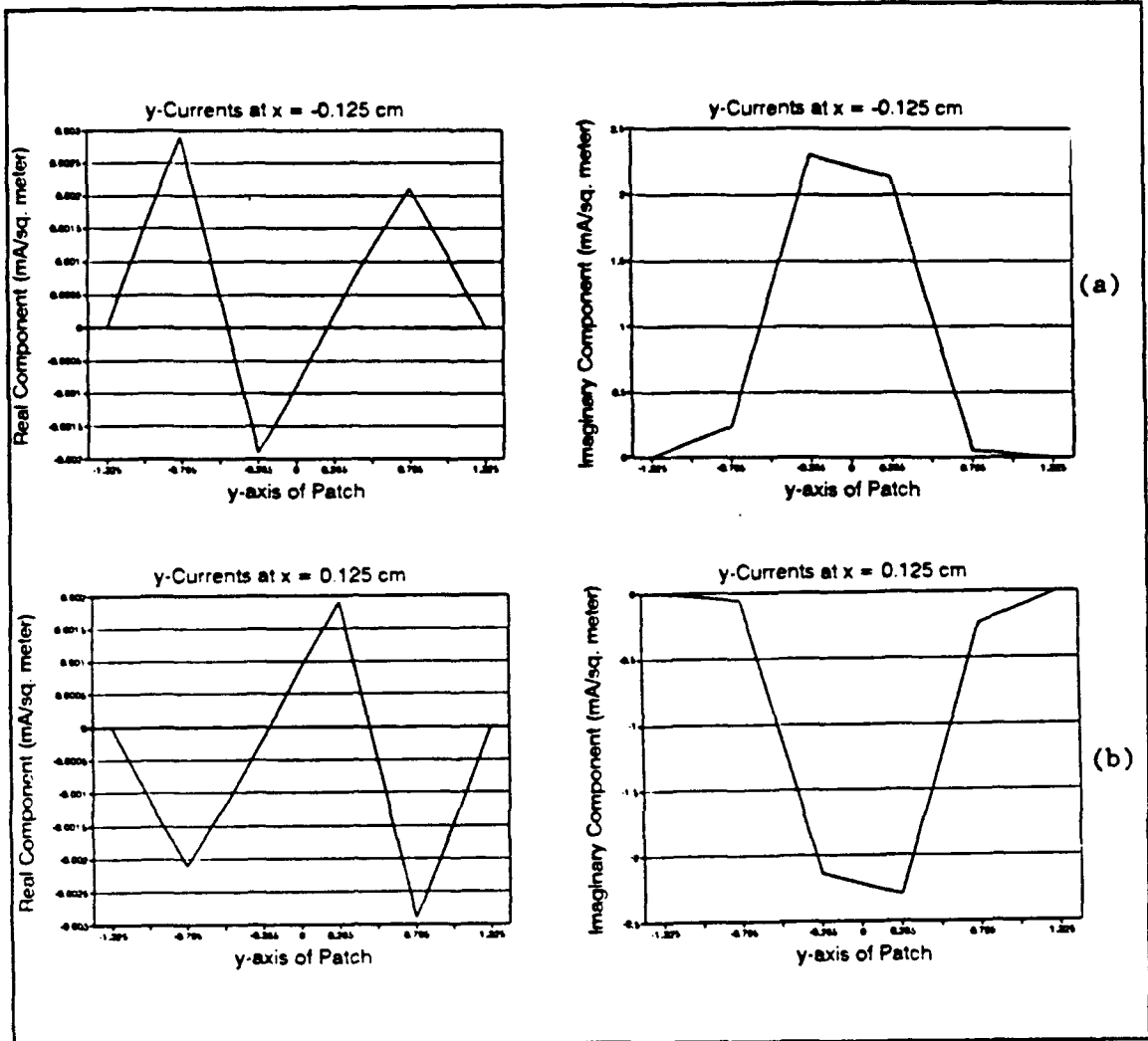


Figure 5-10 Plots of the y-directed currents for Rows Five and Six of y-cells on the patch of Interface 3b, Antenna #2 (data from four node quadrature)

magnitude, but essentially identical. Comparing plots (a) and (b) of Figure 5-10 also shows the y-directed currents of antenna #2 have the same symmetry and phase shift characteristics as antenna #1.

5.3 Surface Current Expansion Coefficients

A listing of the surface current/charge density expansion coefficients obtained with four node Gaussian numerical integration for the patch on interface 2b of antenna #1 is given in Table 5-1 and for interface 3b is given in Table 5-2. Several observations concerning the coefficients can be made, which are valid for both the four node and six node solutions.

As illustrated by the surface current plots of section 5.2, the expansion coefficients for the x-directed surface currents are symmetric about the center of the cell. An examination of x-directed coefficients 1 through 9 on either patch shows the symmetry in x, and comparing coefficients 1 through 9 with coefficients 37 through 45 shows the symmetry in y.

As expected, the imaginary component of the coefficients are dominant over the real component on both patches. On interface 2b the magnitude of the imaginary components are 100 to 10^4 times larger than those of the real components. On the patch of interface 3b, the imaginary components are 10 to 100 times larger than the real components.

Table 5-1 Surface Current Coefficients for the Patch of Interface 2b

X-DIRECTED CURRENT CELLS			
INDEX	COEFFICIENT	INDEX	COEFFICIENT
1	(0.144930D-05, 0.313567D-02)	24	(-.704937D-04, -.152963D-01)
2	(-.588259D-04, -.111001D-01)	25	(-.490389D-04, 0.550930D-02)
3	(-.277699D-04, 0.389851D-01)	26	(-.844589D-04, -.622061D-02)
4	(-.447774D-04, -.226170D-01)	27	(-.197880D-04, 0.243996D-01)
5	(-.390199D-04, 0.234268D-02)	28	(-.180006D-04, 0.733650D-02)
6	(-.447774D-04, -.226170D-01)	29	(-.788197D-04, 0.165448D-01)
7	(-.277699D-04, 0.389851D-01)	30	(-.448388D-04, -.886093D-02)
8	(-.588259D-04, -.111001D-01)	31	(-.655276D-04, -.583216D-02)
9	(0.144930D-05, 0.313567D-02)	32	(-.588050D-04, 0.156866D+00)
10	(-.180006D-04, 0.733650D-02)	33	(-.655276D-04, -.583216D-02)
11	(-.788197D-04, 0.165448D-01)	34	(-.448388D-04, -.886093D-02)
12	-.448388D-04, -.886093D-02)	35	(-.788197D-04, 0.165448D-01)
13	(-.655276D-04, -.583216D-02)	36	(-.180006D-04, 0.733650D-02)
14	(-.588050D-04, 0.156866D+00)	37	(0.144930D-05, 0.313567D-02)
15	(-.655276D-04, -.583216D-02)	38	(-.588259D-04, -.111001D-01)
16	(-.448388D-04, -.886093D-02)	39	(-.277699D-04, 0.389851D-01)
17	(-.788197D-04, 0.165448D-01)	40	(-.447774D-04, -.226170D-01)
18	(-.180006D-04, 0.733650D-02)	41	(-.390199D-04, 0.234268D-02)
19	(-.197880D-04, 0.243996D-01)	42	(-.447774D-04, -.226170D-01)
20	(-.844589D-04, -.622061D-02)	43	(-.277699D-04, 0.389851D-01)
21	(-.490389D-04, 0.550930D-02)	44	(-.588259D-04, -.111001D-01)
22	(-.704937D-04, -.152963D-01)	45	(0.144930D-05, 0.313567D-02)
23	(-.635182D-04, 0.410874D+00)		
Y-DIRECTED CURRENT CELLS			
1	(0.309850D-05, -.126455D-04)	21	(0.314528D-06, -.271924D-04)
2	(-.434617D-06, -.600874D-04)	22	(-.484581D-06, 0.302674D-03)
3	(-.276181D-05, -.872770D-04)	23	(0.650785D-06, 0.377249D-03)
4	(0.398818D-05, 0.101381D-04)	24	(-.155509D-06, -.774813D-04)
5	(-.292500D-06, -.674216D-04)	25	(0.152025D-06, -.136765D-04)
6	(-.186479D-05, -.365742D-04)	26	(-.630530D-07, 0.314760D-03)
7	(0.989116D-06, -.577124D-04)	27	(0.717857D-06, 0.389302D-03)
8	(-.143753D-05, -.688197D-04)	28	(-.174532D-06, -.195733D-04)
9	(-.893336D-07, -.306283D-04)	29	(0.119948D-06, 0.233631D-04)
10	(-.389707D-06, -.124038D-03)	30	(0.346488D-06, 0.174468D-03)
11	(-.346438D-06, -.174468D-03)	31	(0.389658D-06, 0.124038D-03)
12	(-.119989D-06, -.233631D-04)	32	(0.893715D-07, 0.306283D-04)
13	(0.174509D-06, 0.195733D-04)	33	(0.143755D-05, 0.688197D-04)
14	(-.717827D-06, -.389302D-03)	34	(-.989152D-06, 0.577124D-04)
15	(0.630119D-07, -.314760D-03)	35	(0.186483D-05, 0.365742D-04)
16	(-.151986D-06, 0.136765D-04)	36	(0.292481D-06, 0.674216D-04)
17	(0.155539D-06, 0.774813D-04)	37	(-.398819D-05, -.101381D-04)
18	(-.650930D-06, -.377249D-03)	38	(0.276182D-05, 0.872770D-04)
19	(0.484737D-06, -.302674D-03)	39	(0.434610D-06, 0.600874D-04)
20	(-.314572D-06, 0.271924D-04)	40	(-.309850D-05, 0.126455D-04)

Table 5-2 Surface Current Coefficients for the Patch of Interface 3b

X-DIRECTED CURRENT CELLS		Y-DIRECTED CURRENT CELLS	
INDEX	COEFFICIENT	INDEX	COEFFICIENT
1	(0.502501D-03,-.920439D-03)	24	(0.292374D-03,0.157864D-01)
2	(0.202992D-03,0.983445D-03)	25	(0.330107D-03,0.853381D-02)
3	(0.306094D-03,-.160172D-01)	26	(0.211369D-03,0.170281D-02)
4	(0.271213D-03,0.219468D-02)	27	(0.566711D-03,-.865155D-02)
5	(0.290519D-03,-.563160D-02)	28	(0.531274D-03,-.344992D-02)
6	(0.271213D-03,0.219468D-02)	29	(0.194061D-03,-.675561D-02)
7	(0.306094D-03,-.160172D-01)	30	(0.306734D-03,0.587638D-02)
8	(0.202992D-03,0.983445D-03)	31	(0.272054D-03,-.180131D-02)
9	(0.502501D-03,-.920439D-03)	32	(0.288759D-03,-.236412D-01)
10	(0.531274D-03,-.344992D-02)	33	(0.272054D-03,-.180131D-02)
11	(0.194061D-03,-.675561D-02)	34	(0.306734D-03,0.587638D-02)
12	(0.306734D-03,0.587638D-02)	35	(0.194061D-03,-.675561D-02)
13	(0.272054D-03,-.180131D-02)	36	(0.531274D-03,-.344992D-02)
14	(0.288759D-03,-.236412D-01)	37	(0.502501D-03,-.920439D-03)
15	(0.272054D-03,-.180131D-02)	38	(0.202992D-03,0.983445D-03)
16	(0.306734D-03,0.587638D-02)	39	(0.306094D-03,-.160172D-01)
17	(0.194061D-03,-.675561D-02)	40	(0.271213D-03,0.219468D-02)
18	(0.531274D-03,-.344992D-02)	41	(0.290519D-03,-.563160D-02)
19	(0.566711D-03,-.865155D-02)	42	(0.271213D-03,0.219468D-02)
20	(0.211369D-03,0.170281D-02)	43	(0.306094D-03,-.160172D-01)
21	(0.330107D-03,0.853381D-02)	44	(0.202992D-03,0.983445D-03)
22	(0.292374D-03,0.157864D-01)	45	(0.502501D-03,-.920439D-03)
23	(0.310082D-03,0.228847D-01)		
Y-DIRECTED CURRENT CELLS			
1	(0.288394D-04,0.480673D-03)	21	(-.195355D-05,-.177182D-03)
2	(-.484272D-05,0.450811D-04)	22	(0.521850D-07,-.201216D-02)
3	(-.116127D-04,-.158249D-03)	23	(0.141238D-05,-.216219D-02)
4	(0.315246D-04,0.555294D-03)	24	(-.248727D-05,-.360807D-03)
5	(0.157141D-04,0.599795D-03)	25	(-.581689D-05,-.101351D-02)
6	(-.805477D-05,-.232144D-05)	26	(0.106620D-05,-.151859D-02)
7	(-.125982D-05,-.456065D-04)	27	(0.312257D-05,-.107837D-02)
8	(0.128715D-04,0.646055D-03)	28	(-.661839D-05,-.106295D-02)
9	(0.107619D-04,0.886621D-03)	29	(-.102565D-04,-.979207D-03)
10	(-.400550D-05,0.173890D-03)	30	(0.274035D-05,-.178920D-03)
11	(-.274037D-05,0.178920D-03)	31	(0.400551D-05,-.173890D-03)
12	(0.102565D-04,0.979207D-03)	32	(-.107619D-04,-.886621D-03)
13	(0.661841D-05,0.106295D-02)	33	(-.128715D-04,-.646055D-03)
14	(-.312259D-05,0.107837D-02)	34	(0.125983D-05,0.456065D-04)
15	(-.106618D-05,0.151859D-02)	35	(0.805476D-05,0.232144D-05)
16	(0.581689D-05,0.101351D-02)	36	(-.157140D-04,-.599795D-03)
17	(0.248729D-05,0.360807D-03)	37	(-.315246D-04,-.555294D-03)
18	(-.141244D-05,0.216219D-02)	38	(0.116127D-04,0.158249D-03)
19	(-.521166D-07,0.201216D-02)	39	(0.484272D-05,-.450811D-04)
20	(0.195351D-05,0.177182D-03)	40	(-.288394D-04,-.480673D-03)

5.4 MoM Impedance Matrix Properties

Due to space limitations, the complete MoM impedance matrix cannot be included as part of this document, however the matrix elements were examined and this section reports some of the observed properties of the matrix.

As discussed in section 3.3.4, the MoM impedance matrix is expected to be diagonally dominant, and the matrix produced by the MoM software did show the dominance of the diagonal elements. Additionally, as is the case at resonance [20:428], the imaginary components of the elements were dominant over the real components. Also, the elements describing x-directed fields created by x-directed sources were at least one order of magnitude larger than the remaining elements - i.e those describing y-directed fields created by x-directed sources. This dominance manifests itself in the relatively large values of the coefficients for the x-directed cells as compared with the coefficients for the y-directed cells.

Each impedance sub-matrix is composed of four smaller impedance sub-sub-matrices arranged as shown

$$\begin{bmatrix} Z_{ij}^{b22} \end{bmatrix} = \begin{bmatrix} Z_{b22}^{xx} & Z_{b22}^{xy} \\ Z_{b22}^{yx} & Z_{b22}^{yy} \end{bmatrix} \quad (5-1)$$

where the first letter of the superscript is the observer orientation and the second is the source orientation. The number of rows in the sub-sub-matrix are determined by the number cells with the observer orientation and the number of columns is determined by the number of cells with the source orientation. For instance, consider antenna #1 with 45 x-current cells and 40 y-current cells on the patch of interface 2b. Therefore, the sub-sub-matrix with superscript xy will have the dimension 45×40 .

A study of the first 45×45 block of the impedance matrix, representing the elements describing x-directed fields created by x-directed sources on interface 2b, also shows several useful symmetry characteristics. First, the entire 45×45 block consists of five, basic 9×9 sub-sub-matrices rearranged in a simple pattern. There are five basic sub-sub-matrices because there are five rows of x-directed cells on the patch. The dimension of each basic sub-sub-matrix is equal to the number of x-directed current cells on the patch. If the elements in rows 1 through 9 and columns 1 through 9 are designated as sub-sub-matrix z_{11} , and the elements in rows 1 through 9 and columns 10 through 18 are designated as z_{12} , and so forth so that the last sub-sub-matrix comprised by elements in rows 1 through 9 and columns 37 through 45 is designated z_{15} , the remaining twenty 9×9 blocks of the 45×45 block can be filled according to the formula

$$z_{m,n} = z_{1,|m-n|} \quad (5-2)$$

where

m = the row index for the sub-sub-matrix

n = the column for the sub-sub-matrix

This pattern is the same as that of the toeplitz MoM impedance matrix for a wire-scatterer, except 9 x 9 sub-sub-matrices are rearranged instead of individual matrix elements. Each 9 x 9 sub-sub-matrix is toeplitz, and the element arrangement pattern is given by equation (5-2) with the z's being the individual matrix elements in the sub-sub-matrix.

Since the symmetry of the matrix elements is due to the fact that the Green's functions are dependent only upon the argument kR , it is sensible to believe the three remaining sub-sub-matrices of Z^{b22} are symmetric and toeplitz. This symmetry is important because it can be used to reduce the computer processor time needed to fill the MoM impedance matrix. For instance, with the symmetry explained for the first 45 x 45 matrix, the block could be filled by first calculating and then rearranging the 45 elements of the first row. Based on this observation, it is sensible to expect that the complete MoM matrix can be filled by calculating only four rows from the matrix. Calculating the first row would provide the elements needed to fill the sub-sub-matrices for x-directed fields on interface 2b that are created by sources on both patches. Calculating the row with an index of $(N_{2x} + 1)$ would provide the elements needed to fill the sub-sub-matrices describing y-directed fields on interface 2b created by sources on both

patches. Data for the row with index $(N_2 + 1)$ would provide the elements needed to fill the sub-sub-matrices describing x-directed fields on interface 3b created by sources on both patches. Finally, elements with a row index equal to $(N_2 + N_{3x} + 1)$ can be used to fill the sub-sub-matrices describing the y-directed fields on interface 3b created by the sources on both patches.

Modifying the MoM solution software to exploit the toeplitz nature and symmetry of the impedance matrix would be very easy to do and would save considerable computer processor time. While the exact savings is hard to guess without performing the modifications and running the software, estimates can be made. For instance, consider the solution for antenna #1 which has a 170×170 impedance matrix or 28,900 impedance elements. Calculating only four rows of the impedance matrix would require finding only 680 elements. Since each element calculation involves the execution of a three-layer, nested do-loop, - one loop for the line integration and two for the surface integration - it is reasonable to believe most of the processor time for the program is dedicated to filling the impedance matrix. Since reducing the number of element calculations from 28,900 to 680 is a 97% reduction, a similar reduction in the processor time should be obtained.

VI. Recommendations and Conclusions

This chapter contains conclusions about the accuracy of the MoM solution developed in this effort and recommendations for improving the MoM software's flexibility and capabilities.

6.1 Conclusions

Based on data presented in Chapter V, the data obtained from the MoM solution software is correct, as best as can be told at this point. As discussed in Section 5.2.1, the data from the MoM software predicts the antennas are near resonance at 3.7 GHz, and this result matches measurements. The solution predicts the strongest currents occur in the center of the patches which is expected since both patches are aligned directly over the aperture of the antenna. Also, The MoM solution predicts a dominance of the x-directed surface currents over the y-directed currents, and this result is expected since the magnetic surface currents of the aperture are in the y-direction only.

Unfortunately, at the present time the ability to derive impedance information and field patterns using data from the MoM software has not been developed. Since this data is the standard by which solution accuracy is judged, the final measure of the accuracy of the data from MoM software cannot be made.

6.2 Expanding the MoM Software

Microstrip antenna analysis software is most commonly used for predicting the antenna impedance and radiation characteristics. At present, the MoM solution software is not capable of providing data for either predictions. This section outlines the modifications and additions that could be made to use the MoM software for impedance and field pattern predictions.

6.1.1 Incorporating a Feed System Model. Before any antenna impedance data can be calculated, the MoM software must have access to data describing the feed system operation. With this data, the complete antenna model of Sections 3.2 and 3.3 can be completed, thus providing a means to completely calculate the scattered and excitation fields on the feedline. Once the excitation and scattered fields are known, the input impedance can be calculated from the relationship [20:428]

$$Z_{in} = -\frac{1}{I} \int_0^h (\underline{E}^{(s)} + \underline{E}^{(e)}) \cdot \hat{z} dz \quad (6-1)$$

where

I = the input current

h = the distance between the ground plane and the feedline

$\underline{E}^{(s)}$ = the scattered fields on the feedline

$\underline{E}^{(e)}$ = the excitation fields on the feedline

Once input impedance can be calculated, VSWR and other performance data can be obtained. Additionally, the MoM impedance matrix can be analyzed to obtain data on resonant frequencies of the antenna.

It should also be noted that the completion of the MoM solution for the full model would require only minor modifications to the MoM software, however the computer memory and processor time requirements would increase appreciably.

6.1.2 Calculations for Bandwidth Characteristics. Calculating the antenna characteristics over a bandwidth requires the ability to evaluate the Green's functions for various frequencies. There are several ways this capability might be incorporated into the MoM software.

The simplest option would require creating Green's function polynomial coefficient files for selected sampling frequencies over the bandwidth of interest. As the frequency of the excitation is varied, the MoM software would read the polynomial coefficients for the present

frequency, and then complete the MoM solution for the frequency.

However, incorporating this option would require all Green's functions polynomials to have the same general form for all frequencies of interest which is probably not the case.

Other ways to enable bandwidth studies are using Green's functions polynomials that are a function of both R and frequency, incorporating the Green's functions evaluation code into the MoM software, or implementing an interpolation procedure using tabulated data.

These three options would all result in increased processor time for the MoM solution. Using frequency dependent polynomial coefficient data is the most efficient means in terms of computer memory. Using an interpolation scheme would significantly increase memory requirements due to storage for the tabulated Green's function data. Incorporating the code to calculate the Green's functions would produce the most accurate results, but the accuracy improvement would most likely be offset by an enormous increase in computation time. However, the additional computer time would be almost identical to the time needed to produce the data needed for interpolation tables or to produce polynomial approximations.

6.1.3 Modifications for Field Pattern Calculations. Calculating the field patterns of the antenna could easily be incorporated into the MoM solution software. The major obstacle to this capability is obtaining the closed form expressions for the gradient of the G_q Green's functions. Without these expressions, the fields created by the surface

charge distributions cannot be evaluated numerically, and therefore the fields on the antenna interfaces cannot be calculated.

With the gradient of the G_q functions known, a subroutine to establish the observer location and calculate the contributions from the aperture and patches of the antenna would need to be written. The functions performed by the field calculation subroutine would be exactly like those performed by subroutine EVALSUB, with the exception that the integration along the observer test segment would not be performed. Once the fields of the antenna interface can be calculated, the software to complete the calculations of the aperture model as explained in Section 3.7 would need to be written and incorporated into the MoM solution software. With these additions, the field patterns of the antenna could be calculated.

6.3 *Improving Computation Efficiency*

As mentioned in Section 5.4, the 3-plane MoM impedance matrix is toeplitz and symmetrical. While the symmetry is complex, the reduction in the number of impedance elements obtained by taking advantage of the symmetry and toeplitz nature of the matrix would make the study of the symmetry worthwhile.

Appendix A. Green's Functions Sommerfeld Integrals and Polynomial Approximations

This appendix lists the Sommerfeld integrals, as derived by Nazar, that define the Green's functions for the aperture-fed, stacked patch antenna. For the case when the observer and source plane coincide, the asymptotic representation of the integral for $R \rightarrow 0$ is also given. These integrals are taken directly from Nazar's thesis [23:112-122]. Additionally, the coefficients for the Green's function polynomial models, as derived by Erwert and used in the MoM solution, are tabulated.

A.1 Definitions of Constants and Variables and Polynomial Model Forms

In all of the Sommerfeld integrals the path of integration C is along the real axis in the complex λ -plane, except for deformations around any integrand singularities. The deformations around the poles must be made in the half-plane such that $\text{Im}(\lambda) > 0$ [21:50]. Following are the definitions of the constants used in the Green's function Sommerfeld integrals.

μ_{1b} , μ_{2b} , μ_{3b} - the permeability of the dielectric between interface 1b and 2b, interface 2b and 3b, and above interface 3b, respectively; μ_{3b} is actually μ_0

μ_{b23} - the ratio μ_{2b}/μ_{3b} , all other subscripted μ with two numbers in the subscript are defined in the same way

b_{1b} , b_{2b} - the distance between interfaces 1b and 2b, and interfaces 2b and 3b, respectively

$H_0^{(2)}(\lambda R)$ - the Hankel function of the second kind of order 0 with argument λR

Other variables in the integrals are defined as follows:

$$R = |\rho - \rho'|$$

$$\varsigma = \sin^{-1} \left[\frac{\rho \sin \varphi - \rho' \sin \varphi'}{R} \right]$$

$$u_{1b, 2b, 3b} = \sqrt{\lambda^2 - k_{1b, 2b, 3b}^2}$$

$$k_{1b, 2b, 3b} = \omega \sqrt{\epsilon_{1b, 2b, 3b} \mu_{1b, 2b, 3b}} \quad (A-1)$$

$$D_e^b(\lambda) = \left\{ \begin{array}{l} [\mu_{b13} u_{3b} + u_{1b} \coth(b_{1b} u_{1b})] u_{2b} \cosh[u_{2b}(b_{2b} - b_{1b})] + \\ \{\mu_{b12} u_{2b}^2 + \mu_{b23} u_{1b} u_{3b} \coth[b_{1b} u_{1b}]\} \sinh[u_{2b}(b_{2b} - b_{1b})] \end{array} \right\}$$

$$D_m^b(\lambda) = \left\{ \begin{array}{l} [\epsilon_{b13} u_{3b} + u_{1b} \tanh(b_{1b} u_{1b})] u_{2b} \cosh[u_{2b}(b_{2b} - b_{1b})] + \\ [\epsilon_{b12} u_{2b}^2 + \epsilon_{b23} u_{1b} u_{3b} \tanh(b_{1b} u_{1b})] \sinh[u_{2b}(b_{2b} - b_{1b})] \end{array} \right\}$$

The polynomial models for the Green's functions consists of separate models for the real and imaginary components. For the G_A

Green's functions and the I^r , I^s , and I^t components of the G_E Green's functions, the real component is represented by an eighth order polynomial for $0.001 < R < 0.01$. When $R > 0.01$, the real component is modeled as follows:

$$\text{Imag}(f(R)) = \frac{c_0}{R^2} + \frac{c_1}{R} + c_2 + c_3 R + c_4 R^2 + c_5 R^3 + \\ c_6 R^4 + c_7 R^5 + c_8 R^6 + c_9 R^7 + c_{10} R^8 \quad (\text{A-2})$$

where the function $f(R)$ is either one of the G_A functions or one of the components of the G_E functions.

The imaginary components of the G_A functions and the components of the G_E functions are represented by a sixth order polynomial valid for all values of R .

The real components of the G_q functions are modeled by a sixth order polynomial valid for all R . The imaginary components are modeled by an eighth order polynomial for $0.001 < R < 0.01$, and by a polynomial as given in equation (A-2) for values of $R > 0.01$.

The coefficients for each polynomial model are tabulated along with the Sommerfeld integral defining the Green's functions. In the cases where a component of the function is represented by two different polynomials, the coefficients listed under the column heading "Real #1," for example, would indicate the coefficients for the polynomial model when $R \in [0.001, 0.001]$ and the column heading "Real #2" would indicate the coefficients for the polynomial model when $R > 0.001$.

A.2 Green's Functions Describing Fields Generated by Sources on Interface 1b.

A.2.1 Green's Functions for Fields on Interface 2b.

$$\begin{aligned}
 G_{E21}^{bxz}(R, \xi) &= -\sin(2\xi) \left[\frac{1}{2} I_{b21}^x(R) - I_{b21}^s(R) \right] \\
 G_{E21}^{byz}(R, \xi) &= - \left[-I_{b21}^t(R) - \cos^2(\xi) I_{b21}^x(R) + \cos(2\xi) I_{b21}^s(R) \right] \\
 G_{E21}^{bxy}(R, \xi) &= \left[-I_{b21}^t(R) + \sin^2(\xi) I_{b21}^x(R) + \cos(2\xi) I_{b21}^s(R) \right] \\
 G_{E21}^{bzy}(R, \xi) &= -\sin(2\xi) \left[-\frac{1}{2} I_{b21}^x(R) + I_{b21}^s(R) \right]
 \end{aligned} \tag{A-3}$$

where

$$\begin{aligned}
 I_{b21}^x(R) &= \int_C \frac{H_0^{(2)}(\lambda R) \operatorname{sech}(b_{1b} u_{1a}) \lambda^3}{D_b^b(\lambda) D_m^b(\lambda)} \Gamma_2(\lambda) d\lambda \\
 I_{b21}^s(R) &= \int_C \frac{H_1^{(2)}(\lambda R) \operatorname{sech}(b_{1b} u_{1a}) \lambda^2}{RD_b^b(\lambda) D_m^b(\lambda)} \Gamma_2(\lambda) d\lambda \\
 I_{b21}^t(R) &= \int_C \frac{H_0^{(2)}(\lambda R) \operatorname{sech}(b_{1b} u_{1a}) \lambda}{D_m^b(\lambda)} \left[\begin{array}{l} \epsilon_{b13} u_{3b} \cosh(u_{2b}(b_{2b} - b_{1b})) \\ + \epsilon_{b12} u_{2b} \sinh(u_{2b}(b_{2b} - b_{1b})) \end{array} \right] d\lambda
 \end{aligned} \tag{A-4}$$

and

$$\begin{aligned}
 \Gamma_2(\lambda) &= (1 - \mu_{b13} \epsilon_{b13}) u_{2b}^2 \\
 &+ \left[\begin{array}{l} (\lambda - \mu_{b13} \epsilon_{b13}) u_{2b}^2 \\ + (-\mu_{b13} \epsilon_{b13} + \mu_{b23} \epsilon_{b23}) u_{3b}^2 \end{array} \right] \sinh^2[u_{2b}(b_{2b} - b_{1b})] \\
 &+ \frac{\mu_{2b} \mu_{3b}}{2} \left[\begin{array}{l} \mu_{b23} - \mu_{b13} \epsilon_{b12} \\ - \mu_{b12} \epsilon_{b13} + \epsilon_{b23} \end{array} \right] \frac{u_{2b} u_{3b}}{2} \sinh[2u_{2b}(b_{2b} - b_{1b})]
 \end{aligned} \tag{A-5}$$

Table A-1 Coefficients for I^r_{b21} Polynomial Model

Coefficient #	Real #1	Real #2	Imaginary
0	-2.3690010E+04	-2.7567323E-01	7.3622798E+02
1	-5.1497773E+03	4.1969248E+01	1.6413327E+02
2	2.0098000E+09	-1.7263071E+03	-9.4660002E+05
3	1.1664054E+11	6.7013484E-04	-5.5624401E+06
4	-2.4628222E+14	2.5393666E+06	6.6599743E+08
5	6.0581647E+16	-1.0559782E+00	-8.2057805E+09
6	-6.9634200E+18	-3.8054523E+09	2.9878758E+10
7	4.0033536E+20	1.0860188E+11	-
8	-9.2918335E+21	-1.3359528E+12	-
9	-	7.9367587E+12	-
10	-	-1.8720567E+13	-

Table A-2 Coefficients for I^s_{b21} Polynomial Model

Coefficient #	Real #1	Real #2	Imaginary
0	-1.1845706E+04	-1.4338001E-01	3.6839408E+02
1	-1.1244172E+03	-8.8320753E+00	-1.0565021E+02
2	4.8720618E+08	4.8974870E+02	-2.1992704E+05
3	3.5107918E+10	-1.9777346E-04	-1.7804531E+06
4	-4.5628645E+13	-1.6920208E+05	1.2335704E+08
5	9.6364022E+15	3.2111913E-01	-1.2791397E+09
6	-9.8801478E+17	2.6480174E+08	4.0846293E+09
7	5.1850820E+19	-9.6649951E+09	-
8	-1.1172704E+20	1.4729755E+11	-
9	-	-1.0371150E+12	-
10	-	2.7871008E+12	-

Table A-3 Coefficients for I_{b21}^t Polynomial Model

Coefficient #	Real #1	Real #2	Imaginary
0	8.3730489E+05	1.0488087E+00	-1.2618585E+03
1	1.8548911E+07	-9.7803738E+01	-1.1645510E+01
2	-6.9596640E+11	3.8139458E+03	1.2324177E+06
3	4.9585244E+14	-1.1916493E-03	7.8552878E+06
4	-1.6509095E+17	-4.5203333E+06	-8.1658149E+08
5	3.0643030E+19	1.8826109E+00	9.7146319E+09
6	-3.2457653E+21	6.2316114E+09	-3.4550352E+10
7	1.8334913E+23	-1.7672322E+11	-
8	-4.2836938E+24	2.1844777E+12	-
9	-	-1.3111428E+13	-
10	-	3.1297587E+13	-

A.2.2 Green's Function for Fields on Interface 3b.

$$\begin{aligned}
 G_{E31}^{bxz}(R, \xi) &= -\sin(2\xi) \left[\frac{1}{2} I_{b31}^x(R) - I_{b31}^s(R) \right] \\
 G_{E31}^{byz}(R, \xi) &= - \left[-I_{b31}^t(R) - \cos^2(\xi) I_{b31}^x(R) + \cos(2\xi) I_{b31}^s(R) \right] \quad (A-6) \\
 G_{E31}^{bxy}(R, \xi) &= \left[-I_{b31}^t(R) + \sin^2(\xi) I_{b31}^x(R) + \cos(2\xi) I_{b31}^s(R) \right] \\
 G_{E31}^{byy}(R, \xi) &= -\sin(2\xi) \left[-\frac{1}{2} I_{b31}^x(R) + I_{b31}^s(R) \right]
 \end{aligned}$$

where

$$\begin{aligned}
 I_{b31}^x(R) &= \int_C \frac{H_0^{(2)}(\lambda R) \lambda^3}{D_e^b(\lambda) D_m^b(\lambda)} \Gamma_3(\lambda) d\lambda \\
 I_{b31}^s(R) &= \int_C \frac{H_1^{(2)}(\lambda R) \lambda^2}{RD_e^b(\lambda) D_m^b(\lambda)} \Gamma_3(\lambda) d\lambda \quad (A-7) \\
 I_{b31}^t(R) &= \int_C \frac{H_0^{(2)}(\lambda R) \lambda u_{2b}}{D_m^b(\lambda)} [\epsilon_{b13} u_{3b} \operatorname{sech}(u_{1b} b_{1b})] d\lambda
 \end{aligned}$$

and

$$\begin{aligned}
 \Gamma_3(\lambda) &= (1 - \mu_{b13} \epsilon_{b13}) u_{2b}^2 \operatorname{sech}(b_{1b} u_{1b}) \cosh[u_{2b}(b_{2b} - b_{1b})] \\
 &+ \left[(\epsilon_{b12} - \mu_{b23} \epsilon_{b13}) u_{1b} u_{2b} \operatorname{csch}(b_{1b} u_{1b}) \right. \\
 &\quad \left. + (-\mu_{b12} \epsilon_{b13} + \epsilon_{b23}) u_{2b} u_{3b} \operatorname{sech}(b_{1b} u_{1b}) \right] \sinh[u_{2b}(b_{2b} - b_{1b})] \quad (A-8)
 \end{aligned}$$

Table A-4 Coefficients for I^s_{b31} Polynomial Model

Coefficient #	Real #1	Real #2	Imaginary
0	-7.1631702E+04	-3.9145822E-01	1.4578382E+03
1	-1.6126649E+06	6.0771449E+01	3.2605113E+02
2	1.6138582E+10	-2.4640424E+03	-1.8752160E+06
3	-4.6090776E+12	1.0734826E-03	-1.1014941E+07
4	2.0514025E+14	4.2372332E+06	1.3194275E+09
5	1.1322934E+17	-1.6926680E+00	-1.6258111E+10
6	-2.2354787E+19	-6.5280178E+09	5.9202168E+10
7	1.6596165E+21	1.8569636E+11	-
8	-4.5322535E+22	-2.2676061E+12	-
9	-	1.3351982E+13	-
10	-	-3.1213003E+13	-

Table A-5 Coefficients for I^s_{b31} Polynomial Model

Coefficient #	Real #1	Real #2	Imaginary
0	-3.5845677E+04	-3.2220387E-01	7.2947448E+02
1	-1.8303401E+05	-1.1195931E+01	-2.0927389E+02
2	3.3506986E+09	6.7963919E+02	-4.3564658E+05
3	-4.0133292E+11	-2.7539833E-04	-3.5273908E+06
4	-1.6475295E+14	-7.0817217E+04	2.4440619E+08
5	5.8048203E+16	4.4877070E-01	-2.5345126E+09
6	-7.7186016E+18	1.6953818E+08	8.0937999E+09
7	4.8748677E+20	-8.6162929E+09	-
8	-1.2131994E+22	1.5436197E+11	-
9	-	-1.1848456E+12	-
10	-	3.3469197E+12	-

Table A-6 Coefficients for I^t_{b31} Polynomial Model

Coefficient #	Real #1	Real #2	Imaginary
0	2.8114574E+05	1.5538455E+00	-2.4949310E+03
1	5.9078765E+06	-1.2252199E+02	-2.4719206E+01
2	-5.9241731E+10	4.5582187E+03	2.4398514E+06
3	1.6899417E+13	-1.4436500E-03	1.5547730E+07
4	-7.7355313E+14	-6.4603264E+06	-1.6171597E+09
5	-4.0848676E+17	2.2647814E+00	1.9242115E+10
6	8.1118069E+19	9.1346088E+09	-6.8442981E+10
7	-6.0339466E+21	-2.5611943E+11	-
8	1.6495873E+23	3.1131480E+12	-
9	-	-1.8348861E+13	-
10	-	4.3053899E+13	-

A.3 Green's Functions Describing Fields Generated by Sources on Interface 2b.

A.3.1 Green's Functions for Fields on Interface 2b.

$$G_{A22}^{bxz}(R) = \frac{\mu_{1b}}{4\pi} \int_c \frac{H_0^{(2)}(\lambda R) \lambda}{D_s^b(\lambda)} \left[\begin{array}{l} u_{2b} \cosh[u_{2b}(b_{2b} - b_{1b})] \\ + \mu_{b23} u_{3b} \sinh[u_{2b}(b_{2b} - b_{1b})] \end{array} \right] d\lambda$$

$$G_{A22}^{byy}(R) = G_{A22}^{bxz}(R) \quad (A-9)$$

$$G_{q22}^b = \frac{1}{4\pi \epsilon_{2b}} \int_c \frac{H_0^{(2)}(\lambda R) \lambda}{D_s^b(\lambda) D_m^b(\lambda)} \Gamma_{q22} d\lambda$$

where

$$\Gamma_{q22} = \epsilon_{b23} u_{2b}^2 u_{3b} \cosh^2(u_{2b}(b_{2b} - b_{1b}))$$

$$+ \left\{ \mu_{b23} u_{2b}^2 u_{3b} + \left[\begin{array}{l} (\mu_{b12} u_{2b}^2 + \mu_{b13} \epsilon_{b23} u_{3b}^2) \\ * u_{1b} \tanh(b_{1b} u_{1b}) \end{array} \right] \right\} \sinh^2(u_{2b}(b_{2b} - b_{1b}))$$

$$+ \left\{ \begin{array}{l} u_{2b}^2 + \mu_{b23} \epsilon_{b23} u_{3b}^2 + \\ [\mu_{b13} + \mu_{b12} \epsilon_{b23}] u_{1b} u_{3b} \tanh(b_{1b} u_{1b}) \end{array} \right\} \frac{u_{2b}}{2} \sinh[2u_{2b}(b_{2b} - b_{1b})]$$

$$+ \mu_{b13} \epsilon_{b23} u_{1b} u_{2b}^2 \tanh(b_{1b} u_{1b}) \quad (A-10)$$

A.3.1.1 Asymptotic Forms for $R \rightarrow 0$.

$$G_{A22}^{bxz}(R) = \frac{\mu_{1b}}{2\pi} \left\{ \int_0^{\lambda_c} I_{A22}^b(R, \lambda) d\lambda - r_{A2} \int_0^{R\lambda_c} \frac{J_0(x)}{R} dx + \frac{r_{A2}}{R} \right\} \quad (A-11)$$

where

$$\tau_{A2} = \frac{1 + \mu_{b23}}{1 + \mu_{b12} + \mu_{b23} + \mu_{b13}} \quad (A-12)$$

$$G_{q22}^b(R) = \frac{1}{j\omega^2 \pi \epsilon_{2b}} \left\{ \int_0^{\lambda_c} I_{q22}^b(R, \lambda) d\lambda - \tau_{q2} \int_0^{R\lambda_c} \frac{J_0(x)}{R} dx + \frac{\tau_{q2}}{R} \right\} \quad (A-13)$$

where

$$\tau_{q2} = \frac{1 + \epsilon_{b23}}{1 + \epsilon_{b12} + \epsilon_{b23} + \epsilon_{b13}} \quad (A-14)$$

and the integrals $I_{A22}^b(\lambda R)$ and $I_{q22}^b(\lambda R)$ are the integrands of the original Sommerfeld integrals with $H_0^{(2)}(\lambda R)$ replaced by $J_0(\lambda R)$.

Table A-7 Coefficients for G_{A22}^b Polynomial Model

Coefficient #	Real #1	Real #2	Imaginary
0	2.8271357E-04	1.1336337E-10	-8.2697879E-08
1	-3.9846556E-01	-7.7506745E-0	3.0039534E-08
2	2.7285907E+02	2.8775042E-07	4.4481533E-05
3	-1.0962870E+05	-7.9761966E-14	3.7821366E-04
4	-4.2391776E+09	-2.8113896E-04	-2.3998044E-02
5	3.9943857E+11	1.2917902E-10	2.3993749E-01
6	-2.0833405E+13	3.4524106E-01	-7.4304513E-01
7	2.7278577E+07	-9.6808158E+00	-
8	4.6074276E+14	1.2043431E+02	-
9	-	-7.3386638E+02	-
10	-	1.7830531E+03	-

Table A-8 Coefficients for G_{q22}^b Polynomial Model

Coefficient #	Real	Imaginary #1	Imaginary #2
0	2.4690865E-01	-5.0295804E+02	-3.0506451E-04
1	8.1564715E-02	6.9944277E+05	3.7573808E-02
2	-3.1310965E+02	-4.7773874E+08	-1.5014618E+00
3	-1.7501311E+03	1.9210580E+11	3.1525211E-07
4	2.1602490E+05	-4.7861591E+13	7.9630909E+02
5	-2.6605711E+06	7.4454262E+15	-5.0947594E-04
6	9.6760956E+06	-7.0205947E+17	-7.9604799E+05
7	-	3.6635682E+19	2.3725931E+07
8	-	-8.1050716E+20	-3.2364262E+08
9	-	-	2.1545771E+09
10	-	-	-5.6293092E+09

A.3.2 Green's Functions for Fields on Interface 3b.

$$\begin{aligned}
 G_{A32}^{bxx}(R) &= \frac{\mu_{1b}}{4\pi} \int_C H_0^{(2)}(\lambda R) \frac{\lambda u_{2b}}{D_b^b(\lambda)} d\lambda \\
 G_{A32}^{byy}(R) &= G_{A32}^{bxx}(R) \\
 G_{q32}^b(R) &= \frac{1}{4\pi \epsilon_{2b}} \int_C \frac{H_0^{(2)}(\lambda R) \lambda u_{2b}}{D_b^b(\lambda) D_m^b(\lambda)} \Gamma_{q32} d\lambda
 \end{aligned} \tag{A-15}$$

where

$$\begin{aligned}
 \Gamma_{q32} = & [u_{3b} + \mu_{b13} u_{1b} \tanh(b_{1b} u_{1b})] u_{2b} \cosh[u_{2b} (b_{2b} - b_{1b})] \\
 & + \left\{ \begin{array}{l} \mu_{b13} \epsilon_{b12} u_{2b}^2 + [u_{3b}^2 (\mu_{b23} - \mu_{b13} \epsilon_{b12})] \\ + \mu_{b12} u_{1b} u_{3b} \tanh(b_{1b} u_{1b}) \end{array} \right\} \sinh[u_{2b} (b_{2b} - b_{1b})]
 \end{aligned} \tag{A-16}$$

Table A-9 Coefficients for G_{A32}^b Polynomial Model

Coefficient #	Real #1	Real #2	Imaginary
0	4.3605698E-05	1.7029449E-10	-1.6312406E-07
1	1.6428591E-03	-8.1399245E-09	4.7418351E-08
2	-1.9408505E+01	2.6622157E-07	8.8848203E-05
3	1.0921513E+04	-4.1338561E-14	7.1341936E-04
4	-3.0476872E+06	-2.9963275E-04	-4.6862616E-02
5	4.9365870E+08	6.3114878E-11	4.6971581E-01
6	-4.6983776E+10	3.4697986E-01	-1.4547107E+00
7	2.4369181E+12	-9.2439916E+00	-
8	-5.3137854E+13	1.0942193E+02	-
9	-	-6.3847649E+02	-
10	-	1.4970486E+03	-

Table A-10 Coefficients for G_{q32}^b Polynomial Model

Coefficient #	Real	Imaginary #1	Imaginary #2
0	4.8908078E-01	-1.0079854E+02	-4.6056133E-04
1	9.7940015E-02	-3.9690570E+03	5.4394079E-02
2	-6.1506941E+02	4.6810550E+07	-2.1168582E+00
3	-3.6456986E+03	-2.6387382E+10	2.8577567E-07
4	4.3101735E+05	7.3656913E+12	8.4397927E+02
5	-5.2961144E+06	-1.1930563E+15	-4.4687389E-04
6	1.9249510E+07	1.1354126E+17	-6.1246793E+05
7	-	-5.8887562E+18	1.8533381E+07
8	-	1.2840182E+20	-2.7071295E+08
9	-	-	1.9286742E+09
10	-	-	-5.3094692E+09

A.4 Green's Functions Describing Fields Generated by Sources on Interface 3b

A.4.1 Green's Functions for Fields on Interface 2b.

$$G_{A23}^{bxx}(R) = G_{A23}^{byy}(R) = G_{A32}^{bxz}(R)$$

$$G_{q23}^b(R) = \frac{1}{4\pi\epsilon_{2b}} \int_C \frac{H_0^{(2)}(\lambda R) \lambda u_{2b}}{D_s^b(\lambda) D_m^b(\lambda)} \Gamma_{q23} d\lambda \quad (A-17)$$

where

$$\Gamma_{q23} = [u_{3b} + \mu_{b13} u_{1b} \tanh(b_{1b} u_{1b})] \epsilon_{b23} u_{2b} \cosh[u_{2b}(b_{2b} - b_{1b})]$$

$$+ \left\{ \begin{array}{l} u_{1b}^2 [-1 + \mu_{b23} \epsilon_{b23}] + u_{2b}^2 \\ + \mu_{b12} \epsilon_{b23} u_{1b} u_{3b} \tanh(b_{1b} b_{2b}) \end{array} \right\} \sinh[u_{2b}(b_{2b} - b_{1b})] \quad (A-18)$$

$$G_{q32}^b(R) = G_{q23}^b(R) \quad (A-19)$$

The coefficients for $G_{A32}^b(R)$ are the same as those listed in Table A-9.

The coefficients for $G_{q32}^b(R)$ are the same as those listed in Table A-10.

A.4.2 Green's Functions for Fields on Interface 3b.

$$G_{A33}^{bxx}(R) = \frac{\mu_{2b}}{4\pi} \int_C \frac{H_0^{(2)}(\lambda R) \lambda}{D_b^b(\lambda)} \Gamma_{A33} d\lambda$$

$$G_{A33}^{byy}(R) = G_{A33}^{bxx}(R) \quad (A-20)$$

$$G_{q33}^b(R) = \frac{1}{4\pi \epsilon_{3b}} \int_C \frac{H_0^{(2)}(\lambda R) \lambda}{D_b^b(\lambda) D_m^b(\lambda)} \Gamma_{q33} d\lambda$$

where

$$\Gamma_{A33} = \mu_{b12} u_{2b} \cosh[u_{2b}(b_{2b} - b_{1b})] + u_{1b} \coth(b_{1b} u_{1b}) \sinh[u_{2b}(b_{2b} - b_{1b})]$$

$$\Gamma_{q33} = \left\{ u_{3b} + \cosh^2[u_{2b}(b_{2b} - b_{1b})] \mu_{b13} u_{1b} \tanh(b_{1b} u_{1b}) \right\} u_{2b}^2$$

$$+ \left\{ \begin{aligned} & \left(u_{1b}^2 + \mu_{b12} \epsilon_{b12} u_{2b}^2 \right) u_{3b} \\ & + \mu_{b23} \epsilon_{b12} u_{1b} u_{2b}^2 \coth(b_{1b} u_{1b}) \end{aligned} \right\} \sinh^2[u_{2b}(b_{2b} - b_{1b})] \quad (A-21)$$

$$+ \left\{ \begin{aligned} & \mu_{b23} u_{1b}^2 + \mu_{b13} \epsilon_{b12} u_{2b}^2 \\ & + \left\{ \begin{aligned} & \epsilon_{b12} \coth(b_{1b} u_{1b}) \\ & + \mu_{b12} \tanh(b_{1b} u_{1b}) \end{aligned} \right\} u_{1b} u_{3b} \end{aligned} \right\} \frac{u_{2b}}{2} \sinh[2u_{2b}(b_{2b} - b_{1b})]$$

A.4.2.1 Asymptotic Forms for $R \rightarrow 0$.

$$G_{A22}^{bx}(R) = \frac{\mu_{2b}}{2\pi} \left\{ \int_0^{\lambda_c} I_{A33}^b(R, \lambda) d\lambda - r_{A3} \int_0^{R\lambda_c} \frac{J_0(x)}{R} dx + \frac{r_{A3}}{R} \right\} \quad (A-22)$$

where

$$r_{A3} = \frac{1 + \mu_{b12}}{1 + \mu_{b12} + \mu_{b23} + \mu_{b13}} \quad (A-23)$$

$$G_{q33}^b(R) = \frac{1}{j\omega 2\pi \epsilon_{3b}} \left\{ \int_0^{\lambda_c} I_{q33}^b(R, \lambda) d\lambda - r_{q3} \int_0^{R\lambda_c} \frac{J_0(x)}{R} dx + \frac{r_{q3}}{R} \right\} \quad (A-24)$$

where

$$r_{q3} = \frac{1 + \epsilon_{b12}}{1 + \epsilon_{b12} + \epsilon_{b23} + \epsilon_{b13}} \quad (A-25)$$

and the integrals $I_{A33}^b(\lambda R)$ and $I_{q33}^b(\lambda R)$ are the integrands of the original Sommerfeld integrals with $H_0^{(2)}(\lambda R)$ replaced by $J_0(\lambda R)$.

Table A-11 Coefficients for G_{A33}^b Polynomial Model

Coefficient #	Real	Imaginary #1	Imaginary #2
0	2.9895392E-04	2.6798747E-10	-3.2193755E-07
1	-3.9713808E-01	-7.5940224E-09	1.1728108E-07
2	2.7003667E+02	1.8608318E-07	1.7359691E-04
3	-1.0882422E+05	1.5038343E-14	1.4780323E-03
4	-4.2349631E+09	-3.2242885E-04	-9.3812439E-02
5	3.9979300E+11	-3.1416726E-11	9.3841354E-01
6	-2.0878692E+13	3.4534456E-01	-2.9073252E+00
7	2.7177121E+07	-8.3578282E+00	-
8	4.6215527E+14	8.8658536E+01	-
9	-	-4.6285555E+02	-
10	-	9.7745550E+02	-

Table A-12 Coefficients for G_{q33}^b Polynomial Model

Coefficient #	Real	Imaginary #1	Imaginary #2
0	9.6785892E-01	-7.1240104E+02	-7.3279954E-04
1	3.2169259E-01	9.5940154E+05	8.4236082E-02
2	-1.2286658E+03	-6.5262043E+08	-3.2371602E+00
3	-6.8608196E+03	2.6293123E+11	3.4357684E-07
4	8.4780207E+05	-6.5657068E+13	9.1330452E+02
5	-1.0443582E+07	1.0231241E+16	-5.4107447E-04
6	3.7986523E+07	-9.6588315E+17	-2.6362783E+05
7	-	5.0443342E+19	9.1863973E+06
8	-	-1.1166002E+21	-1.8340614E+08
9	-	-	1.6197594E+09
10	-	-	-5.0799782E+09

Appendix B. Evaluation of the Analytic Asymptotic Green's Function Term

This Appendix presents details of evaluating the integrals of equation (3-36) which is

$$I(R) = \int_{C_{x_j}} \int_{S_{x_j}} \frac{1}{R} \left[1 - \frac{|x' - x_j|}{a} \right] ds' dx \quad (3-36)$$

where the contour C_{x_j} is defined by $x \in [-a/2, a/2]$ and the surface S_{x_j} is defined by $x' \in [-a, a]$ and $y' \in [-b/2, b/2]$. In this instance, the variable $R = [(x - x')^2 + (y_j - y')^2]^{\frac{1}{2}}$. Over a y-directed current cell the integration is defined as follows:

$$I(R) = \int_{C_{y_j}} \int_{S_{y_j}} \frac{1}{R} \left[1 - \frac{|y' - y_j|}{b} \right] ds' dy \quad (B-1)$$

where C_{y_j} is defined by $y \in [-b/2, b/2]$ and the surface S_{y_j} is defined by $x' \in [-a/2, a/2]$ and $y' \in [-b, b]$ and $R = [(x_j - x')^2 + (y - y')^2]^{\frac{1}{2}}$.

Equations (3-36) and (B-1) are identical with the exchange of variables a and b except for the constants x_j and y_j which will drop out of the equations after an exchange of variables. Since the expressions over both x-directed and y-directed cells are equivalent, only the integration of (3-36) will be detailed.

The first step of the integration is to complete the integration with respect to y' , to do so let $u = y_m - y'$ therefore $du = -dy'$, and equation (3-36) then becomes

$$I(R) = 2 \int_{x_j}^{x_j+a} \int_{x_j-a}^{x_j+a} \int_0^{b/2} \left[\frac{1}{\sqrt{(x-x')^2 + u^2}} \right] \left[1 - \frac{|x' - x_j|}{a} \right] du dx' dx \quad (B-2)$$

where the fact that the integrand is even with respect to u has been used to half the integration interval and double the result.

Completing the integration with respect to u produces

$$I(R) = 2 \int_{x_j}^{x_j+a} \int_{x_j-a}^{x_j+a} \left[1 - \frac{|x' - x_j|}{a} \right] \ln \left[u + \sqrt{(x-x')^2 + u^2} \right]_0^{b/2} dx' dx \quad (B-3)$$

After evaluating the integrand for the limits of u , the expression for $I(R)$ can be written

$$I(R) = 2 \int_{x_j-a}^{x_j+a} \left[1 - \frac{|x' - x_j|}{a} \right] f(x) dx' \quad (B-4)$$

where the function $f(x)$ is defined by the integral

$$f(x) = \int_{x_j - a/2}^{x_j + a/2} \ln \left[\frac{\frac{b}{2} + \sqrt{(\bar{x}-\bar{x}')^2 + \frac{b^2}{4}}}{|(\bar{x}-\bar{x}')|} \right] dx \quad (B-5)$$

To alleviate the difficulties of the absolute value argument in the denominator of equation (B-5), the interval of integration can be broken into two separate sections such that $\bar{x}' < \bar{x}$, and $\bar{x}' > \bar{x}$. Therefore the integral of equation (B-5) can be written as follows:

$$\begin{aligned} f(x) = & \int_{x_j - a/2}^{x'} \ln \left[\frac{\frac{b}{2} + \sqrt{(\bar{x}-\bar{x}')^2 + \frac{b^2}{4}}}{(\bar{x}'-\bar{x})} \right] d\bar{x} \\ & + \int_{x'}^{x_j + a/2} \ln \left[\frac{\frac{b}{2} + \sqrt{(\bar{x}-\bar{x}')^2 + \frac{b^2}{4}}}{(\bar{x}-\bar{x}')} \right] d\bar{x} \end{aligned} \quad (B-6)$$

Let the first integral of (B-6) be designated $f_1(x)$ and the second as $f_2(x)$. To evaluate these integrals, the change of variables $(\bar{x}' - \bar{x}) = bu/2$ is used in $f_1(x)$, and $(\bar{x} - \bar{x}') = bu/2$ is used in $f_2(x)$. With this substitution, the integrands become the logarithmic identity for the inverse hyperbolic cosecant of u , and the integrals have the form

$$f_s(x) = \frac{b}{2} \int_0^{\lambda} \operatorname{csch}^{-1}(u) du \quad (B-7)$$

where

$$\lambda_s = \begin{cases} \frac{2}{b} \left(x' - x_j + \frac{a}{2} \right); & s = 1 \\ \frac{2}{b} \left(x_j - x' + \frac{a}{2} \right); & s = 2 \end{cases} \quad (B-8)$$

The result for the integration of equation (B-7) is obtained from an integration table [7:375], and then evaluated for the interval of integration producing the results

$$f_1(x) = \frac{b}{2} \left[\lambda_1 \operatorname{csch}^{-1}(\lambda_1) + \sinh^{-1}(\lambda_1) \right] \quad (B-9)$$

$$f_2(x) = \frac{b}{2} \left[\lambda_2 \operatorname{csch}^{-1}(\lambda_2) + \sinh^{-1}(\lambda_2) \right]$$

Substituting equation (B-9) into (B-4) the expression for $I(R)$ is now given by

$$I(R) = b \left\{ \int_{x_j-a}^{x_j+a} \left[1 + \frac{|x' - x_j|}{a} \right] \left[\begin{aligned} &\lambda_1 \operatorname{csch}^{-1}(\lambda_1) + \sinh^{-1}(\lambda_1) \\ &+ \lambda_2 \operatorname{csch}^{-1}(\lambda_2) + \sinh^{-1}(\lambda_2) \end{aligned} \right] dx' \right\} \quad (B-10)$$

Now, consider the terms with arguments of λ_1 , and define the integral with the $\text{csch}^{-1}(\lambda_1)$ term as $I_1(x')$, the integral with the $\sinh^{-1}(\lambda_1)$ as $I_2(x')$, the $\text{csch}^{-1}(\lambda_2)$ term as $I_3(x')$, and the integral with the $\sinh^{-1}(\lambda_2)$ as $I_4(x')$. Let $u = x' - x_j$, then the components of $I(R)$ become

$$\begin{aligned} I_1(u) &= 4 \int_{-\infty}^{\infty} \left[1 - \frac{|u|}{a} \right] \left\{ \left(u + \frac{a}{2} \right) \text{csch}^{-1} \left[\frac{2}{b} \left(u + \frac{a}{2} \right) \right] \right\} du \\ I_2(u) &= 2b \int_{0}^{\infty} \left[1 - \frac{|u|}{a} \right] \sinh^{-1} \left[\frac{2}{b} \left(u + \frac{a}{2} \right) \right] du \\ I_3(u) &= 4 \int_{0}^{\infty} \left[1 - \frac{|u|}{a} \right] \left\{ \left(\frac{a}{2} - u \right) \text{csch}^{-1} \left[\frac{2}{b} \left(\frac{a}{2} - u \right) \right] \right\} du \\ I_4(u) &= 2b \int_{0}^{\infty} \left[1 - \frac{|u|}{a} \right] \sinh^{-1} \left[\frac{2}{b} \left(\frac{a}{2} - u \right) \right] du \end{aligned} \quad (\text{B-11})$$

where the fact that all four integrals are even with respect to u has been used to half the interval of integration and double the result. In the first and third integral, the $2/b$ factor has been combined with the b outside the integral in equation (B-10). Now the original integral is given by $I(R) = 4I_1(u) + 2bI_2(u) + 4I_3(u) + 2bI_4(u)$.

To find $I_1(u)$, let $v = 2(u + a/2)/b$, then $I_1(u) = I_1(v)$ where

$$I_1(v) = \left(\frac{b}{2} \right)^2 \int_{r}^{3r} \left(\frac{3}{2} - \frac{1}{2r} \right) v \text{csch}^{-1}(v) dv \quad (\text{B-12})$$

Breaking $I_1(v)$ into two parts, the integration results for the parts are found in the integral tables [7:375], and $I_1(v)$ can be written as follows:

$$I_1(v) = \left(\frac{b}{2}\right)^2 \left\{ \begin{aligned} & \frac{3}{4} \left[v^2 \operatorname{csch}^{-1}(v) + \sinh^{-1}(v) \right] \\ & - \frac{b}{2a} \left[\frac{v^3}{3} \operatorname{csch}^{-1}(v) \right. \\ & \quad \left. + \frac{1}{3} \sinh^{-1}(v) - \frac{v}{3\sqrt{v^2+1}} \right] \end{aligned} \right\}_{v=\tau}^{v=3\tau} \quad (B-13)$$

where

$$\tau = a/b$$

and the absolute value signs in the integration formulas from the tables can be ignored since v is always positive for $v \in [\tau, 3\tau]$.

For $I_2(u)$, use the same change of variables u to v and obtain

$$I_2(v) = \left(\frac{b}{2}\right) \int_{-\tau}^{\tau} \left(\frac{3}{2} - \frac{v}{2\tau} \right) \sinh^{-1}(v) dv \quad (B-14)$$

$I_2(v)$ can be separated into two integrals and the formulas from the integral table [7:374] give

For $I_3(u)$ and $I_4(u)$, the substitution $v = 2(a/2 - u)/b$ is used and the interval of integration is given by $v \in [-\tau, \tau]$. Since v can be

v-3+

$$\sqrt{v^2 + 1}$$

$$- \frac{b}{2a} \left[\left(\frac{v^2}{2} + \frac{1}{4} \right) \sinh^{-1}(v) - \frac{v}{4} \sqrt{v+1} \right]_{v=+},$$

value of v must be retained in the integral formulas and the results are

$$I_3(v) = \left(\frac{b}{2} \right)^2 \left\{ \begin{aligned} & \frac{3}{4} \left[v^2 \operatorname{csch}^{-1}(v) + \frac{1}{|v|} \sinh^{-1}(v) \right] \\ & + \frac{b}{2a} \left[\begin{aligned} & \frac{v^3}{3} \operatorname{csch}^{-1}(v) \\ & + \frac{v}{3|v|} \left(\sinh^{-1}(v) - \frac{v}{\sqrt{v^2+1}} \right) \end{aligned} \right] \end{aligned} \right\}_{v=-+}, \quad (B-16)$$

$$I_4(v) = \left(\frac{b}{2} \right) \left\{ \begin{aligned} & \frac{1}{2} \left[v \sinh^{-1}(v) - \sqrt{v^2+1} \right] \\ & - \frac{b}{2a} \left[\left(\frac{v^2}{2} + \frac{1}{4} \right) \sinh^{-1}(v) - \frac{v}{4} \sqrt{v+1} \right] \end{aligned} \right\}_{v=-+}, \quad (B-17)$$

Evaluating equations (B-14) through (B-17) at the defined limits, combining the results, and using the identities $\sinh^{-1}(-x) = -\sinh^{-1}(x)$ and $\operatorname{csch}^{-1}(-x) = -\operatorname{csch}^{-1}(x)$ the expression given in equation (3-37) is obtained.

Bibliography

1. Bahl, I.J. and P. Bhartia. *Microstrip Antennas*, Dedham, Massachusetts: Artech House Inc., 1980.
2. Balanis, Constantine A. *Antenna Theory*. New York: John Wiley and Sons, 1982.
3. Barksdale, Major Harry A. Class handout distributed in EENG 625, *Antennas*. School of Engineering, Air Force Institute of Technology (AU), Wright-Patterson AFB OH, Sep 1989.
4. ———. Class handout in EENG 630, *Applications of Electromagnetic Theory*. School of Engineering, Air Force Institute of Technology (AU), Wright-Patterson AFB OH, Sep 1989.
5. Barlatey, Lionel et al. "Analysis of Stacked Patches with a Mixed Potential Integral Equation," *IEEE Transactions on Antennas and Propagation*, 38: 609-615 (May 1990).
6. Carver, Keith R. and James W. Mink. "Microstrip Antenna Technology", *IEEE Transactions on Antennas and Propagation*, 29: 2-24 (Jan 1981).
7. *CRC Standard Mathematical Tables*, 25th Edition, edited by William H. Beyer. Boca Raton, FL: CRC Press Inc., 1981.
8. Erwert, Capt Ronald E. *Polynomial Approximations of the Green's Functions for an Aperture-Fed, Stacked Patch Microstrip Antenna*. MS Thesis, AFIT/GE/ENG/90D-XX, School of Engineering, Air Force Institute of Technology (AU), Wright-Patterson AFB OH, December 1990.
9. Ferguson, Thomas R. and Theodore H. Lenman. "Efficient Solution of Large Moments Problems: Theory and Small Problem Results," *IEEE Transactions on Antennas and Propagation*, 24: 230-235 (Mar 1976).
10. Hall, Richard C. and Mosig, Juan R. "The Analysis of Coaxially Fed Microstrip Antennas with Electrically Thick Substrates," *Electromagnetics* 9: 367-384 (1989).
11. Hammer, D. et al. "A Model for Calculating the Radiation Field of Microstrip Antennas," *IEEE Transactions on Antennas and Propagation*, 27: 267-270 (Mar 79).
12. Johnson and Rice. *Numerical Analysis*, 2nd Edition. Reading, Massachusetts: Addison Wesley Publishing Company, 1982.

13. Kobayashi, Masanori. "Longitudinal and Transverse Current Distributions on Microstriplines and Their Closed-Form Expression," *IEEE Transactions on Microwave Theory and Techniques*, 33: 784-788 (Sep 1985).
14. Lee, R. Q. et al. "Characteristics of a Two-Layer Electromagnetically Coupled Rectangular Patch Antenna," *Electronics Letters*, 23: 1070-1072 (Sep 1987).
15. ——. "Two-Layer Electromagnetically Coupled Rectangular Patch Antenna," *1988 IEEE Antennas and Propagation Society International Symposium Digest*, 3: 948-951. New York: IEEE Press, 1988.
16. Lin, Y. and L. Shafai. "Moment-Method Solution of the Near-Field Distribution and Far-Field Patterns of Microstrip Antennas," *IEE Proceedings*, 132 Pt. H: 369-374 (Oct 1985).
17. Moore, J. and R. Pizer, editors, *Moment Methods in Electromagnetics, Techniques and Applications*. Letchworth, Hertfordshire, England: Research Studies Press Ltd., 1984.
18. Mosig, Juan R. "Arbitrarily Shaped Microstrip Structures and Their Analysis with a Mixed Potential Integral Equation," *IEEE Transactions on Microwave Theory and Techniques*, 36: 314-323 (Feb 1988).
19. Mosig, J. R. et al. "Numerical Analysis of Microstrip Patch Antennas," *Handbook of Microstrip Antennas*, Volume 1, edited by J. R. James and P. S. Hall. London, United Kingdom: Peter Peregrinus Ltd, 1989.
20. Mosig, J. R. and F. E. Gardiol. "General Integral Equation Formulation for Microstrip Antennas and Scatterers," *IEE Proceedings*, 132 Pt. H: 424-432 (Dec 1985).
21. ——. "A Dynamical Radiation Model for Microstrip Structures," *Advances in Electronics and Electron Physics*, 59. New York: Academic Press, 1982.
22. ——. "Current Distribution in Microstrip Planar Antennas," *Proceedings of the 10th European Microwave Conference*. 117-121. Kent, England: Microwave Exhibitions and Publishers, Ltd, 1981.
23. Nazar, Capt James B. *Green's Functions for a Theoretical Model of an Aperture Fed Stacked Patch Microstrip Antenna*, MS thesis, AFIT/GE/ENG/89D-37, School of Engineering, Air Force Institute of Technology (AU), Wright-Patterson AFB OH, December 1989 (AD-A216-280).

24. Newman, Edward H. and Pravit Tulyathan. "Analysis of Microstrip Antennas Using Moment Methods," *IEEE Transactions on Antennas and Propagation*, 29: 47-53 (Jan 1981).
25. Oltman, H. George and Donald A. Huebner. "Electromagnetically Coupled Microstrip Dipoles" *IEEE Transactions on Antennas and Propagation*, 29: 151-157 (Jan 1981).
26. Pozar, D. M. "A Reciprocity Method of Analysis for Printed Slot and Slot Coupled Microstrip Antennas," *IEEE Transactions on Antennas and Propagation*, 34: 1439-1446 (Dec 1986).
27. ———. "Microstrip Antenna Aperture Coupled to a Microstripline," *Electronics Letters*, 21: 49-50 (Jan 1985).
28. Sabban, Albert. "A New Broadband Stacked Two-Layer Microstrip Antenna," *1983 IEEE Antennas and Propagation Society International Symposium Digest*. 63-66. New York: IEEE Press, 1983.
29. Sullivan, Peter L. and Daniel H. Schaubert. "Analysis of an Aperture Coupled Microstrip Antenna," *IEEE Transactions on Antennas and Propagation*, 34: 977-984 (Aug 1986).
30. Terry, Capt Christopher I. *Measurements of the Radiation Characteristics of an Aperture-Fed, Stacked Patch microstrip Antenna*. MS Thesis, AFIT/GE/ENG/90D-36, School of Engineering, Air Force Institute of Technology (AU), Wright-Patterson AFB OH, December 1990.
31. Tsao, C.H. and others. "Aperture-coupled Patch Antennas with Wide-bandwidth and Dual-polarization Capabilities," *1988 IEEE Antennas and Propagation Society International Symposium Digest*, 3: 936-940. New York: IEEE Press, 1988.

Vita

Captain William L. Irvin was born on 18 March 1958 in Ashburn, Georgia and graduated from Avon Park High School, Avon Park, Florida in 1976. Captain Irvin enlisted in the U. S. Air Force in September, 1976 and entered active duty in March 1977 as an Avionics Navigation Systems Technician. He completed six years of enlisted service with the 86th Tactical Fighter Wing at Ramstein Air Base, Federal Republic of Germany and the 1st Special Operations Wing, Hurlburt Field, Florida before his acceptance into the Air Force's Airman Education and Commissioning Program (AECP). While in AECP, he received his Bachelor of Science Degree in Electrical Engineering from the University of Florida, graduating with honors in December, 1985. After graduating from Officer Training School in 1986, Captain Irvin was assigned to the Flight Dynamics Laboratory, Wright Research and Development Center, Wright-Patterson Air Force Base where he served as a Research Flight Simulations Officer from 1986 to 1988 and as Executive Officer to the Laboratory Director from 1988 to 1990. He entered the School of Engineering, Air Force Institute of Technology in May 1989 as a graduate student in the Observables Reduction Technology curriculum.

Permanent Mailing Address: 1611 NW 94th Street
Gainesville, FL 32606

Public reporting burden for this collection of information is estimated to average 1 hour per response, including the time for reviewing instructions, searching existing data sources, gathering and maintaining the data needed, and completing and reviewing the collection of information. Send comments regarding this burden estimate or any other aspect of this collection of information, including suggestions for reducing this burden, to Washington Headquarters Services, Directorate for Information Operations and Reports, 1215 Jefferson Davis Highway, Suite 1204, Arlington, VA 22202-4302, and to the Office of Management and Budget, Paperwork Reduction Project (0704-0188), Washington, DC 20523.

1. AGENCY USE ONLY (Leave blank)	2. REPORT DATE December 1990	3. REPORT TYPE AND DATES COVERED Master's Thesis	
4. TITLE AND SUBTITLE A Method of Moments Solution for the Electric Currents on An Aperture-Fed, Stacked Patch Microstrip Antenna		5. FUNDING NUMBERS	
6. AUTHOR(S) William L. Irvin, Capt, USAF			
7. PERFORMING ORGANIZATION NAME(S) AND ADDRESS(ES) Air Force Institute of Technology WPAFB, OH 45433-6538		8. PERFORMING ORGANIZATION REPORT NUMBER AFIT/GE/ENG/90D-27	
9. SPONSORING/MONITORING AGENCY NAME(S) AND ADDRESS(ES)		10. SPONSORING/MONITORING AGENCY REPORT NUMBER	
11. SUPPLEMENTARY NOTES			
12a. DISTRIBUTION/AVAILABILITY STATEMENT Approved for public release; distribution unlimited		12b. DISTRIBUTION CODE	
13. ABSTRACT (Maximum 200 words) This study presents a method of moments solution for the surface currents and charge distributions on an aperture-fed, stacked patch microstrip antenna. To make the solution independent of the excitation technique, an aperture magnetic current distribution is assumed, and the spatial Green's functions of the antenna are used to calculate the tangential fields on the patches and coefficients for a finite series expansion of the surface currents and charge densities. The Green's functions of the antenna are modeled with polynomials that are a function of the radial distance separating observer and source locations. The method of moments solution is implemented using FORTRAN 77 and requires no external software support. The numerical techniques, algorithms, and complete software descriptions are also included.			
14. SUBJECT TERMS Microstrip Antennas, Aperture Feed, Stacked Patch, Numerical Analysis		15. NUMBER OF PAGES 174	16. PRICE CODE
17. SECURITY CLASSIFICATION OF REPORT Unclassified	18. SECURITY CLASSIFICATION OF THIS PAGE Unclassified	19. SECURITY CLASSIFICATION OF ABSTRACT Unclassified	20. LIMITATION OF ABSTRACT U